JOURNAL OF PETROLOGY | VOLUME 54 | NUMBER 7 | PAGES 1309–1348 | 2013 | doi:10.1093/petrology/egt013

Geochemical, Sr–Nd–Pb, and Zircon Hf–O Isotopic Compositions of Eocene–Oligocene Shoshonitic and Potassic Adakite-like Felsic Intrusions in Western Yunnan, SW China: Petrogenesis and Tectonic Implications

YONG-JUN LU[1,2]*, ROBERT KERRICH[3], T. CAMPBELL McCUAIG[1], ZHENG-XIANG LI[4], CRAIG J. R. HART[5], PETER A. CAWOOD[1,6], ZENG-QIAN HOU[2], LEON BAGAS[1], JOHN CLIFF[1,7], ELENA A. BELOUSOVA[8] AND SUO-HAN TANG[2]

[1]CENTRE FOR EXPLORATION TARGETING, AUSTRALIAN RESEARCH COUNCIL CENTRE OF EXCELLENCE FOR CORE TO CRUST FLUID SYSTEMS (CCFS), SCHOOL OF EARTH AND ENVIRONMENT, UNIVERSITY OF WESTERN AUSTRALIA, PERTH, WA 6009, AUSTRALIA

[2]INSTITUTE OF GEOLOGY, CHINESE ACADEMY OF GEOLOGICAL SCIENCES, BEIJING 100037, CHINA

[3]DEPARTMENT OF GEOLOGICAL SCIENCES, UNIVERSITY OF SASKATCHEWAN, SASKATOON, SK, CANADA S7N 5E2

[4]AUSTRALIAN RESEARCH COUNCIL CENTRE OF EXCELLENCE FOR CORE TO CRUST FLUID SYSTEMS, INSTITUTE FOR GEOSCIENCE RESEARCH, DEPARTMENT OF APPLIED GEOLOGY, CURTIN UNIVERSITY, GPO BOX U1987, PERTH, WA 6845, AUSTRALIA

[5]MINERAL DEPOSIT RESEARCH UNIT, DEPARTMENT OF EARTH AND OCEAN SCIENCES, UNIVERSITY OF BRITISH COLUMBIA, 6339 STORES ROAD, VANCOUVER, BC, CANADA V6T 1Z4

[6]DEPARTMENT OF EARTH SCIENCES, UNIVERSITY OF ST. ANDREWS, NORTH STREET, ST. ANDREWS KY16 9AL, UK

[7]CENTRE FOR MICROSCOPY, CHARACTERIZATION AND ANALYSIS, UNIVERSITY OF WESTERN AUSTRALIA, 35 STIRLING HIGHWAY, CRAWLEY, WA 6009, AUSTRALIA

[8]AUSTRALIAN RESEARCH COUNCIL CENTRE OF EXCELLENCE FOR CORE TO CRUST FLUID SYSTEMS AND GEMOC KEY CENTRE, DEPARTMENT OF EARTH AND PLANETARY SCIENCES, MACQUARIE UNIVERSITY, SYDNEY, NSW 2109, AUSTRALIA

RECEIVED JANUARY 5, 2012; ACCEPTED FEBRUARY 14, 2013
ADVANCE ACCESS PUBLICATION MARCH 15, 2013

Coeval potassic adakite-like and shoshonitic felsic intrusions in the western Yunnan province of SW China are spatially and temporally associated with Eocene–Oligocene shoshonitic mafic volcanic rocks. The shoshonitic syenite and quartz monzonite intrusions are characterized by high K_2O contents (4·9–6·8 wt %) and K_2O/Na_2O ratios (1·1–1·7), high Y (1·7–34·8 ppm) and Yb (1·50–3·16 ppm) contents, nearly flat heavy rare earth element (HREE) patterns and moderate Eu anomalies (Eu/Eu = 0·65–0·78). The potassic adakite-like granite and quartz monzonite intrusions are characterized by enrichment in light rare earth elements (LREE), depletion in HREE and fractionated HREE patterns, high Sr (328–1423 ppm), Sr/Y (38–243) and La/Yb (23–62), and low Y*

*Corresponding author. Present address: Centre for Exploration Targeting, Australian Research Council Centre of Excellence for Core to Crust Fluid Systems (CCFS), School of Earth and Environment, University of Western Australia, Perth, WA 6009, Australia. E-mail: geoyongjun@gmail.com

and Yb contents. The shoshonitic syenite and quartz monzonites have the same Sr–Nd–Pb isotope compositions as the shoshonitic mafic volcanic rocks. They define linear trends on Harker diagrams, and have similar REE and trace element patterns to the shoshonitic mafic volcanic rocks. These observations suggest that the shoshonitic syenite and quartz monzonite magmas were differentiated from parental shoshonitic mafic melts by fractional crystallization of olivine, clinopyroxene and feldspar. The parent magmas originated from a metasomatized lithospheric mantle source. The shoshonitic syenite and quartz monzonites have higher magmatic zircon $\delta^{18}O$ values (6·26–7·05‰) than the mantle, which suggests some ^{18}O enrichment during earlier subduction-related metasomatism of their lithospheric mantle source. The potassic adakite-like granites have Sr–Nd–Pb isotopic compositions that overlap those of lower-crustal amphibolites. They have low Mg#, MgO, Ni and Cr contents, abundant inherited zircons, high zircon εHf (0–5·5) and mantle-like $\delta^{18}O$ (4·78–6·25‰) values. These granites were plausibly derived by partial melting of a thickened, potassic, mafic, lower crust with minor input from an older igneous felsic component. The potassic adakite-like quartz monzonites contain abundant mafic microgranular enclaves, and have transitional major and trace element characteristics between the adakite-like granite and the shoshonitic mafic magma. The quartz monzonites generally have higher Mg#, MgO, Ni and Cr contents than the lower crust-derived adakite-like rocks. They have no inherited zircons and have uniform zircon εHf and $\delta^{18}O$ values. It is suggested that they were derived by variable degrees of mixing between lower-crustal melts and shoshonitic mafic magmas. The coeval shoshonitic and potassic adakite-like rocks appear to be associated with thinning of overthickened lithospheric mantle along the trans-lithospheric Jinsha suture following the collision between India and Asia. This lithospheric thinning could have resulted in the upwelling of the asthenosphere beneath western Yunnan, which induced partial melting of the residual metasomatized lithospheric mantle as well as the thickened lower crust in the Eocene.

KEY WORDS: *adakite; shoshonite; zircon; thickened lower crust; metasomatized mantle lithosphere; western Yunnan*

INTRODUCTION

Adakites are sodic, aluminous igneous rocks that were originally proposed to be derived by partial melting of hot, young (age <20 Ma) subducted oceanic crust in intra-oceanic arcs. Fractionated rare earth element patterns (REE) in conjunction with low Yb suggest melting in equilibrium with residual garnet (Defant & Drummond, 1990; Foley *et al.*, 2002). Adakites in Cenozoic oceanic arcs are associated with tholeiitic to calc-alkaline basalts, Nb-enriched basalts, and magnesian andesites (Kepezhinskas *et al.*, 1996; Sajona *et al.*, 1996; Richards & Kerrich, 2007). A number of other mechanisms have also been proposed for the origin of sodic adakite-like rocks, including the following: (1) crustal assimilation and high-pressure fractional crystallization (AFC) of basaltic magma in island arcs or continental margin arcs, characterized by the basalt–andesite–dacite–rhyolite magma series (BADR; Castillo *et al.*, 1999; Rohrlach & Loucks, 2005; Macpherson *et al.*, 2006; Richards & Kerrich, 2007); (2) partial melting in an intracontinental setting of delaminated mafic lower crust in the lithospheric mantle (Kay & Kay, 1993; Xu *et al.*, 2002; Wang *et al.*, 2006*a*, 2006*b*); (3) partial melting of a thickened mafic lower crust along a continental margin above a subduction zone (Atherton & Petford, 1993; Petford & Atherton, 1996). Recently, potassic, aluminous, adakite-like rocks belonging to the shoshonitic or high-K calc-alkaline magma series have been identified in Tibet and eastern China. These potassic adakite-like rocks are characterized by higher K_2O/Na_2O (~1) than sodic adakites ($K_2O/Na_2O < 0{\cdot}6$), and by the lack of either temporal or spatial relationship with subduction (Xiao & Clemens, 2007). These potassic adakite-like rocks share the fractionated REE patterns of their sodic counterparts; they have been interpreted to be derived from partial melting of potassium-rich mafic sources in thickened lower continental crust (Chung *et al.*, 2003; Hou *et al.*, 2004; Wang *et al.*, 2005; Xiong *et al.*, 2011) or delaminated lower crust (Xu *et al.*, 2002; Wang *et al.*, 2006*a*, 2006*b*). These potassic adakite-like rocks in China are generally coeval with, and spatially related to, mafic shoshonitic suites (Hou *et al.*, 2004; Wang *et al.*, 2006*a*).

It is generally considered that mafic shoshonitic igneous rocks are derived from partial melting of enriched asthenosphere (e.g. Müller & Groves, 1993; Wyman & Kerrich, 1993) or metasomatically enriched lithospheric mantle (e.g. Cousens *et al.*, 2001; Leslie *et al.*, 2009). Felsic shoshonitic rocks are proposed to be the products of partial melting of underplated mafic rocks enriched in incompatible elements (Wang *et al.*, 2005; Pe-Piper *et al.*, 2009) or fractional crystallization with concurrent crustal assimilation of a shoshonitic mafic melt (e.g. Turner *et al.*, 1996; Miller *et al.*, 1999).

Given the diverse origins of adakitic rocks (Richards & Kerrich, 2007; Castillo, 2012), in this contribution the term 'adakite' is strictly used to refer to rocks derived from slab melting. Other rocks sharing similar trace element characteristics with 'adakite', but without a slab melting origin, are referred to as 'adakite-like'. Specifically, these 'adakite-like' rocks are those plotting in the 'adakite' fields in Sr/Y vs Y and La/Yb vs Yb plots as proposed by Richards & Kerrich (2007). The 'shoshonitic' rocks in this study refer to rocks that plot in the shoshonitic field in a K_2O vs SiO_2 diagram, but are outside the 'adakite' fields in Sr/Y vs Y and La/Yb vs Yb diagrams.

Here we report new elemental, Sr–Nd–Pb, and zircon Hf–O isotope data for an association of Cenozoic potassic adakite-like and shoshonitic igneous rocks in western Yunnan, SW China. The association provides new insights

into the petrogenesis and tectonic setting of these rocks. The main objectives of this study are to (1) characterize the distinctive chemical features of spatially related, coeval, potassic adakite-like and shoshonitic intrusions, (2) determine the magma sources and petrogenesis of the two suites, and (3) account for the coeval emplacement of potassic adakite-like and shoshonitic intrusions.

GEOLOGICAL SETTING

Continued collision of the Indian and Asian plates since the early Cenozoic (*c.* 60–55 Ma), driven by subduction of Indian lithosphere (Capitanio *et al.*, 2010), has resulted in formation of the Himalayan orogenic belt, including the Tibetan Plateau (Lee & Lawver, 1995; Yin & Harrison, 2000; Chung *et al.*, 2005; Molnar & Stock, 2009). Lithospheric shortening was accommodated by subduction of Indian continental lithosphere, thickening of Asian lithosphere, and in part by southeastward extrusion tectonics facilitated by strike-slip motion along the NW–SE- to WNW–ESE-trending Ailao Shan–Red River shear zone (ASRR; Fig. 1; Tapponnier *et al.*, 1990; Leloup *et al.*, 1995; Chung *et al.*, 1997; Yin & Harrison, 2000). It is widely considered that the lower portion of the overthickened Asian continental mantle lithosphere (CLM) was convectively removed post-collision at *c.* 26 Ma in South Tibet and at *c.* 13 Ma in North Tibet, resulting in upwelling asthenosphere that was accompanied by uplift of the Tibetan Plateau (Molnar *et al.*, 1993; Houseman & Molnar, 1997; Owens & Zandt, 1997; Chung *et al.*, 2005, 2009; Kind & Yuan, 2010; Liu *et al.*, 2011). The convective thinning of the Asian lithospheric mantle was accompanied by widespread post-collisional potassic volcanism in the Tibetan Plateau owing to the melting of residual subduction-modified CLM (Turner *et al.*, 1993, 1996; Chung *et al.*, 1998, 2005; Xia *et al.*, 2011).

The Tibetan Plateau comprises the Songpan–Ganzi, Qiangtang and Lhasa terranes, which were amalgamated before the Cretaceous along the Paleo-Tethys Jinsha suture and the Meso-Tethys Nujiang suture (Fig. 1; Yin & Harrison, 2000; Metcalfe, 2006). The Yangtze Craton lies to the SE of the Tibetan Plateau (Fig. 1).

The western Yangtze Craton was part of the Rodinia supercontinent and the site of oceanic subduction during the early Neoproterozoic (*c.* 1040–900 Ma; Li *et al.*, 2008*b*; Wang *et al.*, 2009). This was then followed by mantle plume-related magmatic activity between 825 and 750 Ma during the breakup of Rodinia, as indicated by widespread mafic dyke swarms, continental flood basalts, and continental rifting over much of the craton (Ernst *et al.*, 2008; Li *et al.*, 2008*b*; Wang *et al.*, 2009).

During the latest Neoproterozoic to Late Triassic (~700–220 Ma), the Yangtze Craton constituted an isolated continental terrane in the Paleo-Pacific Ocean with its western edge forming a passive continental margin (Li, 1998; Metcalfe, 2006; Pullen *et al.*, 2008). The Emeishan flood basalts erupted in the western part of the craton during Late Permian to Early Triassic times (260–250 Ma) as a consequence of a mantle plume event (Fig. 1; Chung & Jahn, 1995; Xu *et al.*, 2001*a*; Zi *et al.*, 2010). Since the Late Triassic (<220 Ma), the western part of the craton has occupied an intracontinental position (Yang, 1998; Wang *et al.*, 2000).

An Eocene–Oligocene (~40–30 Ma) potassic magmatic suite extends over 2000 km along the translithospheric Jinsha suture in a belt that crosses the Qiangtang Terrane and the western Yangtze Craton (Fig. 1; Chung *et al.*, 1998, 2005; Xia *et al.*, 2011). The suite is widely exposed in western Yunnan where the ASRR shear zone locally overprints the Jinsha suture, but extends up to 50 km to the west within the Simao Block and up to 270 km to the east into the Yangtze Craton (Fig. 1; Zeng *et al.*, 2002; Guo *et al.*, 2005). Potassic igneous rocks form small extrusive and intrusive porphyritic bodies consisting of mafic to felsic rocks. The mafic rocks are dominantly 37–33 Ma lamprophyre dykes and minor mafic lavas (Fig. 2; Xu *et al.*, 2001*b*; Li *et al.*, 2002; Guo *et al.*, 2005; Huang *et al.*, 2010). The felsic rocks are mainly 37–32 Ma syenite porphyry, quartz monzonite porphyry and monzogranitic porphyry intruded into predominantly non-metamorphosed sedimentary sequences (Fig. 2; Liang *et al.*, 2007; Lu *et al.*, 2012). More detailed geological descriptions of these intrusions have been given by Deng *et al.* (1998), Liang *et al.* (2007) and Chung *et al.* (2008). The mafic rocks have been described in previous studies and are not described further in this contribution; their genesis appears to be linked to that of the potassic felsic intrusions (Xu *et al.*, 2001*b*; Li *et al.*, 2002; Guo *et al.*, 2005; Huang *et al.*, 2010; Lu *et al.*, 2012).

Rock samples documented in this contribution were collected from well-exposed and least altered potassic felsic intrusions mainly at Jianchuan, Yongsheng, Liuhe and Binchuan in western Yunnan (Fig. 1).

PETROGRAPHY

Shoshonitic syenites were collected from Jianchuan and Liuhe (Fig. 1). At Jianchuan, ovoid mafic microgranular enclaves (MMEs) are present in equigranular syenite and have gradational contacts with the syenite (Fig. 3a). Abundant angular to subangular garnet-bearing xenoliths are present in the syenite porphyry at Liuhe, including upper mantle-derived garnet clinopyroxenite originating from an estimated depth of 90 km, lower crust-derived garnet–diopside amphibolite and granulite from ~45–55 km depth, and middle crust-derived garnet–plagioclase amphibolites from ~30 km depth (Fig. 3b; Zhao *et al.*, 2003). Shoshonitic syenites have equigranular or porphyritic textures consisting of potassic feldspar, amphibole, clinopyroxene, biotite, and occasionally plagioclase, with grain

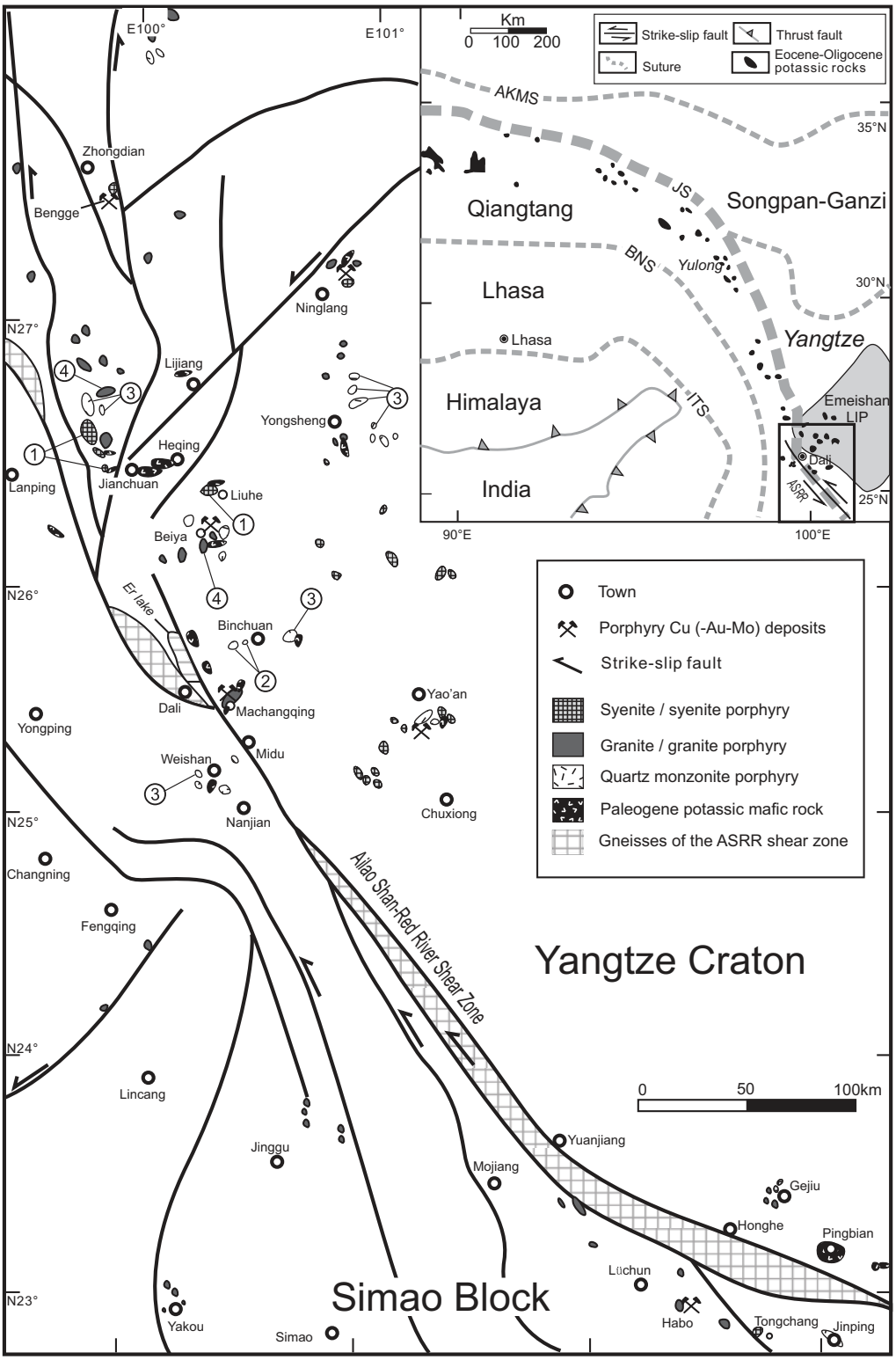

Fig. 1. Simplified geological map showing the distribution of Cenozoic potassic igneous rocks in western Yunnan (modified from Zeng *et al.*, 2002; Huang *et al.*, 2010). Inset shows the tectonic framework of the Tibetan Plateau and highlights the distribution of Eocene–Oligocene potassic igneous rocks along the Jinsha Suture (modified from Chung *et al.*, 2005). The Emeishan flood basalt province is also shown in the inset as a shaded field (Emeishan LIP). AKMS, Anyimaqin–Kunlun–Muztagh Suture; JS, Jinsha Suture; BNS, Bangong–Nujiang Suture; ITS, Indus–Tsangpo Suture; ASRR, Ailao Shan–Red River shear zone. The approximate localities of the studied magmatic suites are indicated: 1, shoshonitic syenite; 2, shoshonitic quartz monzonite; 3, potassic adakite-like quartz monzonite; 4, potassic adakite-like granite.

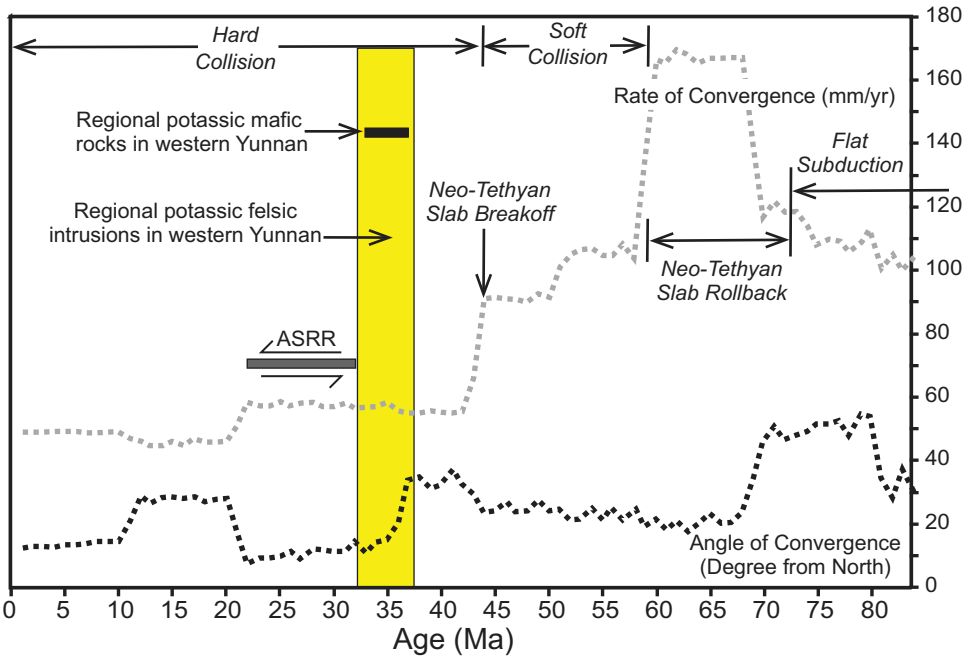

Fig. 2. Ages of potassic magmatism in western Yunnan compared with the rate and angle of convergence between India and Asia (modified after Chung *et al.*, 2005; Lu *et al.*, 2012). The shaded column represents the zircon U–Pb ages of regional potassic felsic intrusions in western Yunnan (36·9 ± 0·3 to 32·5 ± 0·3 Ma); the horizontal bar within the column shows the Ar–Ar age of regional potassic mafic volcanic rocks in western Yunnan (36·6 ± 0·2 to 33·4 ± 0·5 Ma); also shown is the age of sinistral strike-slip movement along the Ailao Shan–Red River shear zone (ASRR) in western Yunnan (*c.* 32–22 Ma). All ages from compilations by Lu *et al.* (2012).

size of 0·5–3 mm (Fig. 4a). Accessory minerals include apatite, zircon, magnetite and titanite.

Shoshonitic quartz monzonites collected from Binchuan (Fig. 1) contain garnet-free crustal xenoliths of banded gneiss and hornblendite (Fig. 3c). These intrusive rocks are porphyritic and consist of 0·5–2 mm diameter phenocrysts of potassic feldspar, plagioclase, amphibole, biotite, and quartz in a fine- to very fine-grained groundmass of potassic feldspar, plagioclase and quartz (Fig. 4b). Accessory minerals include magnetite, zircon, apatite and titanite.

Porphyritic potassic adakite-like quartz monzonites were collected from Jianchuan, Yongsheng, Binchuan and Weishan (Fig. 1). Rounded MMEs are present in some potassic adakite-like quartz monzonites and have gradational contacts with their host intrusion, indicating magma mingling (Fig. 3d). There are rounded and corroded feldspar megacrysts within the MMEs, suggesting physical transfer of crystals between the commingled magmas as exemplified by sample BC-2 (Fig. 3e; Waight *et al.*, 2000). However, we note that crustal xenoliths are absent in the potassic adakite-like quartz monzonites. These rocks contain ~0·5–2 mm diameter phenocrysts of potassic feldspar, plagioclase, amphibole, clinopyroxene, biotite and occasionally quartz in a fine-grained to microcrystalline groundmass of potassic feldspar, plagioclase, quartz and biotite (Fig. 4c). Accessory minerals are mainly magnetite, apatite, zircon and titanite.

Porphyritic potassic adakite-like granites were collected from Jianchuan and Beiya (Fig. 1). Crustal xenoliths and MMEs are not observed in these potassic adakite-like granites, but large quartz phenocrysts are abundant (Fig. 3f). These granites contain 0·5–3 mm diameter phenocrysts of plagioclase, quartz, potassic feldspar, amphibole and biotite in a fine-grained groundmass of feldspar and quartz with accessory magnetite, apatite, titanite, and zircon (Fig. 4d).

ANALYTICAL METHODS

Major and trace elements

Rock samples were cut into slabs and the freshest portions were used for bulk-rock analyses. The freshest slabs were crushed into small fragments before being further cleaned, then ground into a powder of less than 74 μm in a tungsten carbide swing mill. Major and trace element analyses were carried out at the National Research Center for Geoanalysis of Beijing. Major elements were analyzed by wet chemistry and X-ray fluorescence spectrometry (XRF), with analytical uncertainties <5% relative (Hou *et al.*, 2012).

For trace element and REE analyses, whole-rock powders (50 mg) were weighed and dissolved in 1 ml of distilled HF (1·15 g/ml) and 0·5 ml of HNO_3 (1·41 g/ml) in a Teflon-lined stainless steel bomb. The sealed bombs were then

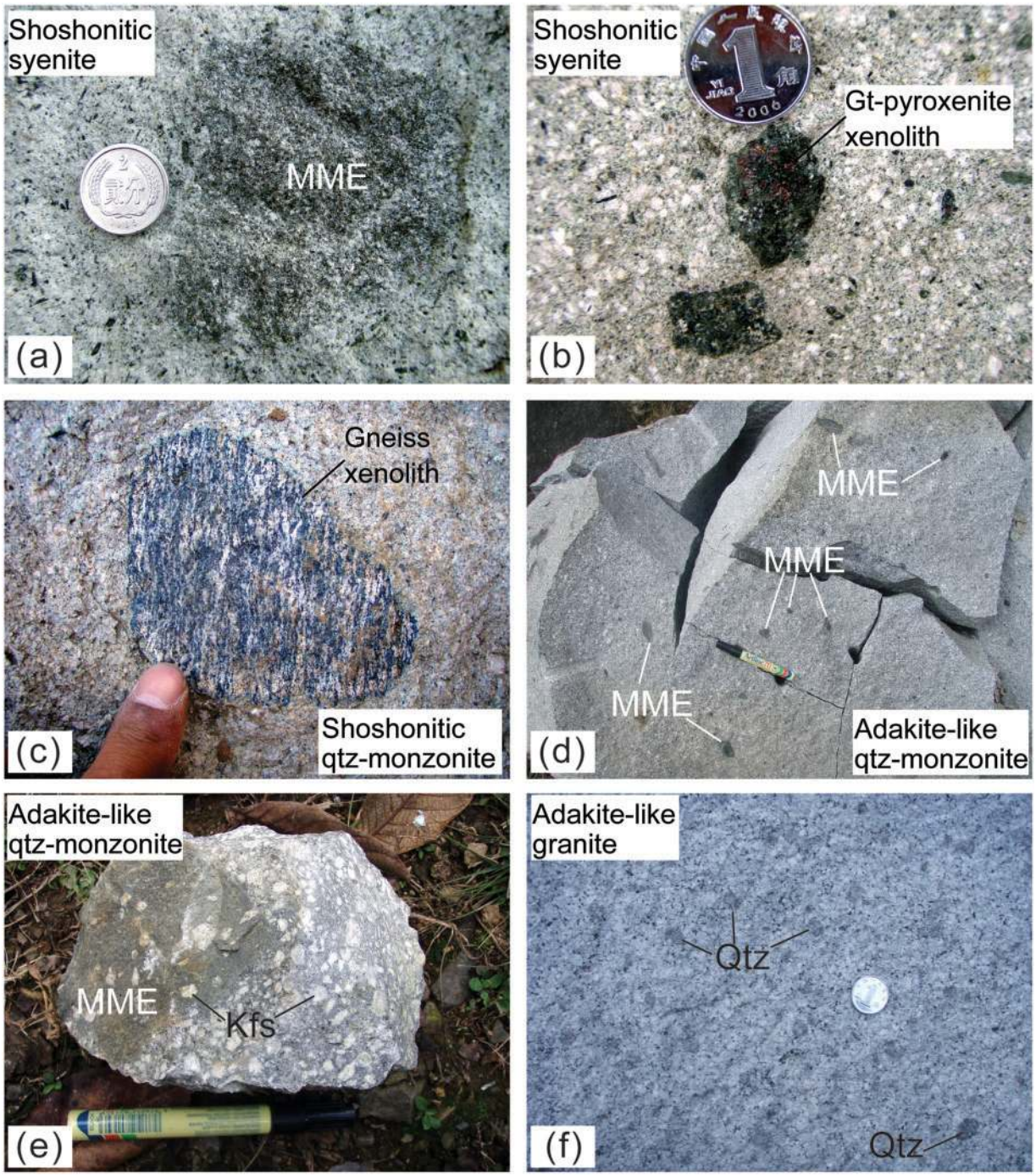

Fig. 3. Photographs showing various mafic microgranular enclaves (MMEs) and crustal xenoliths in the potassic felsic intrusions in western Yunnan. (a) Mafic enclave showing a transitional contact with the host shoshonitic syenite intrusion. Photograph from same locality as sample JC-9. (b) Garnet clinopyroxenite xenolith in a Liuhe shoshonitic syenite porphyry from the same locality as sample LH-1. (c) Feldspar–clinopyroxene banded gneiss xenolith displaying a sharp contact with the host shoshonitic quartz monzonite. Photograph taken from the same locality as sample BC-12. Finger for scale. (d) Mafic enclaves in a potassic adakite-like quartz monzonite host. Photograph from same locality as sample DHS-1. (e) Mafic enclave in a potassic adakite-like quartz monzonite host. K-feldspar megacrysts within the enclave are similar to those in the host. Photograph from the same locality as sample BC-2. (f) Potassic adakite-like granite with abundant quartz phenocrysts; mafic enclaves are absent. Photograph from the same locality as sample SG-3. The coins and pen used for scale are 2 cm in diameter and 10 cm long, respectively. Kfs, potassic feldspar; Qtz, quartz.

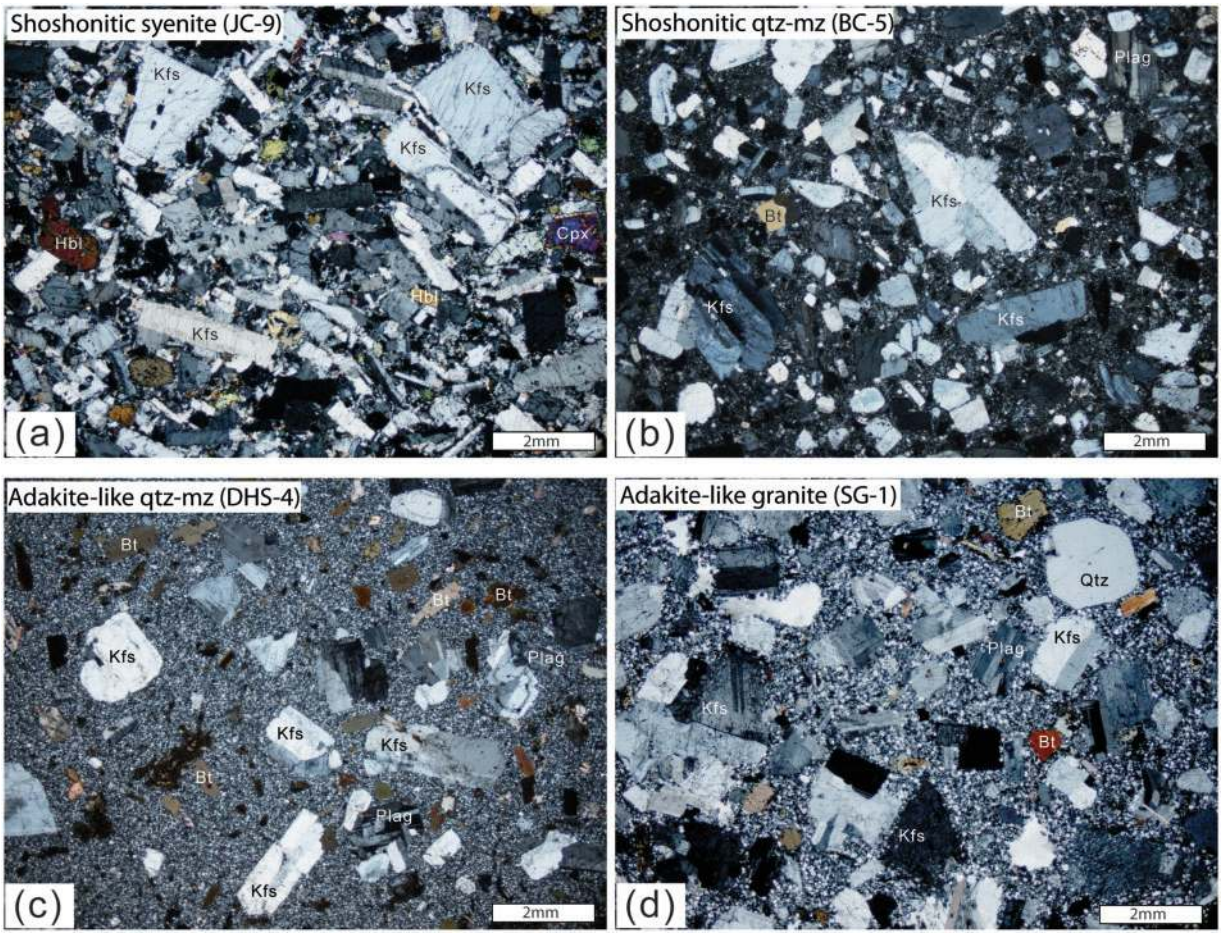

Fig. 4. Photomicrographs of potassic felsic intrusions in western Yunnan: (a) shoshonitic syenite (JC-9); (b) shoshonitic quartz monzonite (BC-5); (c) potassic adakite-like quartz monzonite (DHS-4); (d) potassic adakite-like granite (SG-1). Cpx, clinopyroxene; Hbl, hornblende; Bt, biotite; Kfs, potassic feldspar; Plag, plagioclase; Qtz, quartz.

placed in an oven and heated to 190°C for 24 h. After cooling, the bombs were opened and placed on a hotplate to evaporate the solutions at 200°C to dryness. The residue was then re-dissolved in 0·5 ml of HNO_3 and evaporated to dryness, followed by a second addition of HNO_3 and evaporation to dryness. The final residue was re-dissolved by adding 5 ml of HNO_3, re-sealing the bombs and returning them to the oven and heated at 130°C for 3 h. After cooling, the final solutions were put into plastic beakers and diluted in distilled H_2O to 50 ml before analysis.

The REE and trace element contents of the sample solutions were analysed by inductively coupled plasma mass spectrometry (ICP-MS) using a TJA PQ-ExCell system. Total procedural blanks were <50 ng for all the trace elements reported in Table 1. Internal standards of 10 ng ml^{-1} Rh and Re were added online. During the analytical runs, frequent standard calibrations were performed to correct for instrumental signal drift. Eight replicates and two international standards (GSR1 and GSD9) were prepared using the same procedure to monitor the analytical reproducibility. The discrepancy, based on repeated analyses of samples and international standards, is <10% relative for elements with abundances <10 ppm and <5% relative for those >10 ppm. Detailed sample preparation and analytical procedures follow those of He *et al.* (2002).

Sr–Nd–Pb isotopes

The sample powders were dissolved on a hot plate with 2 ml 10M HNO_3 and 10 ml 23M HF. The initial chemical separation of Sr and Nd followed standard ion exchange procedures and the solution was loaded into a quartz column packed with AG50WX8 (H+) (200–400 mesh) ion exchange resin. The REE fraction was further separated on a 2 ml column of Teflon powder coated with di-2-ethylhexyl phosphoric acid. Neodymium was eluted with 0·20 mol l^{-1} HCl.

The Sr isotope ratios were determined by thermal ionization mass spectrometry (TIMS) on a Finnigan MAT

Table 1: Major oxide (wt %) and trace element (ppm) compositions of Paleogene potassic felsic intrusions in western Yunnan

No.:	1	2	3	4	5	6	7	8	9	10
Sample:	LH-1	LH-2	LH-3·1	JC-1	JC-2	JC-9	JC-10·1	JC-10·2	BC-5	BC-7
Locality:	Liuhe	Liuhe	Liuhe	Jianchuan	Jianchuan	Jianchuan	Jianchuan	Jianchuan	Binchuan	Binchuan
Latitude:	26·45216	26·45901	26·43484	26·63232	26·63942	26·58424	26·58888	26·58888	25·79255	25·78979
Longitude:	100·32935	100·33203	100·31461	99·72533	99·73012	99·91970	99·91307	99·91307	100·47626	100·47727
Suite:	SHO	SHO	SHO	SHO	SHO	SHO	SHO	SHO	SHO	SHO
Lithology:	SP	SP	SP	AS	AS	AS	SP	SP	QMP	QMP
Age (Ma):	36·9			35·4		35·6			36·6	
SiO_2	62·60	62·40	63·57	61·75	62·55	62·04	61·06	61·47	64·80	64·63
TiO_2	0·63	0·70	0·55	0·56	0·52	0·62	0·66	0·62	0·40	0·39
Al_2O_3	14·52	14·61	14·24	14·12	14·34	14·82	14·74	14·76	16·30	16·31
Fe_2O_3	2·76	2·68	1·16	2·38	2·60	3·42	3·73	4·35	1·99	2·13
FeO	1·29	1·71	2·34	2·19	2·01	1·67	1·54	1·01	0·32	0·45
MnO	0·07	0·08	0·08	0·10	0·09	0·10	0·17	0·52	0·03	0·06
MgO	1·94	2·07	1·74	2·61	2·24	1·52	1·42	1·55	0·08	0·04
CaO	3·60	3·96	4·04	4·06	3·66	3·77	4·05	3·41	3·36	3·16
Na_2O	4·39	4·24	4·50	4·04	3·85	3·99	3·88	3·94	4·99	4·70
K_2O	6·21	6·25	5·92	6·55	6·60	6·46	6·76	6·58	5·54	5·61
P_2O_5	0·33	0·37	0·31	0·33	0·25	0·29	0·31	0·30	0·15	0·15
H_2O^+	0·84	0·68	0·80	0·42	0·26	0·62	0·64	0·66	1·32	1·44
CO_2	0·53	0·26	0·44	0·26	0·30	0·18	0·30	0·21	0·44	0·12
Sum	99·71	100·01	99·69	99·37	99·27	99·50	99·26	99·38	99·72	99·19
LOI	1·44	0·87	1·09	0·53	0·40	0·58	0·82	0·81	1·94	1·72
Mg#	0·48	0·47	0·48	0·52	0·48	0·37	0·34	0·36	0·06	0·03
K_2O/Na_2O	1·41	1·47	1·32	1·62	1·71	1·62	1·74	1·67	1·11	1·19
A/CNK	0·71	0·70	0·67	0·67	0·71	0·73	0·70	0·75	0·80	0·83
Li	22·5	17·5	22·8	18·1	12·0	23·2	26·4	24·0	15·9	12·2
Be	5·73	5·98	6·51	7·14	9·27	7·95	10·5	11·4	5·06	5·44
Sc	11·8	12·7	10·7	10·7	9·16	9·86	10·3	9·74	4·66	4·77
V	84·7	93·6	75·2	89·6	86·3	98·4	111	103	41·1	41·8
Cr	65·4	74·8	62·7	92·5	113	35·0	39·4	34·3	3·17	5·08
Co	11·9	13·0	11·6	13·5	11·6	10·4	10·6	10·7	2·45	3·03
Ni	30·9	34·8	29·7	42·6	37·8	13·1	13·8	17·9	1·44	1·88
Cu	42·9	28·7	54·4	12·4	9·69	27·9	43·8	32·6	7·54	7·18
Zn	62·3	69·7	51·5	63·9	53·8	78·2	96·0	109	46·3	47·7
Ga	19·9	19·4	20·5	19·5	20·7	20·9	20·8	21·9	20·0	20·0
Rb	240	224	209	273	304	259	268	262	202	198
Sr	880	722	766	1304	1209	1498	1595	1604	1229	1264
Y	17·6	18·2	15·7	22·4	22·5	30·3	32·3	34·8	18·0	18·8
Zr	197	205	178	124	192	268	262	266	221	223
Nb	10·0	10·4	9·33	9·92	10·9	12·8	12·2	12·6	9·64	9·65
Mo	0·50	0·47	0·25	0·69	0·85	1·08	0·75	0·84	1·08	2·54
Cs	3·66	2·9	2·89	10·1	8·60	8·18	9·05	5·58	8·47	8·65
Ba	2448	2470	2278	2133	2075	2374	2543	2829	2435	2382
La	30·6	32·2	28·2	45·2	42·8	56·4	55·1	65·9	35·6	38·8
Ce	60·3	63·5	55·3	86·5	82·9	116	108	118	61·4	67·5
Pr	6·68	7·06	6·07	9·09	8·95	12·2	11·9	12·5	7·42	7·89

(continued)

Table 1: Continued

No.:	1	2	3	4	5	6	7	8	9	10
Sample:	LH-1	LH-2	LH-3·1	JC-1	JC-2	JC-9	JC-10·1	JC-10·2	BC-5	BC-7
Locality:	Liuhe	Liuhe	Liuhe	Jianchuan	Jianchuan	Jianchuan	Jianchuan	Jianchuan	Binchuan	Binchuan
Latitude:	26·45216	26·45901	26·43484	26·63232	26·63942	26·58424	26·58888	26·58888	25·79255	25·78979
Longitude:	100·32935	100·33203	100·31461	99·72533	99·73012	99·91970	99·91307	99·91307	100·47626	100·47727
Suite:	SHO	SHO	SHO	SHO	SHO	SHO	SHO	SHO	SHO	SHO
Lithology:	SP	SP	SP	AS	AS	AS	SP	SP	QMP	QMP
Age (Ma):	36·9			35·4		35·6			36·6	
Nd	25·8	27·0	23·7	34·7	33·9	46·9	45·5	47·4	28·4	30·4
Sm	4·83	5·11	4·51	6·72	6·62	9·08	8·75	9·02	5·39	5·61
Eu	1·03	1·14	0·96	1·54	1·46	2·05	2·02	2·04	1·31	1·37
Gd	4·92	5·22	4·36	6·33	6·14	8·47	8·54	8·79	4·95	5·20
Tb	0·59	0·63	0·54	0·78	0·77	1·08	1·08	1·09	0·62	0·66
Dy	3·43	3·58	3·01	4·24	4·26	6·06	5·87	6·19	3·46	3·66
Ho	0·65	0·67	0·58	0·81	0·81	1·15	1·12	1·20	0·65	0·67
Er	1·89	1·92	1·63	2·31	2·30	3·22	3·23	3·39	1·84	1·93
Tm	0·26	0·27	0·23	0·32	0·32	0·45	0·44	0·47	0·25	0·26
Yb	1·65	1·72	1·50	2·13	2·21	2·96	2·88	3·16	1·75	1·78
Lu	0·25	0·26	0·21	0·33	0·32	0·43	0·44	0·48	0·26	0·27
Hf	5·38	5·59	5·11	4·02	5·38	6·80	6·43	6·59	5·44	5·49
Ta	0·62	0·63	0·62	0·71	0·78	0·93	0·89	0·92	0·60	0·60
Pb	32·0	28·1	36·3	38·4	34·3	47·2	61·3	66·6	31·4	28·6
Th	9·09	9·44	8·84	23·8	28·5	23·0	21·8	22·9	9·68	9·92
U	2·69	2·69	3·96	5·68	7·10	5·92	6·07	6·18	3·14	8·01
Eu/Eu*	0·65	0·67	0·66	0·72	0·70	0·71	0·71	0·70	0·78	0·78
Sr/Y	50·00	39·65	48·78	58·23	53·74	49·42	49·38	46·10	68·29	67·24
La/Yb	18·55	18·72	18·80	21·27	19·37	19·05	19·13	20·85	20·34	21·80
$(La/Yb)_n$	13·30	13·43	13·49	15·26	13·89	13·67	13·72	14·96	14·59	15·64
Dy/Yb	2·08	2·08	2·01	1·99	1·93	2·05	2·04	1·96	1·98	2·06

No.:	11	12	13	14	15	16	17	18	19	20
Sample:	BC-8	BC-9	BC-10	BC-11	BC-12	BC-13	BL-3	PTS	BY-YKD	SG-1
Locality:	Binchuan	Binchuan	Binchuan	Binchuan	Binchuan	Binchuan	Bailian	Songgui	Beiya	Shigu
Latitude:	25·78078	25·80592	25·80592	25·76942	25·76942	25·71875	26·14816	26·28732	26·16280	26·90149
Longitude:	100·44486	100·42872	100·42872	100·42663	100·42663	100·37181	100·22231	100·18642	100·18447	99·80072
Suite:	SHO	SHO	SHO	SHO	SHO	SHO	ADAK	ADAK	ADAK	ADAK
Lithology:	QMP	QMP	QMP	QMP	QMP	QMP	MGP	MGP	MGP	MGP
Age (Ma):								36·5	36·8	
SiO_2	63·22	62·30	62·41	64·04	62·75	64·24	70·15	70·32	70·36	70·30
TiO_2	0·48	0·54	0·54	0·43	0·47	0·47	0·22	0·24	0·30	0·28
Al_2O_3	15·99	15·88	15·58	16·26	16·16	15·48	15·47	14·96	15·59	15·04
Fe_2O_3	3·27	3·58	3·09	2·80	3·05	2·41	1·34	1·35	1·07	1·20
FeO	0·70	0·72	1·10	0·63	0·70	1·13	0·25	0·22	0·63	0·65
MnO	0·10	0·11	0·11	0·12	0·10	0·08	0·02	0·03	0·02	0·04
MgO	0·90	1·04	1·26	0·47	0·96	0·77	0·03	0·27	0·87	0·50
CaO	3·42	3·89	4·04	3·52	3·90	3·33	0·83	1·40	1·10	1·82
Na_2O	4·52	4·17	3·81	4·81	4·10	4·48	4·28	4·77	2·90	5·32

(continued)

Table 1: Continued

No.:	11	12	13	14	15	16	17	18	19	20
Sample:	BC-8	BC-9	BC-10	BC-11	BC-12	BC-13	BL-3	PTS	BY-YKD	SG-1
Locality:	Binchuan	Binchuan	Binchuan	Binchuan	Binchuan	Binchuan	Bailian	Songgui	Beiya	Shigu
Latitude:	25·78078	25·80592	25·80592	25·76942	25·76942	25·71875	26·14816	26·28732	26·16280	26·90149
Longitude:	100·44486	100·42872	100·42872	100·42663	100·42663	100·37181	100·22231	100·18642	100·18447	99·80072
Suite:	SHO	SHO	SHO	SHO	SHO	SHO	ADAK	ADAK	ADAK	ADAK
Lithology:	QMP	QMP	QMP	QMP	QMP	QMP	MGP	MGP	MGP	MGP
Age (Ma):								36·5	36·8	
K_2O	5·29	5·17	5·06	5·25	4·94	5·28	5·87	5·67	4·22	3·72
P_2O_5	0·18	0·23	0·22	0·16	0·18	0·26	0·02	0·09	0·04	0·11
H_2O^+	1·04	1·64	1·94	0·86	2·26	1·32	0·84	0·22	2·36	0·50
CO_2	0·26	0·26	0·12	0·14	0·21	0·23	0·18	0·09	0·35	0·18
Sum	99·37	99·53	99·28	99·49	99·78	99·48	99·5	99·63	99·81	99·66
LOI	1·18	1·61	2·01	1·06	2·26	1·52	0·89	0·24	2·79	0·58
Mg#	0·31	0·32	0·37	0·21	0·33	0·30	0·04	0·25	0·50	0·34
K_2O/Na_2O	1·17	1·24	1·33	1·09	1·20	1·18	1·37	1·19	1·46	0·70
A/CNK	0·83	0·81	0·82	0·81	0·84	0·81	1·04	0·91	1·37	0·93
Li	14·2	11·9	19·0	14·9	14·4	6·47	8·82	21·8	40·5	19·0
Be	5·32	5·21	5·07	5·39	4·80	5·32	3·62	7·00	3·87	4·30
Sc	7·76	9·04	9·00	5·68	7·71	6·90	2·17	3·96	3·61	3·52
V	60·0	70·1	70·3	48·1	58·7	56·1	16·4	19·5	28·6	27·2
Cr	35·3	14·8	17·4	7·24	14·8	7·21	1·98	3·25	27·7	4·29
Co	6·52	7·05	7·28	4·33	6·43	5·71	1·18	1·79	4·70	3·22
Ni	8·01	6·40	7·31	2·87	6·81	5·37	1·27	2·23	18·5	2·44
Cu	7·37	6·01	11·7	6·83	7·50	19·0	2·71	2·30	15·3	2·55
Zn	71·8	68·2	73·9	68·4	64·8	87·2	43·6	39·7	52·4	45·6
Ga	20·2	19·7	19·9	20·5	19·9	20·0	17·7	19·7	21·7	21·5
Rb	179	171	174	169	164	175	221	226	153	118
Sr	1438	1296	1387	1450	1285	1297	867	835	470	1250
Y	26·1	26·7	27·2	25·0	25·0	20·0	12·1	9·07	10·4	8·02
Zr	223	205	203	253	200	199	150	133	121	113
Nb	10·5	10·1	10·4	11·0	9·67	9·37	7·75	8·11	2·83	5·57
Mo	0·53	0·64	0·61	0·55	0·39	4·61	0·24	0·19	0·26	0·31
Cs	8·88	7·63	8·20	7·41	7·03	3·32	8·94	15·2	3·70	8·27
Ba	2452	2512	2500	2561	2278	2300	2264	2163	1312	1623
La	47·3	47·3	48·6	46·2	44·2	41·4	25·3	18·4	43·4	20·9
Ce	93·3	94·0	96·8	90·5	84·5	78·0	27·3	30·4	47·7	39·5
Pr	10·2	10·3	10·5	9·86	9·67	8·83	5·31	3·46	10·6	4·50
Nd	39·7	40·6	40·9	38·0	37·5	33·6	19·6	12·6	37·7	17·0
Sm	7·44	7·84	7·48	7·14	7·12	6·18	3·87	2·44	7·18	3·11
Eu	1·83	1·87	1·92	1·74	1·74	1·52	0·79	0·50	1·78	0·67
Gd	7·24	7·45	7·62	7·04	7·02	5·75	3·31	2·40	4·98	2·70
Tb	0·91	0·93	0·94	0·88	0·86	0·71	0·44	0·30	0·62	0·32
Dy	5·10	5·21	5·24	4·86	4·84	3·86	2·24	1·61	2·85	1·58
Ho	0·98	0·99	0·98	0·94	0·93	0·73	0·42	0·31	0·46	0·29
Er	2·75	2·84	2·81	2·60	2·64	2·05	1·14	0·84	1·15	0·78
Tm	0·38	0·39	0·38	0·36	0·37	0·28	0·15	0·12	0·14	0·10
Yb	2·54	2·50	2·47	2·46	2·45	1·83	0·88	0·77	0·86	0·71

(continued)

Table 1: Continued

No.:	11	12	13	14	15	16	17	18	19	20
Sample:	BC-8	BC-9	BC-10	BC-11	BC-12	BC-13	BL-3	PTS	BY-YKD	SG-1
Locality:	Binchuan	Binchuan	Binchuan	Binchuan	Binchuan	Binchuan	Bailian	Songgui	Beiya	Shigu
Latitude:	25·78078	25·80592	25·80592	25·76942	25·76942	25·71875	26·14816	26·28732	26·16280	26·90149
Longitude:	100·44486	100·42872	100·42872	100·42663	100·42663	100·37181	100·22231	100·18642	100·18447	99·80072
Suite:	SHO	SHO	SHO	SHO	SHO	SHO	ADAK	ADAK	ADAK	ADAK
Lithology:	QMP	QMP	QMP	QMP	QMP	QMP	MGP	MGP	MGP	MGP
Age (Ma):								36·5	36·8	
Lu	0·37	0·37	0·37	0·36	0·35	0·27	0·13	0·11	0·11	0·10
Hf	5·58	5·33	5·33	5·95	5·22	5·40	4·53	4·47	3·59	3·84
Ta	0·66	0·65	0·65	0·68	0·62	0·61	0·51	0·59	0·26	0·47
Pb	33·9	31·8	37·8	44·1	28·0	141	47·5	51·4	83·6	37·5
Th	12·9	12·3	12·7	12·3	11·7	12·5	12·0	10·4	8·45	8·00
U	4·28	4·07	4·07	3·40	3·74	5·19	2·80	2·41	3·48	2·34
Eu/Eu*	0·76	0·75	0·78	0·75	0·75	0·78	0·67	0·63	0·91	0·71
Sr/Y	55·08	48·53	50·98	58·00	51·40	64·84	71·65	92·04	45·19	155·86
La/Yb	18·62	18·92	19·68	18·78	18·04	22·68	28·75	23·90	50·47	29·44
$(La/Yb)_n$	13·36	13·57	14·11	13·47	12·94	16·27	20·62	17·14	36·20	21·11
Dy/Yb	2·01	2·08	2·12	1·98	1·98	2·11	2·55	2·09	3·31	2·23

No.:	21	22	23	24	25	26	27	28	29	30
Sample:	SG-3	SG-11	SG-12	SG-13	SG-14	JC-7	YS-1	DHS-1	DHS-2	DHS-4
Locality:	Shigu	Shigu	Shigu	Shigu	Shigu	Jianchuan	Yongsheng	Yongsheng	Yongsheng	Yongsheng
Latitude:	26·90446	26·78461	26·78186	26·77924	26·77790	26·65669	26·85138	26·84665	26·82191	26·85954
Longitude:	99·78879	99·77996	99·77637	99·77316	99·77171	99·81210	100·88572	100·98596	101·00521	100·97423
Suite:	ADAK	ADAK	ADAK	ADAK	ADAK	ADAK	ADAK	ADAK	ADAK	ADAK
Lithology:	MGP	MGP	MGP	MGP	MGP	MGP	QMP	QMP	QMP	QMP
Age (Ma):			35·7			35·3		33·1		34·1
SiO_2	70·01	71·49	71·02	69·10	68·82	71·34	65·57	62·94	67·05	67·96
TiO_2	0·28	0·24	0·24	0·27	0·25	0·24	0·49	0·55	0·36	0·38
Al_2O_3	15·44	15·30	15·14	15·51	13·95	14·94	15·00	15·67	15·11	14·72
Fe_2O_3	1·34	0·64	0·51	1·51	1·53	0·55	1·29	1·95	1·72	1·87
FeO	0·42	0·43	0·38	0·45	0·43	0·57	1·63	1·98	0·92	0·45
MnO	0·03	<0·01	<0·01	0·01	0·01	0·01	0·05	0·08	0·06	0·04
MgO	0·46	0·18	0·25	0·42	0·75	0·31	2·63	2·82	1·23	1·18
CaO	1·98	0·83	0·97	0·49	1·36	0·76	2·70	3·81	2·51	2·38
Na_2O	5·20	5·35	5·19	4·64	3·40	4·65	4·51	4·52	4·60	4·48
K_2O	3·87	4·62	4·61	6·25	6·42	4·68	4·15	4·15	4·43	4·11
P_2O_5	0·12	0·03	0·09	0·12	0·12	0·05	0·33	0·34	0·21	0·18
H_2O^+	0·46	0·74	0·68	0·58	1·54	0·98	0·92	0·48	1·08	1·12
CO_2	0·26	0·35	0·12	0·26	0·70	0·12	0·35	0·35	0·18	0·35
Sum	99·87	100·20	99·20	99·61	99·28	99·20	99·62	99·64	99·46	99·22
LOI	0·65	0·88	0·87	0·69	2·37	1·18	1·20	0·69	1·29	1·50
Mg#	0·34	0·24	0·35	0·29	0·43	0·34	0·63	0·58	0·47	0·50
K_2O/Na_2O	0·74	0·86	0·89	1·35	1·89	1·01	0·92	0·92	0·96	0·92
A/CNK	0·94	1·00	0·99	1·01	0·93	1·06	0·89	0·83	0·89	0·91
Li	22·2	3·55	6·92	7·61	11·9	26·3	26·6	14·5	22·1	30·9
Be	4·33	4·20	3·93	3·79	2·98	2·62	4·00	3·22	3·83	3·70

(continued)

Table 1: Continued

No.:	21	22	23	24	25	26	27	28	29	30
Sample:	SG-3	SG-11	SG-12	SG-13	SG-14	JC-7	YS-1	DHS-1	DHS-2	DHS-4
Locality:	Shigu	Shigu	Shigu	Shigu	Shigu	Jianchuan	Yongsheng	Yongsheng	Yongsheng	Yongsheng
Latitude:	26·90446	26·78461	26·78186	26·77924	26·77790	26·65669	26·85138	26·84665	26·82191	26·85954
Longitude:	99·78879	99·77996	99·77637	99·77316	99·77171	99·81210	100·88572	100·98596	101·00521	100·97423
Suite:	ADAK	ADAK	ADAK	ADAK	ADAK	ADAK	ADAK	ADAK	ADAK	ADAK
Lithology:	MGP	MGP	MGP	MGP	MGP	MGP	QMP	QMP	QMP	QMP
Age (Ma):			35·7			35·3		33·1		34·1
Sc	3·30	1·94	2·23	2·60	4·33	2·67	7·76	9·65	5·15	4·69
V	25·7	18·7	19·2	28·8	29·9	22·2	60·1	79·1	43·2	39·9
Cr	2·96	2·60	4·26	6·49	7·78	21·1	113	96·4	35·8	36·8
Co	3·10	1·16	1·18	1·22	4·40	2·28	11·8	13·9	7·04	6·80
Ni	1·99	1·33	1·34	2·98	6·94	3·45	55·0	53·8	21·4	23·5
Cu	2·57	24·8	123	327	12·2	4·38	13·8	28·4	16·8	10·5
Zn	37·4	19·6	21·5	23·0	18·6	34·3	51·9	59·2	52·9	44·1
Ga	22·2	21·5	22·2	21·8	19·2	20·6	20·2	19·9	19·6	20·2
Rb	123	165	164	194	277	177	139	107	128	124
Sr	1272	1086	827	486	328	448	813	1293	978	886
Y	8·53	4·47	6·09	6·63	8·67	4·26	11·8	15·5	13·1	8·88
Zr	119	112	103	109	102	107	189	187	192	148
Nb	5·88	5·74	5·72	5·89	5·93	3·02	6·31	7·93	8·03	6·43
Mo	0·41	2·44	26·5	18·9	1·03	0·35	0·34	2·62	0·77	1·15
Cs	9·95	3·52	3·10	2·96	3·64	8·01	3·30	2·69	5·97	3·36
Ba	1648	1714	1522	1905	2024	879	1510	2494	2335	1598
La	20·2	19·7	16·6	15·5	27·5	13·7	40·4	62·3	65·3	46·0
Ce	39·7	37·1	31·5	28·2	50·1	24·7	78·6	122	125	87·3
Pr	4·57	4·15	3·65	3·37	5·35	2·78	8·51	12·4	12·1	8·83
Nd	17·6	15·6	13·9	13·1	19·4	10·2	31·7	45·4	42·6	31·3
Sm	3·27	2·90	2·66	2·43	3·36	1·82	5·33	7·41	6·43	4·82
Eu	0·70	0·67	0·61	0·45	0·84	0·39	1·23	1·69	1·36	1·08
Gd	2·80	2·23	2·10	2·13	2·75	1·48	4·51	6·07	5·19	3·70
Tb	0·33	0·23	0·24	0·25	0·33	0·18	0·50	0·65	0·55	0·41
Dy	1·71	1·10	1·21	1·30	1·64	0·86	2·47	3·29	2·71	1·95
Ho	0·30	0·17	0·21	0·23	0·32	0·15	0·44	0·58	0·47	0·32
Er	0·83	0·46	0·58	0·66	0·88	0·43	1·21	1·59	1·33	0·89
Tm	0·12	0·06	0·07	0·09	0·12	0·05	0·16	0·21	0·17	0·12
Yb	0·73	0·42	0·52	0·61	0·77	0·37	1·01	1·36	1·15	0·74
Lu	0·12	0·06	0·07	0·09	0·12	0·05	0·14	0·19	0·17	0·11
Hf	3·99	3·88	3·51	3·75	3·23	3·41	5·28	5·09	5·30	4·31
Ta	0·50	0·48	0·47	0·48	0·45	0·36	0·47	0·53	0·62	0·51
Pb	44·6	27·3	49·5	13·6	9·90	29·9	35·4	30·9	40·9	37·6
Th	8·19	8·30	7·69	7·57	9·66	9·19	15·7	18·9	21·5	17·9
U	3·83	6·77	7·42	4·84	4·43	4·24	4·71	4·66	4·66	4·08
Eu/Eu*	0·71	0·81	0·79	0·60	0·84	0·73	0·77	0·77	0·72	0·78
Sr/Y	149·08	242·92	135·74	73·28	37·87	105·05	68·93	83·44	74·62	99·76
La/Yb	27·67	46·90	31·92	25·41	35·71	37·03	40·00	45·81	56·78	62·16
$(La/Yb)_n$	19·85	33·64	22·90	18·23	25·62	26·56	28·69	32·86	40·73	44·59
Dy/Yb	2·34	2·62	2·33	2·13	2·13	2·32	2·45	2·42	2·36	2·64

(continued)

Table 1: Continued

No.:	31	32	33	34	35	36	37	38	39	40
Sample:	SG-7	SG-8	SG-9	BC-2	BC-4	WS-4	WS-6	JC-5	JC-6	JC-11
Locality:	Shigu	Shigu	Shigu	Binchuan	Binchuan	Weishan	Weishan	Jianchuan	Jianchuan	Jianchuan
Latitude:	26·76011	26·76105	26·76114	25·77359	25·77359	25·15450	25·21489	26·64204	26·66078	26·61017
Longitude:	99·69240	99·69398	99·69589	100·65682	100·65682	100·28703	100·28093	99·75246	99·78047	99·81569
Suite:	ADAK	ADAK	ADAK	ADAK	ADAK	ADAK	ADAK	ADAK	ADAK	ADAK
Lithology:	QMP	QMP	QMP	QMP	QMP	QMP	QMP	QMP	QMP	QMP
Age (Ma):					35·4	35·4				
SiO_2	68·88	67·20	68·12	67·09	64·99	62·31	68·10	65·98	68·34	68·05
TiO_2	0·34	0·33	0·38	0·31	0·34	0·38	0·35	0·46	0·38	0·40
Al_2O_3	15·28	15·23	14·94	15·68	15·07	14·18	15·02	15·15	15·36	15·28
Fe_2O_3	1·57	1·58	1·64	1·56	1·95	0·93	1·43	1·79	1·60	1·71
FeO	0·81	0·70	0·84	1·29	2·68	1·74	1·01	1·56	0·93	0·95
MnO	0·05	0·04	0·06	0·02	0·08	0·05	0·04	0·05	0·05	0·06
MgO	0·82	0·79	0·81	1·14	1·18	1·65	1·12	1·10	0·83	0·85
CaO	2·17	1·93	1·99	1·07	1·21	3·57	2·40	2·55	1·72	2·18
Na_2O	5·22	5·27	5·38	4·24	4·07	3·55	4·57	4·33	5·07	4·90
K_2O	4·03	4·10	3·99	5·58	5·80	3·40	4·36	4·01	4·19	4·04
P_2O_5	0·16	0·16	0·17	0·22	0·22	0·17	0·14	0·18	0·18	0·19
H_2O^+	0·68	1·40	0·92	0·94	1·16	1·90	0·76	1·70	0·66	0·50
CO_2	0·21	1·32	0·26	0·18	0·35	5·35	0·12	0·53	0·12	0·12
Sum	100·22	100·05	99·50	99·32	99·10	99·18	99·42	99·39	99·43	99·23
LOI	0·85	1·94	1·28	0·95	1·44	7·17	0·82	2·13	0·70	0·58
Mg#	0·40	0·40	0·39	0·43	0·32	0·54	0·47	0·38	0·39	0·38
K_2O/Na_2O	0·77	0·78	0·74	1·32	1·43	0·96	0·95	0·93	0·83	0·82
A/CNK	0·90	0·92	0·89	1·05	0·99	0·89	0·90	0·94	0·96	0·93
Li	19·6	27·1	20·7	13·6	13·3	28·7	26·6	31·5	18·8	16·0
Be	4·05	3·94	3·83	3·44	3·44	4·52	5·14	3·50	4·18	3·74
Sc	4·74	4·45	5·24	4·34	4·74	6·05	5·09	6·67	4·90	5·26
V	38·7	37·1	43·4	35·0	43·2	49·0	40·4	52·2	42·3	43·6
Cr	8·80	7·97	9·37	28·1	36·4	51·5	40·3	28·5	8·42	7·59
Co	4·80	4·56	5·28	3·25	7·05	8·37	6·34	7·17	4·98	5·40
Ni	4·11	4·25	4·70	12·8	14·0	18·2	14·8	10·2	3·80	3·89
Cu	6·60	11·4	6·87	136	144	16·7	8·54	5·91	11·5	4·59
Zn	47·0	53·3	62·5	110	54·9	53·6	40·7	45·0	61·4	50·3
Ga	21·8	20·9	21·3	21·4	21·4	18·0	20·0	20·1	21·2	20·9
Rb	128	124	121	121	149	128	168	145	120	123
Sr	1305	886	1161	1404	1423	1063	1411	1071	1394	1379
Y	12·6	12·3	12·6	13·2	15·5	15·8	14·1	18·6	17·2	15·0
Zr	122	120	123	173	189	168	170	178	161	160
Nb	6·69	6·83	6·78	10·1	10·6	7·87	8·18	9·31	7·37	7·37
Mo	0·49	0·83	0·64	3·81	3·80	0·95	0·39	0·92	0·45	0·52
Cs	6·22	6·80	3·46	2·49	4·13	6·66	11·6	6·32	2·60	7·32
Ba	1763	1753	1736	3228	3118	3529	1405	2233	2141	2006
La	27·3	25·3	27·1	58·8	54·3	41·8	42·9	45·2	33·1	31·5
Ce	53·1	49·2	52·7	115	110	79·8	80·2	87·4	58·9	60·0
Pr	5·99	5·69	5·86	12·7	12·6	8·62	8·45	9·18	7·01	6·89

(continued)

Table 1: Continued

No.:	31	32	33	34	35	36	37	38	39	40
Sample:	SG-7	SG-8	SG-9	BC-2	BC-4	WS-4	WS-6	JC-5	JC-6	JC-11
Locality:	Shigu	Shigu	Shigu	Binchuan	Binchuan	Weishan	Weishan	Jianchuan	Jianchuan	Jianchuan
Latitude:	26·76011	26·76105	26·76114	25·77359	25·77359	25·15450	25·21489	26·64204	26·66078	26·61017
Longitude:	99·69240	99·69398	99·69589	100·65682	100·65682	100·28703	100·28093	99·75246	99·78047	99·81569
Suite:	ADAK	ADAK	ADAK	ADAK	ADAK	ADAK	ADAK	ADAK	ADAK	ADAK
Lithology:	QMP	QMP	QMP	QMP	QMP	QMP	QMP	QMP	QMP	QMP
Age (Ma):					35·4	35·4				
Nd	23·0	22·0	22·7	47·7	50·6	32·1	30·8	34·0	26·9	26·5
Sm	4·34	4·18	4·31	7·75	9·27	5·50	5·09	6·14	4·99	4·95
Eu	0·98	0·97	0·97	1·89	1·99	1·11	1·17	1·30	1·13	1·12
Gd	3·86	3·68	3·80	5·68	6·97	5·18	4·22	5·44	4·69	4·45
Tb	0·46	0·45	0·46	0·61	0·73	0·56	0·50	0·66	0·57	0·55
Dy	2·49	2·42	2·55	2·92	3·49	3·03	2·70	3·61	2·95	2·99
Ho	0·45	0·43	0·45	0·49	0·57	0·57	0·50	0·67	0·56	0·55
Er	1·27	1·21	1·28	1·29	1·54	1·64	1·39	1·84	1·54	1·53
Tm	0·17	0·17	0·18	0·16	0·19	0·22	0·19	0·25	0·20	0·21
Yb	1·14	1·08	1·17	1·07	1·31	1·47	1·31	1·63	1·38	1·37
Lu	0·17	0·17	0·17	0·16	0·19	0·21	0·19	0·25	0·21	0·20
Hf	4·01	3·94	4·08	4·48	4·81	4·82	4·79	4·89	4·69	4·73
Ta	0·53	0·56	0·54	0·59	0·62	0·71	0·71	0·71	0·57	0·57
Pb	49·8	48·9	60·3	31·6	44·7	25·2	55·2	39·6	71·9	46·7
Th	10·5	10·2	10·6	23·5	24·1	16·7	18·5	16·6	11·9	11·6
U	3·69	3·81	3·63	7·50	8·63	6·44	4·97	5·26	3·19	3·79
Eu/Eu*	0·73	0·75	0·73	0·87	0·76	0·64	0·77	0·69	0·71	0·73
Sr/Y	103·57	72·35	92·13	106·77	91·83	67·25	100·06	57·57	81·06	91·94
La/Yb	23·95	23·38	23·16	54·91	41·45	28·44	32·75	27·73	23·99	22·99
$(La/Yb)_n$	17·18	16·77	16·61	39·38	29·73	20·40	23·49	19·89	17·20	16·49
Dy/Yb	2·18	2·24	2·18	2·73	2·66	2·06	2·06	2·21	2·14	2·18

SHO, Shoshonitic suite; ADAK, adakite-like suite; SP, syenite porphyry; AS, amphibole syenite; MGP, monzogranite porphyry; QMP, quartz monzonite porphyry. Ages cited are SHRIMP zircon U–Pb dates from Lu *et al*. (2012). LOI, loss of ignition; $Mg\# = MgO/(MgO + FeO_T)$ in atomic ratio.

262 instrument equipped with a multi-collector at the Isotope Geology Laboratory of the Institute of Geology, Chinese Academy of Geological Sciences, Beijing. During the analytical period, several measurements of the NIST SRM 987 (formerly NBS 987) Sr reference standard gave $^{87}Sr/^{86}Sr = 0{\cdot}710232 \pm 15$ (2SE, $n = 6$) (the recommended value is 0·710240). Mass fractionations were corrected to $^{88}Sr/^{86}Sr = 8{\cdot}37521$. Detailed sample preparation and analytical procedures for Sr isotopic analysis follow those of Tang *et al*. (2007).

Nd isotope composition analyses were carried out by multicollector (MC)-ICP-MS on a Nu Instruments system at the Isotope Geology Laboratory of the Institute of Geology, Chinese Academy of Geological Sciences, Beijing. The international JMC321 Nd reference solution yielded a $^{143}Nd/^{144}Nd$ ratio of $0{\cdot}511124 \pm 10$ (2SE, $n = 8$; the recommended value is 0·511125) and the international JNdi-1 standard gave a $^{143}Nd/^{144}Nd$ ratio of $0{\cdot}512117 \pm 11$ (2SE, $n = 8$; the recommended value is 0·512115). Nd isotope ratios were internally corrected for mass fractionation using a constant value of 0·7219 for $^{146}Nd/^{144}Nd$ by the exponential law. Detailed sample preparation and analytical procedures for Nd isotopic analysis follow those of He *et al*. (2007). Total procedural blanks were about 10^{-9}–10^{-10} g Sr and 5×10^{-11} g Nd. The $^{87}Rb/^{86}Sr$ and $^{147}Sm/^{144}Nd$ ratios were calculated using the whole-rock Rb, Sr, Sm and Nd concentrations obtained by ICP-MS (Table 2).

Pb was separated and purified using AG1-X8 resin (200–400 mesh) anionic ion-exchange columns with dilute HBr as eluant. Pb isotopic ratios of samples were measured by MC-ICP-MS with a Nu Instruments system at the

Table 2: Sr–Nd–Pb isotope data for Paleogene potassic felsic intrusions in western Yunnan

Locality	Sample	Rock-type	$^{87}Rb/^{86}Sr$	$^{87}Sr/^{86}Sr$	±2σ	$(^{87}Sr/^{86}Sr)_i$	$^{147}Sm/^{144}Nd$	$^{143}Nd/^{144}Nd$	±2σ	$(^{143}Nd/^{144}Nd)_i$	$\varepsilon_{Nd}(t)$	T_{DM1} (Ma)	T_{DM2} (Ma)	$^{206}Pb/^{204}Pb$	$^{207}Pb/^{204}Pb$	$^{208}Pb/^{204}Pb$
Liuhe	LH-1	shoshonitic syenite	0·7884	0·707667	15	0·707275	0·1132	0·51235	5	0·512324	−5·25	1212	1272	18·589	15·659	38·899
Jianchuan	JC-1	shoshonitic syenite	0·6044	0·707339	23	0·707039	0·1171	0·512438	6	0·512411	−3·55	1123	1133	18·720	15·638	38·838
Jianchuan	JC-9	shoshonitic syenite	0·4994	0·707333	10	0·707085	0·1170	0·512597	10	0·512570	−0·44	872	881	18·700	15·637	38·821
Binchuan	BC-5	shoshonitic quartz monzonite	0·4764	0·706708	13	0·706471	0·1147	0·512446	5	0·512420	−3·38	1084	1120	18·554	15·614	38·661
Binchuan	BC-11	shoshonitic quartz monzonite	0·3380	0·70714	17	0·706972	0·1136	0·512429	7	0·512403	−3·71	1097	1146	18·540	15·608	38·639
Binchuan	BC-13	shoshonitic quartz monzonite	0·3908	0·707412	14	0·707218	0·1112	0·512414	5	0·512389	−3·99	1094	1169	18·542	15·615	38·670
Bailian	BL-3	adakite-like monzogranite	0·7375	0·707797	17	0·707430	0·1194	0·512378	10	0·512351	−4·73	1246	1229	18·651	15·665	38·983
Songgui	PTS	adakite-like monzogranite	0·7833	0·708187	8	0·707798	0·1171	0·512331	8	0·512304	−5·63	1290	1303	18·639	15·675	39·018
Beiya	BY-YKD	adakite-like monzogranite	0·9411	0·706449	18	0·705981	0·1151	0·512457	10	0·512431	−3·17	1071	1103	18·440	15·627	38·633
Shigu	SG-1	adakite-like monzogranite	0·2724	0·705732	11	0·705597	0·1106	0·512588	5	0·512563	−0·59	831	893	18·673	15·629	38·736
Jianchuan	JC-7	adakite-like monzogranite	1·1450	0·707596	14	0·707027	0·1079	0·512709	5	0·512684	1·78	636	700	18·652	15·619	38·679
Yongsheng	YS-1	adakite-like quartz monzonite	0·4931	0·70829	15	0·708045	0·1016	0·512415	5	0·512392	−3·93	1000	1165	18·223	15·596	38·456
Yongsheng	DHS-1	adakite-like quartz monzonite	0·2392	0·706435	12	0·706316	0·0987	0·512455	5	0·512432	−3·13	921	1100	18·238	15·587	38·413
Yongsheng	DHS-4	adakite-like quartz monzonite	0·4059	0·706123	14	0·705921	0·0931	0·512436	7	0·512415	−3·48	903	1129	18·168	15·587	38·390
Shigu	SG-7	adakite-like quartz monzonite	0·2828	0·705989	15	0·705848	0·1141	0·512561	9	0·512535	−1·13	901	937	18·676	15·629	38·742
Binchuan	BC-4	adakite-like quartz monzonite	0·3018	0·706575	12	0·706425	0·1107	0·512217	5	0·512192	−7·83	1379	1482	18·304	15·601	38·770
Weishan	WS-6	adakite-like quartz monzonite	0·3451	0·707517	16	0·707345	0·0999	0·512411	5	0·512388	−4·00	990	1171	18·808	15·651	38·874

$^{87}Rb/^{86}Sr$ and $^{147}Sm/^{144}Nd$ are calculated using whole-rock Rb, Sr, Sm and Nd values in Table 1. Chondritic Uniform Reservoir (CHUR) at the present day [$(^{87}Rb/^{86}Sr)_{CHUR} = 0{\cdot}0847$ (McCulloch & Black, 1984); $(^{87}Sr/^{86}Sr)_{CHUR} = 0{\cdot}7045$ (DePaolo, 1988); $(^{147}Sm/^{144}Nd)_{CHUR} = 0{\cdot}1967$ (Jacobsen & Wasserburg, 1980); $(^{143}Nd/^{144}Nd)_{CHUR} = 0{\cdot}512638$ (Goldstein *et al.*, 1984)] was used for the calculations. Nd depleted mantle model ages (T_{DM}) were calculated using $(^{147}Sm/^{144}Nd)_{DM} = 0{\cdot}2137$ and $(^{143}Nd/^{144}Nd)_{DM} = 0{\cdot}51315$ (Peucat *et al.*, 1989) at the present day. $\lambda_{Rb} = 1{\cdot}42 \times 10^{-11}$ a^{-1} (Steiger & Jäger, 1977); $\lambda_{Sm} = 6{\cdot}54 \times 10^{-12}$ a^{-1} (Lugmair & Marti, 1978). Initial $^{87}Sr/^{86}Sr$ ratios and $\varepsilon_{Nd}(t)$ values are corrected at $t = 35$Ma.

same laboratory as the Nd isotopic analysis. Thallium was used as an internal standard to correct the mass fractionation of Pb isotopes during analysis. During the period of analysis, repeated analyses of international standard NBS981 yielded ratios of $^{206}Pb/^{204}Pb = 16{\cdot}939 \pm 0{\cdot}013$ (the recommended value is 16·9356), $^{207}Pb/^{204}Pb = 15{\cdot}497 \pm 0{\cdot}011$ (the recommended value is 15·4891), and $^{208}Pb/^{204}Pb = 36{\cdot}712 \pm 0{\cdot}033$ (the recommended value is 36·7006; Todt *et al.*, 1996; 2σ). Detailed sample preparation and analytical procedures for the Pb isotope measurements follow those of He *et al.* (2005).

The single-stage Nd model age (T_{DM1}) was calculated assuming linear Nd isotopic growth of the depleted mantle reservoir from $\varepsilon_{Nd}(t) = 0$ at 4·56 Ga to +10 at the present time (Goldstein *et al.*, 1984):

$$T_{DM1} = 1/\lambda \ln\left\{1 + \left[\left(^{143}Nd/^{144}Nd\right)_S - 0{\cdot}51315\right] \Big/ \left[\left(^{147}Sm/^{144}Nd\right)_S - 0{\cdot}2137\right]\right\}$$

where subscript S indicates sample. The parameters used are listed in Table 2.

The two-stage Nd model age (T_{DM2}) is obtained using the equation

$$T_{DM2} = T_{DM1} - (T_{DM1} - t)(f_{cc} - f_s)/(f_{cc} - f_{DM})$$

where f_{cc}, f_s and f_{DM} are $f_{Sm/Nd}$ values of average continental crust, the sample and the depleted mantle, respectively. It is assumed in the equation that the protolith of the granitic magmas has a Sm/Nd ratio, or $f_{Sm/Nd}$ value, of the average continental crust (i.e. Sm/Nd = 0·115; Goldstein *et al.*, 1984); $f_{cc} = -0{\cdot}4$ and $f_{DM} = 0{\cdot}08643$, and $t = 35$ Ma was taken as the crystallization age of the felsic intrusions (Lu *et al.*, 2012).

Zircon oxygen isotopes

Zircons were extracted from rock samples by standard heavy liquid and magnetic separation techniques. Representative zircon grains were handpicked under a binocular microscope, mounted in epoxy resin discs, then polished and coated with gold. The internal structures of the zircons were then examined using cathodoluminescence (CL) techniques. CL imaging of all zircons was undertaken on a Zeiss 1555 VP-FESEM at the Centre for Microscopy, Characterisation and Analysis, University of Western Australia. Before the zircon oxygen isotopic analysis, U–Pb isotopic analyses were performed using the sensitive high-resolution ion microprobe (SHRIMP II) at the John de Laeter Centre for Mass Spectrometry, Curtin University. The detailed U–Pb analytical methods and the SHRIMP age data have been published previously by Lu *et al.* (2012). The SHRIMP zircon ages are cited in Tables 1 and 3.

Zircon oxygen isotope compositions were measured using the Cameca IMS 1280 large-radius SIMS at the Centre for Microscopy, Characterisation and Analysis, the University of Western Australia in Perth. The oxygen analysis spots were close to the SHRIMP pit within a domain of uniform CL texture on the same zircon. The Gaussian Cs^+ primary ion beam was accelerated to 10 kV, with an intensity of *c.* 2·5 nA and a spot diameter of about 20 μm. A normal-incidence electron flood gun was used to compensate for sample charging during analysis, with a homogeneous electron density over a 100 μm oval area. Negative secondary ions were extracted with a −10 kV potential. The field aperture was set to 4000 μm, and the transfer-optics magnification was 130. The energy slit width was 30 eV, with a 5 eV gap. The entrance slit width was 110 μm and exit slit width for multi-collector Faraday cups (FCs) for ^{16}O and ^{18}O was 500 μm (MRP ~2200). The intensity of $^{16}O^-$ was typically 2×10^9 c.p.s. Oxygen isotopes were measured in multi-collector mode using two off-axis Faraday cups. The nuclear magnetic resonance (NMR) probe was used for magnetic field control with stability.

Analysis time was about 3·75 min, consisting of 10 s pre-sputtering, automatic, secondary beam centering and 20×4 s integrations of oxygen isotope intensities. Uncertainties on single analyses are reported at the 2σ level and include propagation of uncertainties associated with calculation of instrumental mass fractionation, drift correction, and calculation of δ values relative to Vienna Standard Mean Ocean Water (V-SMOW). The internal precision of a single analysis was generally better than 0·15‰ for $^{18}O/^{16}O$ ratios. External precision was <0·20‰ for bracketing standards for all reported analyses. The $^{18}O/^{16}O$ ratios are reported in delta notation as $\delta^{18}O$ values, by normalizing to V-SMOW $(^{18}O/^{16}O)_{V\text{-}SMOW} = 0{\cdot}0020052$ (Baertschi, 1976). The internal standard used for correction of mass fractionation was Temora 2 zircon with a $\delta^{18}O$ value of 8·2 ± 0·01‰ (1SD) (Valley, 2003; Black *et al.*, 2004).

Zircon hafnium isotopes

Hf-isotope analyses were carried out *in situ* at GEMOC (Macquarie University) using a New Wave/Merchantek UP-213 laser-ablation microprobe attached to a Nu Plasma MC-ICP-MS system. The Hf analyses were made on the same spots as the previous oxygen isotope analyses. They were conducted with a beam diameter of ~55 μm and a 5 Hz repetition rate, resulting in total Hf signals of $(1–6) \times 10^{-11}$ A (depending on conditions and Hf contents). Typical ablation times were 100–120 s, resulting in ablation pits 40–60 μm deep. Helium carrier gas transported the ablated aliquot from the laser-ablation cell via a mixing chamber to the ICP-MS torch.

Interference of ^{176}Lu on ^{176}Hf is corrected by measuring the intensity of the interference-free ^{175}Lu isotope and

Table 3: Hf–O isotopic data for the magmatic zircons in the Paleogene potassic felsic intrusions in western Yunnan

Hf analysis no.	$^{176}Yb/^{177}Hf$	$^{176}Lu/^{177}Hf$	$^{176}Hf/^{177}Hf$	±σ	εHf(t)	±2σ	T_{DM2} (Ga)	$\delta^{18}O$ (‰)	± 2σ
LH-1 (Liuhe, shoshonitic syenite; 36·9±0·3 Ma)									
5	0·017271	0·000460	0·282741	0·000022	−0·7	1·5	1·13	5·79	0·29
7	0·065320	0·001120	0·282802	0·000022	1·4	1·5	1·00	7·43	0·24
13	0·028769	0·000669	0·282658	0·000022	−3·7	1·5	1·32	7·15	0·20
14	0·000883	0·000015	0·282881	0·000013	4·2	0·9	0·82	6·10	0·21
18	0·027687	0·000764	0·282630	0·000025	−4·7	1·8	1·38	7·42	0·26
Average					−0·7	1·5	1·13	6·78	0·24
JC-1 (Jianchuan, shoshonitic syenite; 35·4±0·3 Ma)									
1	0·101756	0·001734	0·282778	0·000015	0·5	1·1	1·05	6·76	0·42
2	0·101756	0·001734	0·282778	0·000015	0·5	1·1	1·05	5·97	0·31
3	0·050641	0·000913	0·282764	0·000009	0·0	0·6	1·08	6·92	0·42
4	0·097393	0·001724	0·282805	0·000008	1·5	0·6	0·99	6·63	0·52
5	0·081826	0·001454	0·282783	0·000011	0·7	0·8	1·04	6·84	0·30
6	0·031520	0·000578	0·282744	0·000008	−0·7	0·6	1·13	7·01	0·31
7	0·050084	0·000803	0·282762	0·000012	0·0	0·8	1·09	6·71	0·30
8	0·030801	0·000534	0·282761	0·000008	−0·1	0·6	1·09	6·94	0·43
9	0·077724	0·001357	0·282763	0·000008	0·0	0·5	1·08	6·85	0·28
10	0·039719	0·000708	0·282743	0·000007	−0·7	0·5	1·13	7·05	0·32
11	0·027342	0·000543	0·282724	0·000008	−1·4	0·5	1·17	6·58	0·30
12	0·195870	0·003056	0·282923	0·000016	5·6	1·1	0·73	7·23	0·31
13	0·035613	0·000675	0·282732	0·000010	−1·1	0·7	1·15	6·77	0·29
Average					0·4	0·7	1·06	6·79	0·35
JC-9 (Jianchuan, shoshonitic syenite; 35·6±0·3 Ma)									
1	0·024646	0·000430	0·282799	0·000011	1·3	0·8	1·00	6·44	0·27
2	0·041878	0·000705	0·282862	0·000013	3·5	0·9	0·86	6·31	0·40
3	0·021742	0·000391	0·282842	0·000012	2·8	0·8	0·91	6·63	0·43
4	0·035222	0·000614	0·282809	0·000009	1·6	0·6	0·98	6·88	0·35
5	0·022184	0·000407	0·282831	0·000013	2·4	0·9	0·93	6·86	0·22
6	0·022736	0·000411	0·282844	0·000010	2·9	0·7	0·90	6·57	0·23
7	0·024521	0·000423	0·282841	0·000010	2·8	0·7	0·91	6·26	0·28
8	0·030915	0·000571	0·282835	0·000011	2·5	0·8	0·92	6·63	0·38
9	0·033916	0·000622	0·282830	0·000009	2·4	0·6	0·93	6·51	0·35
10	0·038086	0·000689	0·282846	0·000013	2·9	0·9	0·90	6·48	0·27
11	0·060088	0·001049	0·282805	0·000012	1·5	0·8	0·99	6·81	0·27
Average					2·4	0·8	0·93	6·58	0·31
BC-5 (Binchuan, shoshonitic quartz monzonite; 36·6±0·4 Ma)									
1	0·051984	0·001254	0·282811	0·000035	1·7	2·5	0·98	6·41	0·33
2	0·095821	0·001880	0·282749	0·000037	−0·5	2·6	1·12	5·77	0·36
3	0·105240	0·001982	0·282760	0·000015	−0·1	1·1	1·09	6·24	0·31
4	0·046003	0·000901	0·282703	0·000022	−2·1	1·5	1·22	–	–
5	0·082364	0·001677	0·282778	0·000029	0·5	2·0	1·05	6·24	0·38
6	0·068522	0·001463	0·282829	0·000048	2·3	3·4	0·94	5·74	0·62
7	0·068088	0·001393	0·282680	0·000047	−2·9	3·3	1·27	6·28	0·60
Average					−0·2	2·3	1·09	6·11	0·43

(continued)

Table 3: Continued

Hf analysis no.	$^{176}Yb/^{177}Hf$	$^{176}Lu/^{177}Hf$	$^{176}Hf/^{177}Hf$	±σ	εHf(t)	±2σ	T_{DM2} (Ga)	$\delta^{18}O$ (‰)	± 2σ
PTS (Heqing, potassic adakite-like monzogranite; 36·5 ± 0·8 Ma)									
1	0·140188	0·002556	0·282996	0·000023	8·2	1·6	0·56	–	–
2	0·024559	0·000425	0·282781	0·000019	0·7	1·3	1·04	–	–
3	0·137572	0·002530	0·282716	0·000059	−1·7	4·1	1·19	–	–
7	0·073280	0·001167	0·282739	0·000048	−0·8	3·4	1·14	–	–
8	0·030855	0·000648	0·282816	0·000030	1·9	2·1	0·96	–	–
Average					1·6	2·5	0·98		
SG-12 (Shigu, potassic adakite-like monzogranite; 35·7 ± 0·2 Ma)									
1	0·041524	0·000838	0·282880	0·000029	4·1	2·0	0·82	6·13	0·28
2	0·023599	0·000506	0·282817	0·000031	1·9	2·2	0·96	5·59	0·29
4	0·026624	0·000587	0·282919	0·000026	5·5	1·8	0·73	5·05	0·54
6	0·041940	0·000922	0·282844	0·000029	2·9	2·0	0·90	5·25	0·23
8	0·103935	0·002222	0·282875	0·000032	3·9	2·2	0·83	4·98	0·29
9	0·039693	0·000870	0·282812	0·000023	1·7	1·6	0·97	5·10	0·23
10	0·035231	0·000933	0·282825	0·000019	2·2	1·3	0·94	5·38	0·26
11	0·051455	0·001093	0·282880	0·000027	4·1	1·9	0·82	4·78	0·26
12	0·028766	0·000627	0·282899	0·000029	4·8	2·0	0·78	5·33	0·31
14	0·040597	0·000863	0·282964	0·000021	7·1	1·5	0·63	5·24	0·26
15	0·095297	0·001694	0·282995	0·000040	8·2	2·8	0·56	5·16	0·24
18	0·029305	0·000611	0·282963	0·000030	7·1	2·1	0·63	5·45	0·18
19	0·021342	0·000455	0·282930	0·000036	5·9	2·5	0·71	5·23	0·27
Average					4·6	2·0	0·79	5·28	0·28
JC-7 (Jianchuan, potassic adakite-like monzogranite; 35·3 ± 0·4 Ma)									
1	0·016687	0·000304	0·282764	0·000010	0·0	0·7	1·08	6·77	0·22
3	0·013992	0·000259	0·282774	0·000009	0·4	0·6	1·06	6·79	0·29
5	0·024202	0·000441	0·282751	0·000010	−0·4	0·7	1·11	6·81	0·30
6	0·026800	0·000587	0·282873	0·000029	3·9	2·0	0·84	–	–
7	0·016814	0·000349	0·282845	0·000040	2·9	2·8	0·90	7·16	0·18
8	0·031020	0·000773	0·282792	0·000033	1·0	2·3	1·02	6·31	0·45
9	0·036291	0·000664	0·282875	0·000014	3·9	1·0	0·83	6·77	0·20
18	0·103448	0·001779	0·282821	0·000025	2·0	1·8	0·96	7·03	0·20
Average					1·7	1·5	0·97	6·80	0·26
DHS-1 (Yongsheng, potassic adakite-like quartz monzonite; 33·1 ± 0·4 Ma)									
1	0·043424	0·000738	0·282813	0·000009	1·7	0·6	0·97	6·67	0·27
2	0·062978	0·001103	0·282812	0·000013	1·7	0·9	0·98	6·28	0·29
4	0·079535	0·001312	0·282863	0·000013	3·5	0·9	0·86	6·45	0·42
5	0·058980	0·001024	0·282809	0·000010	1·6	0·7	0·98	6·54	0·36
6	0·050098	0·000888	0·282845	0·000013	2·8	0·9	0·90	6·60	0·48
8	0·052054	0·000901	0·282827	0·000012	2·2	0·8	0·94	6·21	0·32
9	0·273504	0·004003	0·282857	0·000019	3·2	1·3	0·88	6·26	0·45
11	0·060030	0·001028	0·282763	0·000009	−0·1	0·6	1·09	6·51	0·31
12	0·062794	0·001092	0·282817	0·000011	1·8	0·8	0·96	6·70	0·46
13	0·035268	0·000651	0·282800	0·000009	1·3	0·7	1·00	6·80	0·28
Average					2·0	0·8	0·96	6·50	0·36

(continued)

Table 3: Continued

Hf analysis no.	$^{176}Yb/^{177}Hf$	$^{176}Lu/^{177}Hf$	$^{176}Hf/^{177}Hf$	±σ	εHf(t)	±2σ	T_{DM2} (Ga)	$\delta^{18}O$ (‰)	± 2σ
DHS-4 (Yongsheng, potassic adakite-like quartz monzonite; 34·1±0·3 Ma)									
1	0·033015	0·000608	0·282806	0·000010	1·5	0·7	0·99	6·34	0·24
2	0·033446	0·000610	0·282793	0·000008	1·0	0·5	1·02	6·49	0·25
3	0·050139	0·000910	0·282823	0·000011	2·1	0·8	0·95	6·31	0·23
4	0·029156	0·000550	0·282876	0·000013	4·0	0·9	0·83	6·76	0·26
5	0·026388	0·000505	0·282811	0·000009	1·7	0·6	0·98	6·31	0·24
6	0·026198	0·000537	0·282864	0·000010	3·5	0·7	0·86	6·15	0·40
7	0·028411	0·000548	0·282799	0·000012	1·2	0·8	1·00	6·21	0·18
8	0·028809	0·000523	0·282847	0·000017	2·9	1·2	0·90	6·27	0·25
9	0·056744	0·001013	0·282832	0·000013	2·4	0·9	0·93	6·46	0·22
10	0·039805	0·000748	0·282825	0·000016	2·2	1·1	0·95	6·45	0·24
11	0·029818	0·000592	0·282813	0·000011	1·7	0·8	0·97	6·64	0·27
12	0·049569	0·000874	0·282791	0·000014	0·9	1·0	1·02	5·95	0·22
13	0·029347	0·000607	0·282765	0·000013	0·0	0·9	1·08	6·09	0·32
Average					1·9	0·8	0·96	6·34	0·25
BC-4 (Binchuan, potassic adakite-like quartz monzonite; 35·4±0·4 Ma)									
2	0·053157	0·001003	0·282704	0·000009	−2·1	0·6	1·22	6·07	0·34
3	0·051909	0·000973	0·282692	0·000011	−2·5	0·8	1·24	5·92	0·41
4	0·075637	0·001454	0·282679	0·000009	−3·0	0·6	1·27	5·81	0·41
5	0·053568	0·001040	0·282697	0·000008	−2·4	0·6	1·23	6·09	0·29
6	0·037304	0·000748	0·282698	0·000010	−2·3	0·7	1·23	5·67	0·49
7	0·051802	0·001018	0·282701	0·000010	−2·2	0·7	1·22	5·85	0·48
8	0·041593	0·000830	0·282709	0·000009	−1·9	0·6	1·21	5·98	0·40
9	0·041296	0·000773	0·282675	0·000016	−3·1	1·1	1·28	5·81	0·44
Average					-2·4	0·7	1·24	5·90	0·41
WS-4 (Weishan, potassic adakite-like quartz monzonite; 35·4±0·6 Ma)									
1	0·101853	0·001700	0·282909	0·000009	5·1	0·6	0·76	–	–
2	0·051088	0·001012	0·282923	0·000009	5·6	0·6	0·72	–	–
3	0·047388	0·000970	0·282908	0·000009	5·1	0·6	0·76	–	–
4	0·068468	0·001287	0·282895	0·000013	4·6	0·9	0·79	–	–
5	0·052113	0·000993	0·282873	0·000010	3·9	0·7	0·84	–	–
6	0·080200	0·001426	0·282893	0·000010	4·6	0·7	0·79	–	–
8	0·046327	0·000919	0·282871	0·000008	3·8	0·5	0·84	–	–
9	0·033000	0·000683	0·282852	0·000007	3·1	0·5	0·88	–	–
10	0·067596	0·001313	0·282859	0·000008	3·4	0·6	0·87	–	–
11	0·066715	0·001229	0·282869	0·000011	3·7	0·8	0·85	–	–
12	0·214074	0·003595	0·282997	0·000012	8·2	0·8	0·56	–	–
15	0·049783	0·000868	0·282822	0·000012	2·1	0·8	0·95	–	–
16	0·075012	0·001419	0·282901	0·000011	4·9	0·8	0·77	–	–
Average					4·5	0·7	0·80		
BNC-3 (Ninglang, potassic adakite-like granite; 32·5±0·3 Ma); whole-rock geochemistry not analysed									
1	0·040374	0·000747	0·282839	0·000011	2·6	0·8	0·91	5·92	0·22
3	0·054265	0·001048	0·282786	0·000015	0·7	1·1	1·03	5·87	0·23
4	0·043984	0·000799	0·282861	0·000010	3·4	0·7	0·87	5·58	0·27
5	0·024383	0·000492	0·282769	0·000011	0·1	0·8	1·07	6·03	0·34
6	0·026491	0·000514	0·282809	0·000011	1·6	0·8	0·98	5·69	0·29

(continued)

Table 3: Continued

Hf analysis no.	$^{176}Yb/^{177}Hf$	$^{176}Lu/^{177}Hf$	$^{176}Hf/^{177}Hf$	±σ	εHf(t)	±2σ	T_{DM2} (Ga)	$\delta^{18}O$ (‰)	± 2σ
7	0·029594	0·000570	0·282840	0·000009	2·7	0·6	0·91	5·98	0·28
8	0·057980	0·000882	0·282864	0·000017	3·5	1·2	0·86	6·25	0·25
9	0·051181	0·000990	0·282806	0·000014	1·4	1·0	0·99	5·95	0·31
11	0·029012	0·000383	0·282772	0·000010	0·3	0·7	1·06	5·84	0·50
12	0·027883	0·000504	0·282811	0·000018	1·6	1·3	0·98	5·95	0·21
14	0·044721	0·000920	0·282838	0·000019	2·6	1·3	0·92	5·54	0·39
15	0·032909	0·000681	0·282828	0·000017	2·2	1·2	0·94	5·56	0·24
16	0·049790	0·001011	0·282909	0·000020	5·1	1·4	0·76	5·44	0·21
17	0·057276	0·001156	0·282761	0·000022	−0·2	1·5	1·09	5·51	0·24
Average					2·0	1·0	0·96	5·79	0·28

$\varepsilon Hf(t) = 10000[(^{176}Hf/^{177}Hf)_S - (^{176}Lu/^{177}Hf)_S(e^{\lambda t} - 1)]/[(^{176}Hf/^{177}Hf)_{CHUR,0} - (^{176}Lu/^{177}Hf)_{CHUR}(e^{\lambda t} - 1)] - 1$. Values for $(^{176}Hf/^{177}Hf)_{CHUR,0}$ (0·282785) and $(^{176}Lu/^{177}Hf)_{CHUR}$ (0·0336) are from Bouvier *et al.* (2008). εHf(t) calculated using a Lu decay constant of $1{\cdot}865 \times 10^{-11}$ a^{-1} (Scherer *et al.*, 2001). Two-stage Hf model age (T_{DM2}) calculated using the initial $^{176}Hf/^{177}Hf$ ratios of the zircons and the depleted mantle, the U–Pb age and the $^{176}Lu/^{177}Hf$ ratios of the average continental crust ($^{176}Lu/^{177}Hf = 0{\cdot}015$; Griffin *et al.*, 2002). Present-day $^{176}Lu/^{177}Hf$ ratio and $^{176}Hf/^{177}Hf$ ratio of the depleted mantle are 0·0384 and 0·28325, respectively (Griffin *et al.*, 2000). —, Not measured. The crystallization age of each sample is given following sample lithology (Lu *et al.*, 2012).

using $^{176}Lu/^{175}Lu = 0{\cdot}02669$ (DeBievre & Taylor, 1993) to calculate $^{176}Lu/^{177}Hf$. Similarly, the isobaric interference of ^{176}Yb on ^{176}Hf has been corrected by measuring the interference-free ^{172}Yb isotope and using $^{176}Yb/^{172}Yb$ to calculate $^{176}Yb/^{177}Hf$. The appropriate value of $^{176}Yb/^{172}Yb$ was determined by spiking the JMC475 Hf standard with Yb, and determining the value of $^{176}Yb/^{172}Yb$ (0·58669) required to yield the value of $^{176}Hf/^{177}Hf$ obtained on the pure Hf solution. Detailed discussion regarding the overlap corrections for ^{176}Lu and ^{176}Yb has been provided by Pearson *et al.* (2008). The typical 2σ precision for the $^{176}Hf/^{177}Hf$ ratios of unknown samples reported here is 0·000020, equivalent to a 0·7 εHf unit. Two zircon standards, including Mud Tank and 91500, were analyzed to evaluate the accuracy of the laser-ablation results. During the whole session, Mud Tank yielded mean $^{176}Hf/^{177}Hf = 0{\cdot}282546 \pm 4$ (2σ; $n = 49$) (the recommended value is $0{\cdot}282530 \pm 30$) and 91500 gave mean $^{176}Hf/^{177}Hf = 0{\cdot}282366 \pm 22$ (2σ; $n = 4$) (the recommended value is $0{\cdot}282280 \pm 120$). Detailed analytical procedures have been given by Griffin *et al.* (2000, 2002).

For calculation of ε_{Hf} values we have adopted the chondritic values of Bouvier *et al.* (2008); that is, $^{176}Lu/^{177}Hf$ (CHUR, today) = 0·0336 and $^{176}Hf/^{177}Hf$ (CHUR, today) = 0·282785. We have also used the decay constant for ^{176}Lu of $1{\cdot}865 \times 10^{-11}$ a^{-1} in the ε_{Hf} calculation (Scherer *et al.*, 2001).

To calculate model ages (T_{DM}) based on a depleted-mantle source, we assume that the depleted mantle (DM) reservoir developed from an initially chondritic mantle, and is complementary to subsequent crustal extraction; that is, $^{176}Lu/^{177}Hf$ (DM, today) = 0·0384 and $^{176}Hf/^{177}Hf$ (DM, today) = 0·28325 (Griffin *et al.*, 2000). We have calculated, for each zircon, a 'crustal' model age (T_{DM2}; two-stage model age), which assumes that its parental magma was produced from an average continental crust (i.e. $^{176}Lu/^{177}Hf = 0{\cdot}015$) derived from depleted mantle (Griffin *et al.*, 2002).

RESULTS

Major element geochemistry

Major and trace element data are listed in Table 1. The shoshonitic syenites are characterized by high K_2O contents (5·9–6·8 wt %) and K_2O/Na_2O ratios (1·3–1·7) with A/CNK [i.e. molar ratio $Al_2O_3/(CaO + Na_2O + K_2O)$] ratios of 0·67–0·75 (Fig. 5; Table 1). Compared with the other felsic suites, the shoshonitic syenites have the lowest SiO_2 (61·1–63·6 wt %) and Al_2O_3 (14·1–14·8 wt %) contents, but the highest TiO_2, Fe_2O_3T (total Fe_2O_3), CaO and MgO contents (Fig. 6; Table 1).

The shoshonitic quartz monzonites have higher SiO_2 contents than the shoshonitic syenites, ranging from 62·3 to 64·8 wt %, as well as slightly lower K_2O contents (4·9–5·6 wt %), but higher A/CNK ratios of 0·80–0·84 (Fig. 5; Table 1). Compared with the syenites, they have higher Al_2O_3 contents (15·5–16·3 wt %), but lower TiO_2, Fe_2O_3T, CaO and MgO contents (Fig. 6; Table 1). They also have lower K_2O/Na_2O ratios than the syenites, ranging from 1·1 to 1·3 (Table 1). Collectively, these compositional characteristics are consistent with the shoshonitic quartz monzonites being more evolved than the syenites.

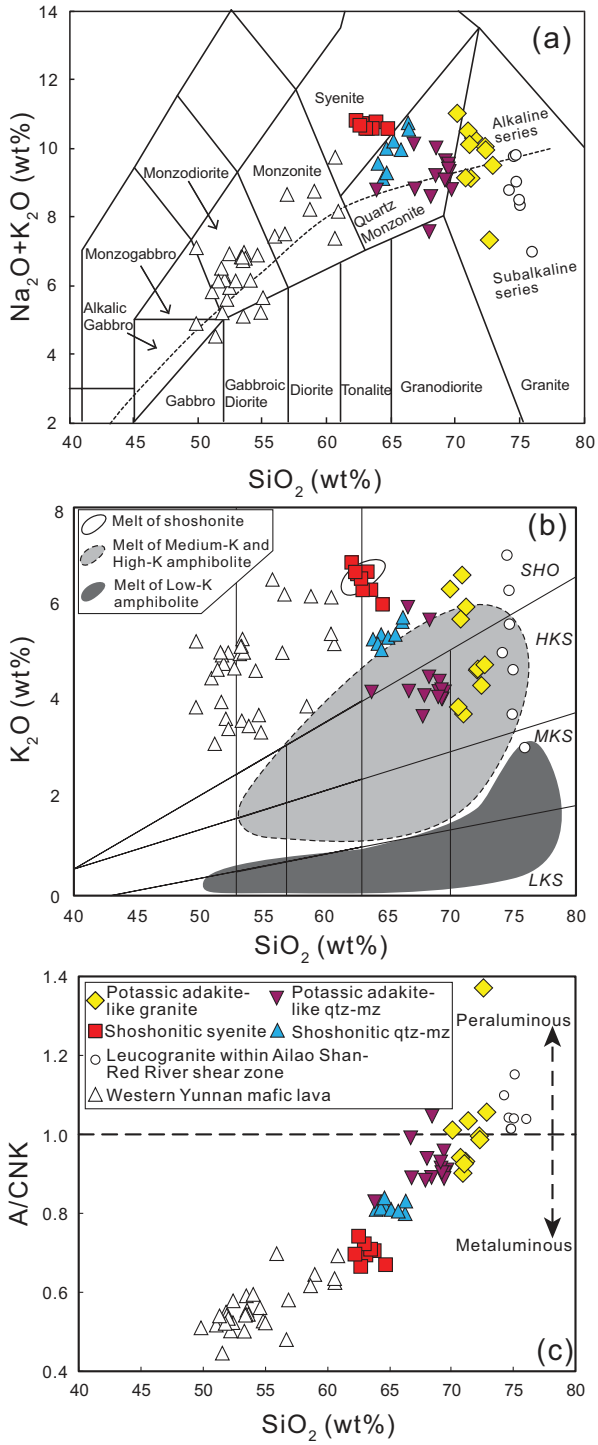

Fig. 5. Geochemical classification of potassic felsic intrusions in western Yunnan. (a) TAS diagram (Middlemost, 1994); the dashed line separating alkaline series from subalkaline series is from Irvine & Baragar (1971). (b) K_2O vs SiO_2 diagram, modified from Peccerillo & Taylor (1976) and Gill (1981). LKS, MKS, HKS and SHO are low-K tholeiite series, medium-K calc-alkaline series, high-K calc-alkaline series and shoshonitic series, respectively. The shaded fields represent experimental melts of low-K amphibolite at 3·2–0·6 GPa and 795–1150°C (Rapp *et al.*, 1991; Winther & Newton, 1991; Wolf & Wyllie, 1994; Rapp & Watson, 1995; Winther, 1996), of medium-K and high-K amphibolite at 3·2–0·7 GPa and 825–1150°C (Rapp *et al.*, 1991; Rushmer, 1991, 1993; Sen & Dunn, 1994; Rapp & Watson, 1995; Sisson *et al.*, 2005; Xiong *et al.*, 2005; Xiao & Clemens, 2007), and of shoshonite at 2·5–1·5 GPa and 1050–1075°C (Xiao & Clemens, 2007), respectively. (c) A/CNK [molar ratio $Al_2O_3/(CaO+Na_2O+K_2O)$] vs SiO_2 plot (Kemp & Hawkesworth, 2003). The rocks plotted for comparison include coeval Paleogene mafic lavas (Xu *et al.*, 2001*b*; Huang *et al.*, 2010) and leucogranites within the Ailao Shan–Red River shear zone (ASRR) in western Yunnan (Zhang & Schärer, 1999). All the major element data have been recalculated to 100 wt % on a volatile-free basis. qtz-mz, quartz monzonite.

Potassic adakite-like granites have the highest SiO_2 contents, ranging from 68·8 to 71·5 wt %, variable K_2O contents (3·7–6·4 wt %), and are transitional from subalkaline to alkaline, high-K calc-alkaline to shoshonitic with A/CNK ratios of 0·91–1·06 (Fig. 5; Table 1). These granites have high Al_2O_3 contents (14–15·6 wt %), but the lowest TiO_2, Fe_2O_3T, CaO and MgO contents, and variable K_2O/Na_2O ratios ranging from 0·7 to 1·9 (Fig. 6; Table 1).

Potassic adakite-like quartz monzonites have lower SiO_2 contents than the granites, ranging from 62·3 to 68·9 wt %, variable K_2O contents (3·4–5·8 wt %), are transitional from subalkaline to alkaline, and high-K calc-alkaline to shoshonitic, with A/CNK ratios of 0·83–1·05 (Fig. 5; Table 1). Compared with the granites, they have similar Al_2O_3 contents (14·2–15·7 wt %), but higher TiO_2, Fe_2O_3T, CaO and MgO contents, and variable K_2O/Na_2O ratios ranging from 0·7 to 1·4 (Fig. 6; Table 1).

The shoshonitic syenites and quartz monzonites lie on an extension of the coeval shoshonitic mafic lava trends on Harker diagrams, signifying a potential comagmatic relationship, whereas the potassic adakite-like quartz monzonites and granites show different trends from the shoshonitic suites (Figs 5 and 6). The two different trends are also highlighted in the Mg# vs SiO_2 and MgO vs SiO_2 diagrams shown in Fig. 7a and b, suggesting different origins for the two suites of rocks.

Trace element geochemistry

The shoshonitic and potassic adakite-like suites have distinct trends on Ni vs SiO_2 and Cr vs SiO_2 plots. For example, the shoshonitic syenites and quartz monzonites have decreasing Ni (from 42·6 to 1·4 ppm) and Cr (from 113 to 3 ppm) with SiO_2. However, the potassic adakite-like quartz monzonites and granites have similar Ni (from 55 to 1·3 ppm) and Cr (from 113 to 2 ppm) contents to the shoshonitic syenites and quartz monzonites, respectively, despite the much higher SiO_2 contents in the adakite-like suites (Fig. 7c and d; Table 1).

Both shoshonitic and potassic adakite-like suites are enriched in highly incompatible trace elements such as the light rare earth elements (LREE), and large-ion lithophile

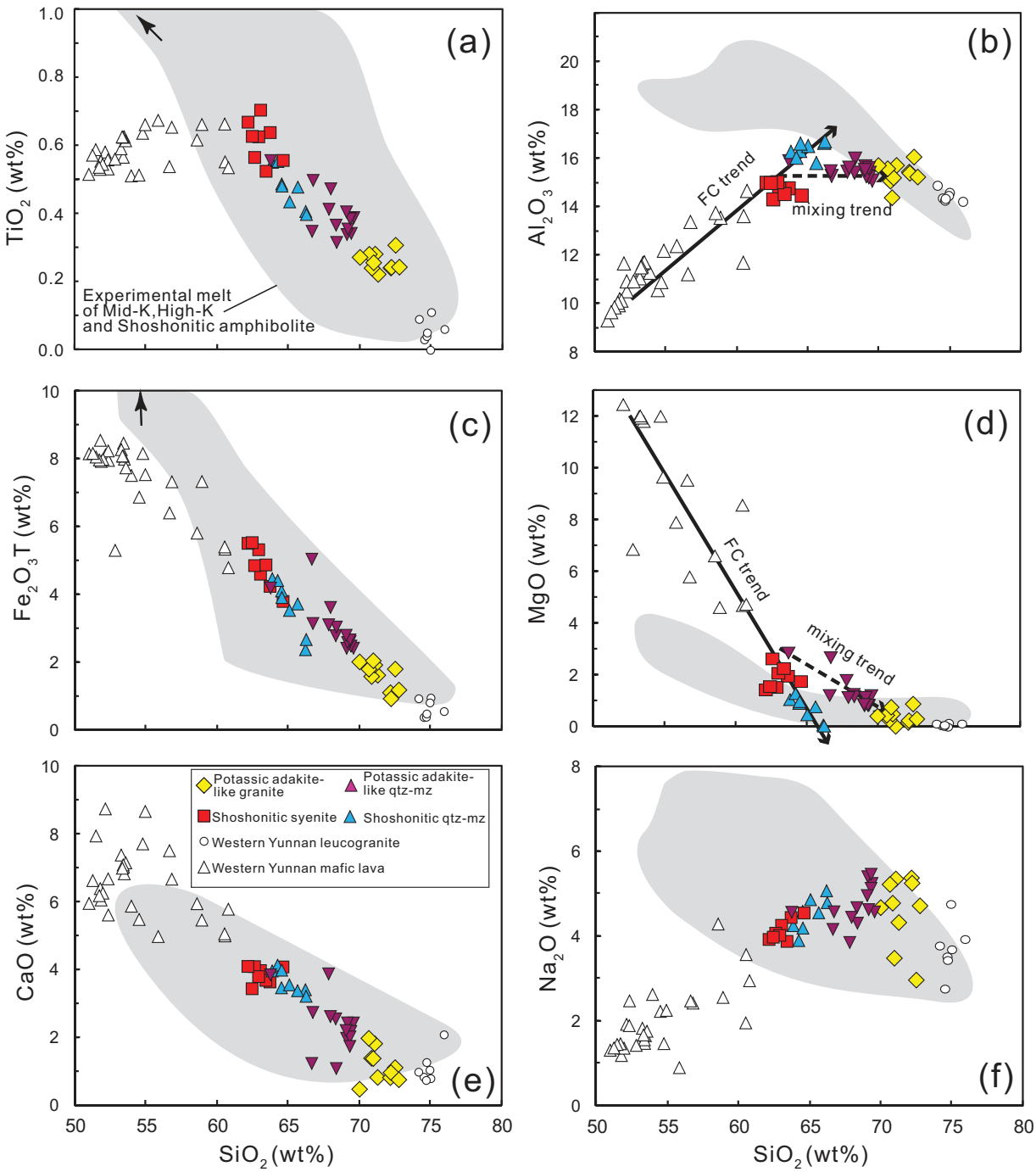

Fig. 6. Harker variation diagrams showing the major element compositions of the potassic felsic intrusions in western Yunnan. Grey fields represent experimental partial melts of medium-K, high-K and shoshonitic amphibolite at 0·6–3·2 GPa; the short black arrows in (a) and (c) indicate that some experimental data are out of the plot area. Long black arrows in (b) and (d) highlight the fractional crystallization (FC) trends for shoshonitic mafic lava, shoshonitic syenite and quartz monzonite; dashed black arrows in (b) and (d) indicate a magma mixing trend for potassic adakite-like quartz monzonite. Data sources as in Fig. 5. qtz-mz, quartz monzonite.

elements (LILE: Rb, Ba, K), but are depleted in Nb, Ta, P and Ti relative to neighboring REE (Fig. 8).

The shoshonitic syenites and quartz monzonites are characterized by high heavy rare earth element (HREE) contents (e.g. 15·7–34·8 ppm Y, 1·50–3·16 ppm Yb), resulting in lower Sr/Y (40–68) and La/Yb (18–23) ratios than the potassic adakite-like suites and plot outside the adakite fields (Fig. 9). However, both shoshonitic syenites and

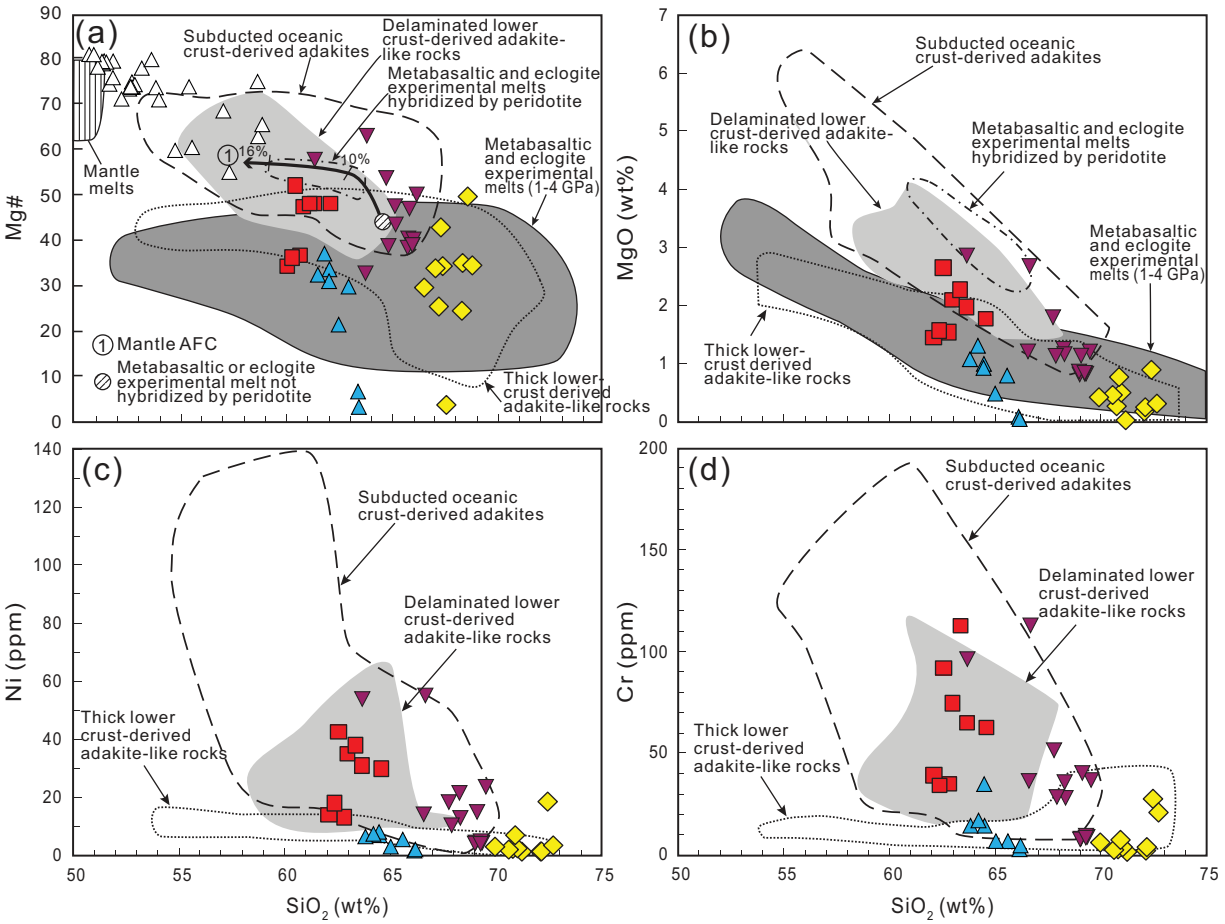

Fig. 7. (a) Mg-number (Mg#) vs SiO_2 (wt %); (b) MgO (wt %) vs SiO_2 (wt %); (c) Ni (ppm) vs SiO_2 (wt %); (d) Cr (ppm) vs SiO_2 (wt %). Mantle AFC curve in (a) is after Rapp *et al.* (1999) with the percentage of assimilated peridotite shown. The starting point represents the composition of a metabasaltic or eclogite experimental melt not hybridized with peridotite (Rapp *et al.*, 1999). Fields of subducted oceanic crust-derived adakites, thick lower crust-derived adakite-like rocks, delaminated lower crust-derived adakite-like rocks and metabasaltic and eclogite experimental melts hybridized with peridotite are after Wang *et al.* (2006*b*). Legend as in Fig. 6.

quartz monzonites overlap the field of coeval shoshonitic mafic lavas on the Sr/Y vs Y and La/Yb vs Yb plots in Fig. 9. Both shoshonitic suites show variable Eu anomalies (Eu/Eu*) of 0·65–0·78, and nearly flat HREE patterns with uniform Dy/Yb ratios of 1·9–2·1 (Figs 8a–d and 10).

Potassic adakite-like granites are characterized by high Sr (328–1272 ppm) but low Y (4·3–12·1 ppm) and Yb (0·37–0·88 ppm) contents, with elevated Sr/Y (38–243) and La/Yb (24–50) ratios. Similarly, potassic adakite-like quartz monzonites have high Sr (813–1423 ppm), slightly higher Y (8·9–18·6 ppm) and Yb (0·74–1·63 ppm) than the granites, but similar Sr/Y (58–107) and La/Yb (23–62) ratios (Table 1; Fig. 9). Both suites plot in the adakite field owing to their high Sr/Y and La/Yb ratios and low Y and Yb contents (Fig. 9). Compared with the shoshonitic suites, the potassic adakite-like granites and quartz monzonites have lower HREE contents and fractionated HREE patterns with larger and variable Dy/Yb ratios (2·1–3·3) (Table 1; Fig. 10), and Eu/Eu* varies from 0·6 to 0·9 (Table 1; Figs. 8e,g).

Sr–Nd–Pb isotopes

Whole-rock Sr–Nd–Pb isotopic data for the shoshonitic and potassic adakite-like suites are listed in Table 2 and plotted in Fig. 11. The shoshonitic syenites and quartz monzonites have a wide range in Sr [$(^{87}Sr/^{86}Sr)_i = 0{\cdot}7065$–$0{\cdot}7073$] and Nd [$\varepsilon_{Nd}(t) = -5{\cdot}3$ to $-0{\cdot}4$] isotope compositions. Compared with the shoshonitic suites, the potassic adakite-like granites and quartz monzonites have even larger variations in Sr [$(^{87}Sr/^{86}Sr)_i = 0{\cdot}7056$–$0{\cdot}7080$] and Nd [$\varepsilon_{Nd}(t) = -7{\cdot}8$ to $1{\cdot}8$] isotope compositions. The shoshonitic syenites and quartz monzonites have uniform two-stage Nd-isotope depleted mantle model ages (T_{DM2}) ranging from 1·3 to 1·1 Ga, except for syenite sample JC-9, which has a younger model age of *c.* 0·9 Ga. The potassic adakite-like suites have a larger variation in T_{DM2}, which

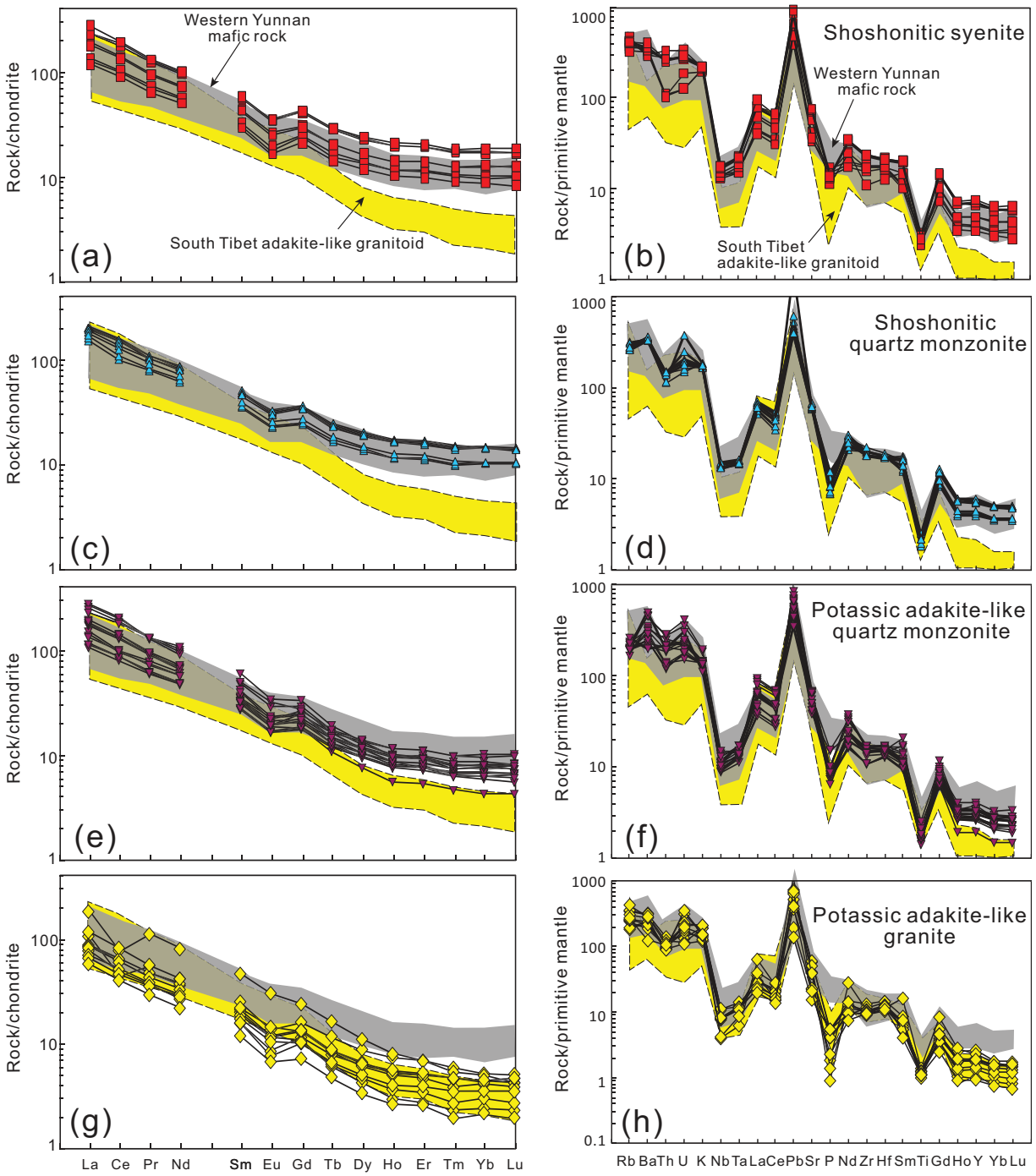

Fig. 8. Chondrite-normalized rare earth element (REE) patterns and primitive mantle normalized multi-element diagrams for the potassic felsic intrusions in western Yunnan. Shaded fields without outline are for coeval mafic volcanic rocks in western Yunnan (Xu *et al.*, 2001*b*; Li *et al.*, 2002; Huang *et al.*, 2010) and fields with dashed outline are typical South Tibet adakite-like rocks derived by partial melting of thickened lower crust (Chung *et al.*, 2003). Chondrite and primitive mantle normalizing values are from Sun & McDonough (1989).

ranges from 1·3 to 0·7 Ga for adakite-like granites, and from 1·5 to 0·9 Ga for adakite-like quartz monzonites (Fig. 11a and b; Table 2).

Both the shoshonitic and adakite-like suites have radiogenic $^{207}Pb/^{204}Pb$ (15·57–15·68) and $^{208}Pb/^{204}Pb$ (38·83–39·06) compositions, plotting well above the Northern Hemisphere Reference Line (NHRL, Hart, 1984; Fig. 11c and d). The shoshonitic syenites and quartz monzonites have relatively uniform $^{206}Pb/^{204}Pb$ (18·54–18·72), $^{207}Pb/^{204}Pb$ (15·61–15·66) and $^{208}Pb/^{204}Pb$ (38·64–38·90)

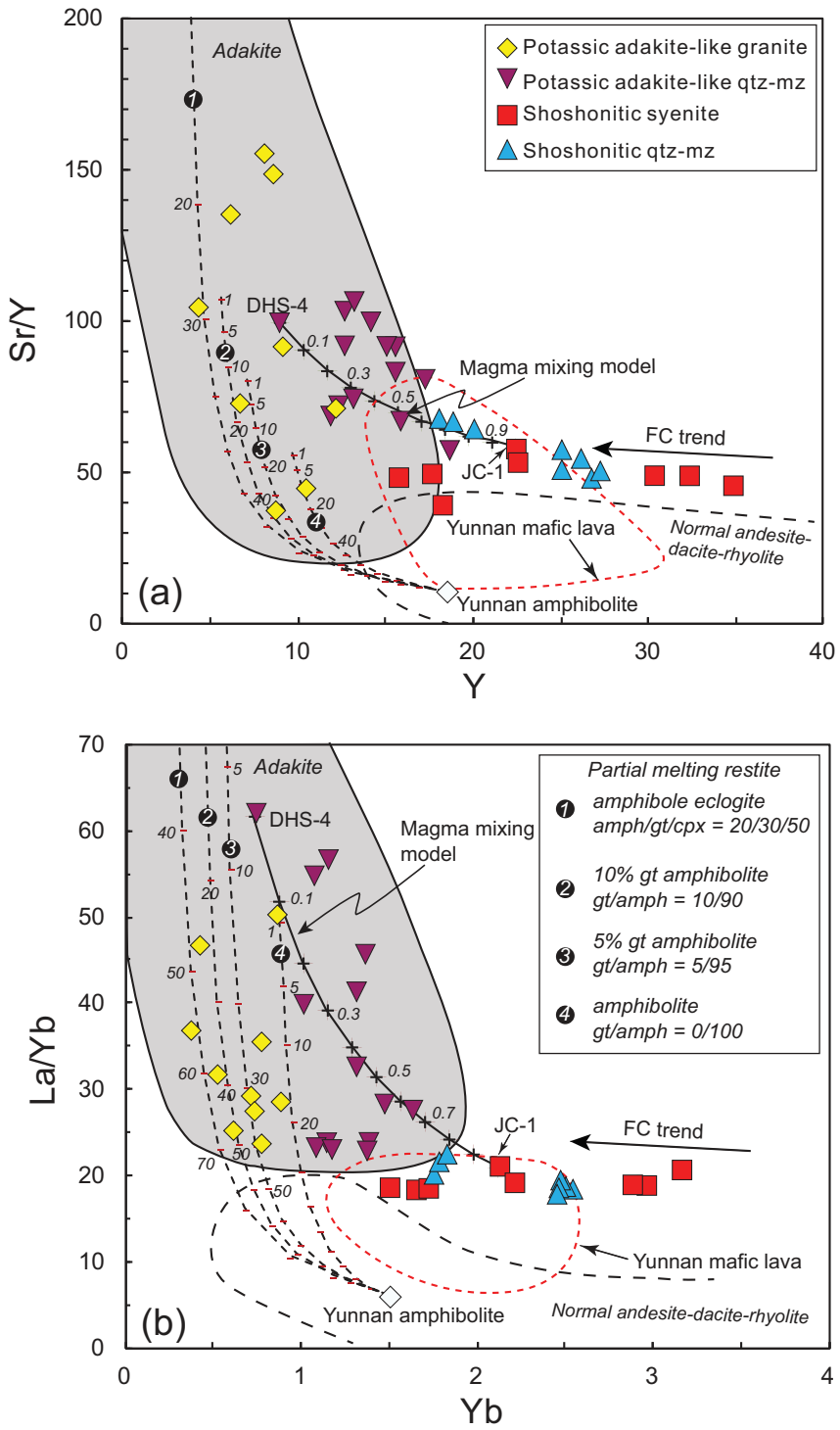

Fig. 9. Variation of (a) Sr/Y vs Y and (b) La/Yb vs Yb, showing the results of batch-melting modeling and magma mixing. The four dashed curves represent melting leaving a restite of amphibole eclogite, 10% garnet amphibolite, 5% garnet amphibolite and garnet-free amphibolite, respectively, based on a shoshonitic amphibolite xenolith from Liuhe, western Yunnan, as the starting composition (LH14b, Wang *et al.*, 2003). The melt percentage is shown next to the melting curves. The continuous-line curve represents a magma mixing model using sample DHS-4 and JC-1 as the felsic and mafic endmembers, respectively. Numbers beside the mixing curve indicate the weight fraction (F) of the mafic endmember in the mixture. The fractional crystallization (FC) trend for the shoshonitic suite is shown schematically. Dotted field is of Paleogene mafic volcanic rocks in western Yunnan (Xu *et al.*, 2001*b*; Li *et al.*, 2002; Huang *et al.*, 2010). Fields of adakite and normal andesite–dacite–rhyolite are after Richards & Kerrich (2007). Batch-melting modeling calculations follow Haschke *et al.* (2002, 2010) and magma mixing modeling follows Schwartz *et al.* (2011). qtz-mz, quartz monzonite.

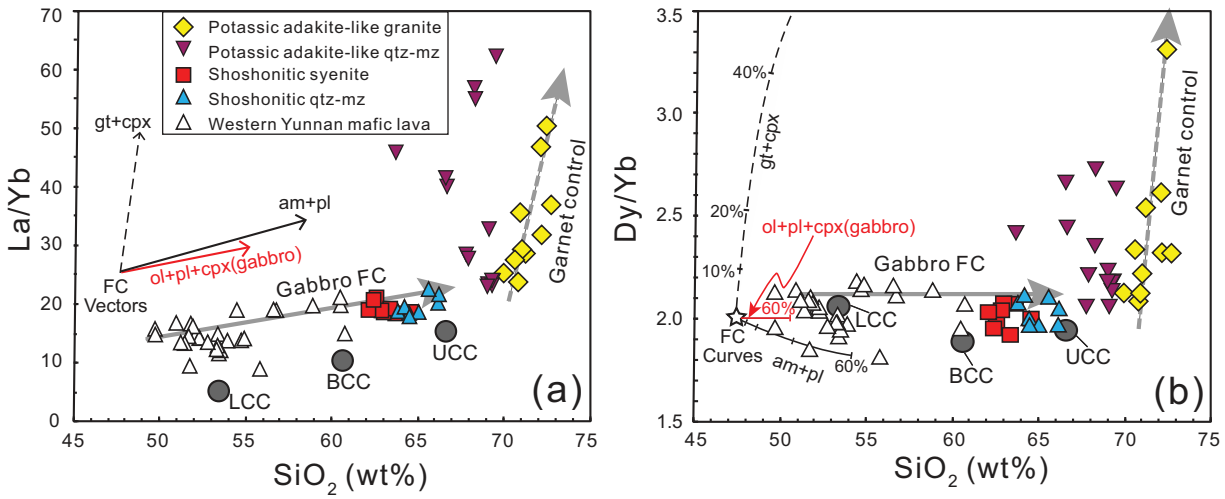

Fig. 10. Variation of (a) La/Yb vs SiO_2 and (b) Dy/Yb vs SiO_2. Fractional crystallization (FC) vectors of gt + cpx, am + pl, and ol + pl + cpx(gabbro) in (a) are from Davidson *et al.* (2007). FC models (showing per cent crystallization) of gt + cpx, ol + pl + cpx(gabbro) and am + pl in (b) are after Macpherson (2008). The thick grey continuous-line arrows represent gabbro-dominated fractionation (gabbro FC) for the shoshonitic suite; the grey dashed arrows highlight the garnet control for the potassic adakite-like granite. gt, garnet; ol, olivine; pl, plagioclase; cpx, clinopyroxene; am, amphibole. The compositions of lower continental crust (LCC), bulk continental crust (BCC), and upper continental crust (UCC) are plotted for comparison (Rudnick & Gao, 2003). Data for western Yunnan mafic lavas are from Xu *et al.* (2001*b*) and Huang *et al.* (2010). qtz-mz, quartz monzonite.

ratios. However, the potassic adakite-like granites and quartz monzonites have wider ranges in $^{206}Pb/^{204}Pb$ (18·17–18·81), $^{207}Pb/^{204}Pb$ (15·59–15·67), and $^{208}Pb/^{204}Pb$ (38·39–39·02) ratios.

Notwithstanding differences in Sr–Nd–Pb isotope compositions between the shoshonitic and potassic adakite-like suites, both suites are generally well within the range of coeval potassic mafic rocks in western Yunnan (Fig. 11). Furthermore, both shoshonitic and adakite-like suites share similar Sr–Nd–Pb isotopic compositions with the amphibolite xenoliths hosted by the potassic felsic intrusions in western Yunnan (Fig. 11; Deng *et al.*, 1998; Zhao *et al.*, 2004). Both felsic suites and potassic mafic counterparts are distinct from shallow crustal-derived leucogranites emplaced between 32 and 22 Ma within the Ailao Shan–Red River shear zone (Searle *et al.*, 2010), which have highly radiogenic Sr–Nd–Pb isotope compositions that are consistent with melts of older crust (Zhang & Schärer, 1999; Fig. 11).

Zircon Hf–O isotopes

In situ zircon Hf and O isotopic analyses of both shoshonitic and potassic adakite-like felsic intrusions are listed in Table 3. Representative zircon CL images are presented in Fig. 12, and Hf–O isotope variations are reported in Figs 13–15.

CL images show that xenolith-bearing shoshonitic syenite (sample LH-1) contains inherited zircons with or without younger magmatic overgrowths. These inherited zircons have U–Pb ages ranging from 2481 to 250 Ma (Figs 12a and 13; Lu *et al.*, 2012). In contrast, no inherited zircons were found in two xenolith-free shoshonitic syenites (samples JC-1 and JC-9, Fig. 12b and c). The Tertiary magmatic zircons in the three shoshonitic syenite samples, however, have similar zircon εHf and $\delta^{18}O$ values (Figs 13, 14a and 15; Table 3). For example, the average magmatic zircon εHf and $\delta^{18}O$ values for the three samples range from −0·7 to 2·4 and 6·58 to 6·79‰, respectively (Fig. 15; Table 3). The average zircon two-stage Hf mantle model ages (T_{DM2}) range from 1·1 to 0·9 Ga (Table 3).

Similarly, xenolith-bearing shoshonitic quartz monzonite (sample BC-5) has inherited zircons with U–Pb ages of *c.* 750 Ma (Fig. 12d; Lu *et al.*, 2012). The Tertiary magmatic zircons in this quartz monzonite have similar εHf and $\delta^{18}O$ values to those of the shoshonitic syenites, averaged at −0·2 and 6·11‰, respectively (Figs 13, 14a and 15; Table 3). Zircon two-stage Hf mantle model ages (T_{DM2}) for BC-5 range between 1·3 and 0·9 Ga, averaged at 1·1 Ga (Table 3).

No inherited zircon was found in any of the four potassic adakite-like quartz monzonites sampled (Fig. 12e–h), and Tertiary magmatic zircons in these samples have narrow εHf and $\delta^{18}O$ ranges. For example, sample DHS-1 has zircon εHf values of 0·4–3·9 and $\delta^{18}O$ values of 6·21–6·80‰, sample DHS-4 has zircon εHf values of 0·5–4·4 and $\delta^{18}O$ values of 5·95–6·76‰, and sample BC-4 has uniform but slightly lower εHf values between −2·7 and −1·5 and $\delta^{18}O$ values of 5·67–6·09‰ (Figs 13 and 14; Table 3). Zircon two-stage Hf mantle model ages (T_{DM2}) for these samples collectively span the range 1·3–0·7Ga (Table 3).

The potassic adakite-like granites have abundant inherited zircon with U–Pb ages clustered at *c.* 250 Ma and 900–850 Ma (Figs 12i–l and 13; Lu *et al.*, 2012). The

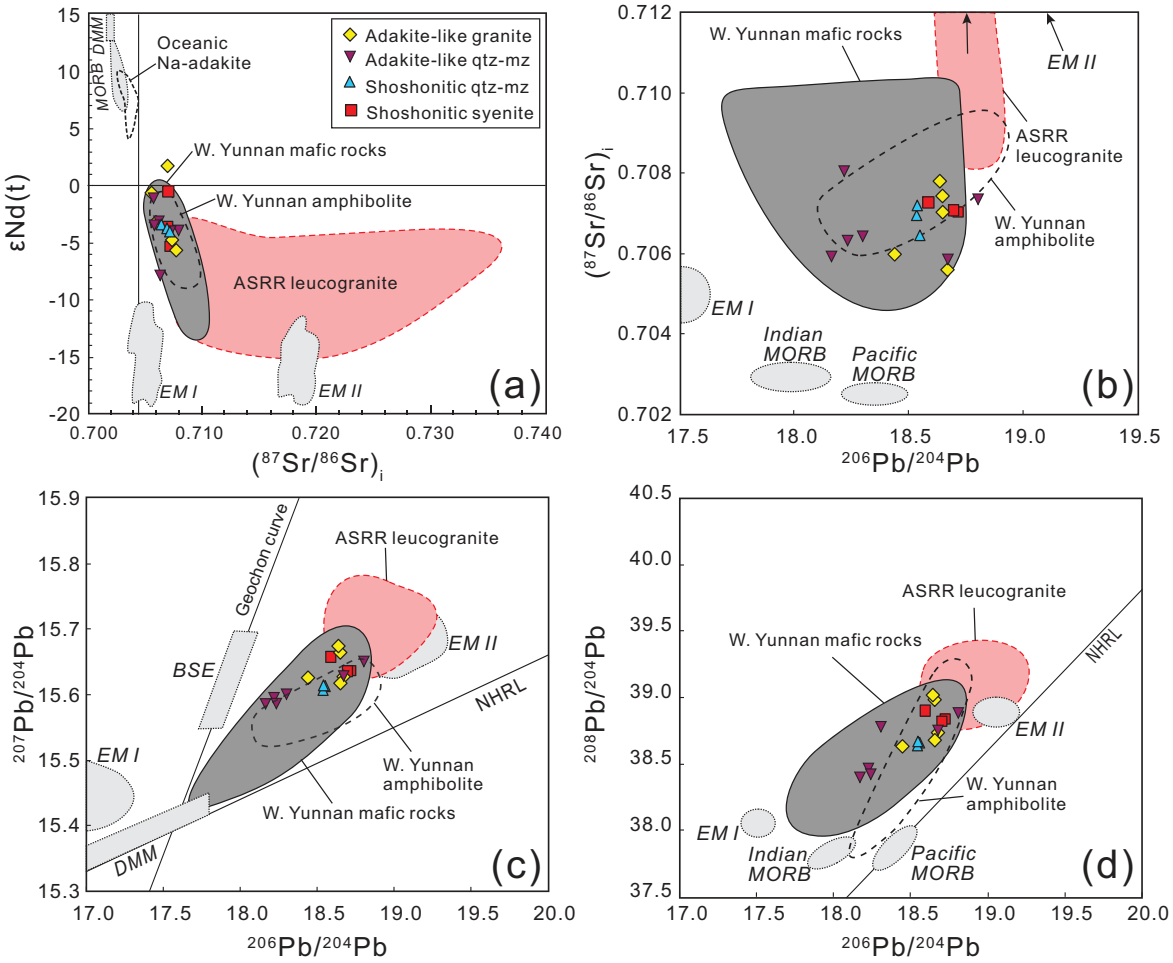

Fig. 11. Variation of $(^{87}Sr/^{86}Sr)_i$ vs $\varepsilon_{Nd}(t)$ (a), $^{206}Pb/^{204}Pb$ vs $(^{87}Sr/^{86}Sr)_i$ (b), $^{206}Pb/^{204}Pb$ vs $^{207}Pb/^{204}Pb$ (c) and $^{206}Pb/^{204}Pb$ vs $^{208}Pb/^{204}Pb$ (d) for the potassic felsic intrusions in western Yunnan (after Huang *et al.*, 2010). The field for oceanic sodic adakite attributed to melting of subducting oceanic crust is after Wang *et al.* (2006*b*). The field for western Yunnan potassic mafic rocks is from Xu *et al.* (2001*b*), Li *et al.* (2002), Guo *et al.* (2005) and Huang *et al.* (2010). The field for leucogranite within the Ailao Shan–Red River shear zone (ASRR) in western Yunnan is from Zhang & Schärer (1999). The field for western Yunnan amphibolite is from Deng *et al.* (1998) and Zhao *et al.* (2004). Northern Hemisphere Reference Line (NHRL) is from Hart (1984). Mantle source reservoirs BSE, MORB, DMM, EM I and EM II are from Zindler & Hart (1986). Indian MORB and Pacific MORB are after Guo *et al.* (2005). qtz-mz, quartz monzonite.

Tertiary magmatic zircons in the four samples have similar εHf, which mostly varies from near zero to +5·5 (Fig. 13). Samples SG-12 and BNC-3 have mantle-like magmatic zircon $\delta^{18}O$ values of 4·78–6·25‰, where the zircon $\delta^{18}O$ in equilibrium with mantle is 5·3 ± 0·6‰ (2σ, Valley *et al.*, 1998, 2005). Sample JC-7 has higher zircon $\delta^{18}O$ values ranging from 6·31 to 7·16‰ (Fig. 14; Table 3). The average zircon two-stage Hf mantle model ages (T_{DM2}) for the granites are 1·0–0·8 Ga (Table 3).

DISCUSSION

Petrogenesis of shoshonitic syenite and quartz monzonite

The SiO_2 contents of the shoshonitic syenites and quartz monzonites in western Yunnan are too high (61–65 wt %) to represent magmas derived by direct partial melting of the mantle, as the latter cannot yield melts more silicic than andesitic compositions with <57 wt % SiO_2 (Lloyd *et al.*, 1985; Baker *et al.*, 1995). Several lines of evidence suggest that the shoshonitic syenites and quartz monzonites evolved from shoshonitic mafic melts derived from metasomatized lithospheric mantle (Xu *et al.*, 2001*b*; Li *et al.*, 2002; Guo *et al.*, 2005; Huang *et al.*, 2010). The evidence includes the following: (1) the shoshonitic felsic and mafic suites in western Yunnan show close proximity and a coeval nature (Figs 1 and 2; Deng *et al.*, 1998; Lu *et al.*, 2012); (2) both the shoshonitic felsic and mafic suites are alkaline with continuous trends in Figs 5 and 6; (3) the shoshonitic mafic and felsic suites have the same coherent, parallel, REE and trace element patterns (Fig. 8); (4) the shoshonitic mafic and felsic suites plot together in Sr/Y vs

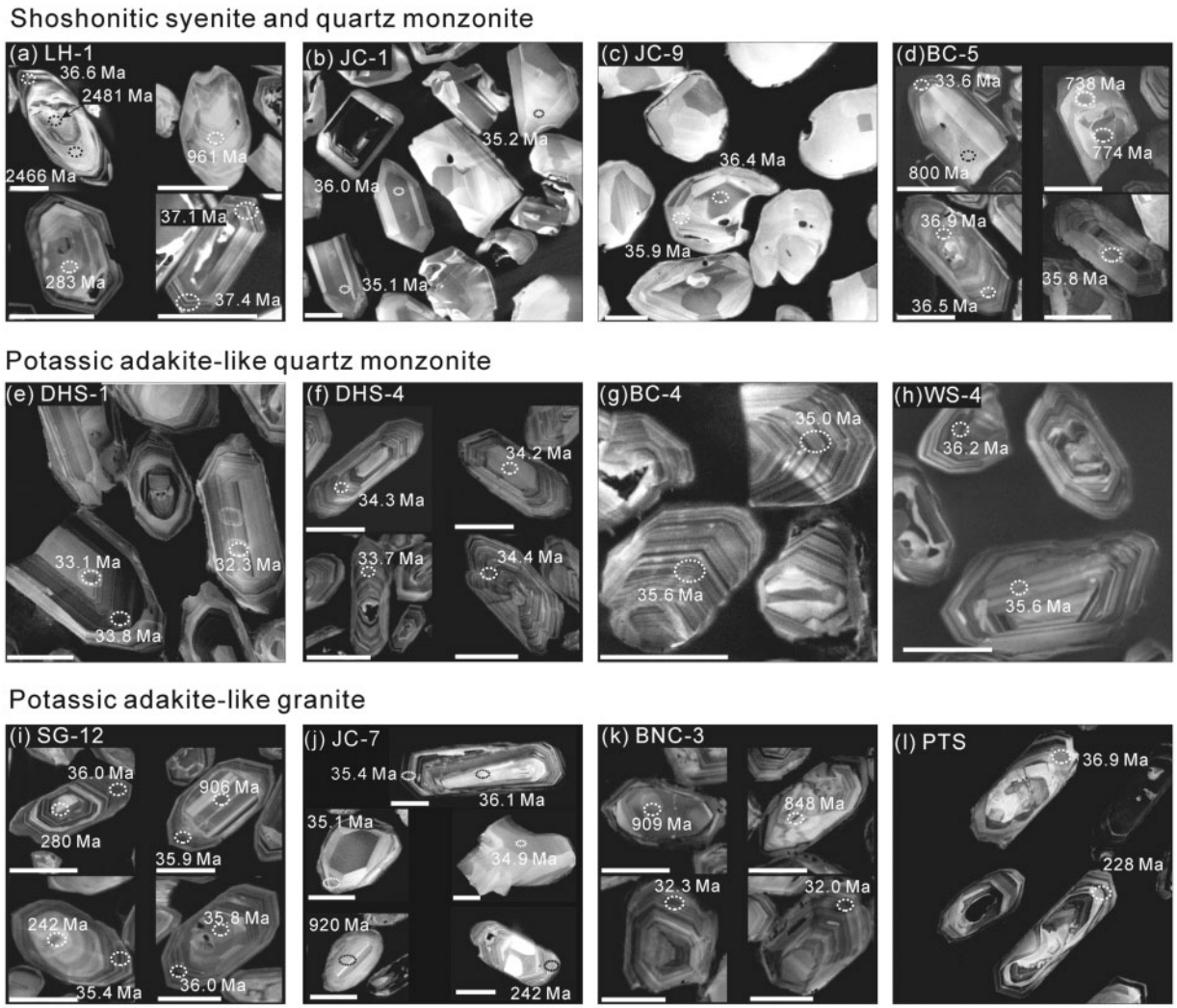

Fig. 12. Cathodoluminescence images of representative analyzed zircons from the potassic felsic intrusions in western Yunnan. The dashed ellipses indicate SHRIMP U–Pb pits and the number is the age of the corresponding spot (Lu *et al.*, 2012). The white scale bars represent 100 μm.

Y and La/Yb vs Yb co-ordinate space (Fig. 9); (5) the shoshonitic potassic felsic suites have Sr–Nd–Pb isotope compositions well within the range of the shoshonitic mafic magmas (Fig. 11).

Negative correlations of TiO_2, Fe_2O_3T, MgO, CaO, Ni and Cr with SiO_2 imply fractionation of olivine and clinopyroxene for both the shoshonitic syenites and quartz monzonites (Figs 6a, c, d, e and 7). In addition, plagioclase might have been another fractionated phase given the relatively low Eu/Eu* (0·65–0·78) values of these rocks (Table 1) coupled with negative correlations of Eu/Eu* and Sr with SiO_2 (not shown). Minor potassic feldspar fractionation may have also taken place for the shoshonitic syenites, as indicated by the negative correlation between K_2O and SiO_2 (Fig. 5b) and between Ba and SiO_2 (not shown). Both the shoshonitic syenites and quartz monzonites have similar and limited variations in La/Yb (18–23) and Dy/Yb (1·9–2·1) with increasing SiO_2, consistent with differentiation from a shoshonitic mafic melt by olivine, clinopyroxene and plagioclase (gabbroic) dominated fractional crystallization (Fig. 10). Amphibole and garnet were probably not involved in magmatic differentiation, because it is expected that garnet fractionation would be indicated by a significant increase in La/Yb and Dy/Yb ratios, whereas amphibole fractionation would be indicated by increased La/Yb and decreased Dy/Yb ratios. None of these trends are observed for the shoshonitic suites (Fig. 10; Davidson *et al.*, 2007; Macpherson, 2008).

Igneous zircons in high-temperature equilibrium with asthenospheric mantle should have average $\delta^{18}O$ of $5{\cdot}3 \pm 0{\cdot}6‰$ (2σ, Valley *et al.*, 1998, 2005). Significant deviations of zircon $\delta^{18}O$ from the mantle value are due to input of supracrustal materials that ultimately derived their higher $\delta^{18}O$ from low-temperature fluid–rock

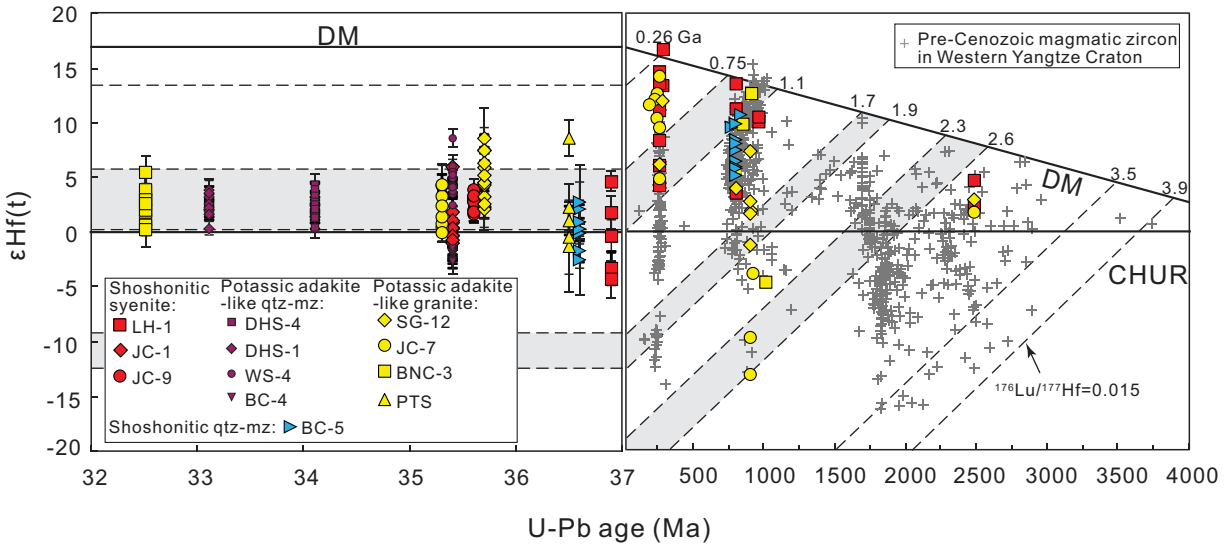

Fig. 13. Variation of initial εHf isotope values vs the U–Pb ages of the zircons studied. Data for Pre-Cenozoic magmatic zircons from western Yangtze Craton are from Huang *et al.* (2008, 2009), Xu *et al.* (2008), Sun *et al.* (2009) and Zhao *et al.* (2010). DM, Depleted Mantle; CHUR, Chondritic Uniform Reservoir. The grey fields represent episodes of major juvenile crustal growth in the Yangtze Craton (Sun *et al.*, 2009; Zhao *et al.*, 2010; Wang *et al.*, 2012). qtz-mz, quartz monzonite.

interaction on or near the Earth's surface (Valley *et al.*, 2005). It is generally accepted that zircons with $\delta^{18}O$ of less than 6·5‰ formed from melts that contained a minor to negligible supracrustal component, whereas zircon $\delta^{18}O$ values higher than 6·5‰ signify a significant component of supracrustal material (Cavosie *et al.*, 2005; Valley *et al.*, 2005; Hawkesworth & Kemp, 2006; Kemp *et al.*, 2006; Fu *et al.*, 2009; Hawkesworth *et al.*, 2010). For zircons with $\delta^{18}O > 6{\cdot}5$, it is important to distinguish high-$\delta^{18}O$ crustal materials recycled into the mantle source from melts or direct assimilation of a high-$\delta^{18}O$ supracrustal component in the crust.

The xenolith-free shoshonitic syenites have uniform zircon $\delta^{18}O$ values averaging $6{\cdot}58 \pm 0{\cdot}31$‰ (sample JC-9) and $6{\cdot}79 \pm 0{\cdot}35$‰ (sample JC-1), suggesting insignificant crustal contamination during magma emplacement (Fig. 15; Table 3), which is also indicated by the lack of zircon inheritance and relatively uniform zircon εHf ($-0{\cdot}9$ to $+3{\cdot}9$) values (Figs 12b, c and 13; Table 3). The crustal xenolith-bearing shoshonitic syenite (sample LH-1) has an average magmatic zircon $\delta^{18}O$ value of $6{\cdot}78 \pm 0{\cdot}24$‰, which is identical within error to that of its xenolith-free counterparts (Fig. 15). The xenolith-bearing shoshonitic quartz monzonite (sample BC-5) has an average magmatic zircon $\delta^{18}O$ value of $6{\cdot}11 \pm 0{\cdot}43$‰, which overlaps with those of the shoshonitic syenites (Fig. 15; Table 3). This suggests that the crustal xenoliths and the presence of inherited zircons had minimal effect on the oxygen isotope compositions; therefore supracrustal contamination appears to be negligible in the petrogenesis of shoshonitic syenites and quartz monzonites (Fig. 15).

The zircon $\delta^{18}O$ values of the shoshonitic syenites and quartz monzonites (6·11–6·79‰) are higher than that for the depleted mantle ($5{\cdot}3 \pm 0{\cdot}6$‰, 2σ; Valley *et al.*, 1998, 2005; Figs 14 and 15). The high $\delta^{18}O$ values for the shoshonitic syenites and quartz monzonites are inferred to be inherited from the parent shoshonitic mafic melt, rather than from the assimilation of a high-$\delta^{18}O$ supracrustal component (as discussed above). The potassic mafic rocks in western Yunnan were most probably derived from continental mantle lithosphere, metasomatized by subduction-related fluids and/or melts, which carry crustal elemental and isotopic signatures (Xu *et al.*, 2001*b*; Li *et al.*, 2002; Guo *et al.*, 2005; Huang *et al.*, 2010). It is likely that the elevated zircon $\delta^{18}O$ of the potassic suites is due to mantle metasomatism by subduction-derived fluids and/or melts (Eiler *et al.*, 1998); this was also inferred for potassic rocks in Central Italy (Gagnevin *et al.*, 2011). It has been also demonstrated that potassic magmatism in SW Tibet has whole-rock $\delta^{18}O$ values of 6·3–9·5‰, which is much higher than mantle values of 5·5–5·9‰ (Bindeman, 2008). These higher $\delta^{18}O$ values have been interpreted as being due to mantle metasomatism by melts and/or fluids derived from the subducting Indian continental crust (Zhao *et al.*, 2009).

Petrogenesis of potassic adakite-like suites

Origin of potassic adakite-like granite

The potassic adakite-like rocks in western Yunnan postdate the India–Asia continent–continent collision (Fig. 2). As a corollary, there is no geodynamic evidence for coeval oceanic subduction in western Yunnan that might have generated oceanic Na-adakite suites. Accordingly, given the

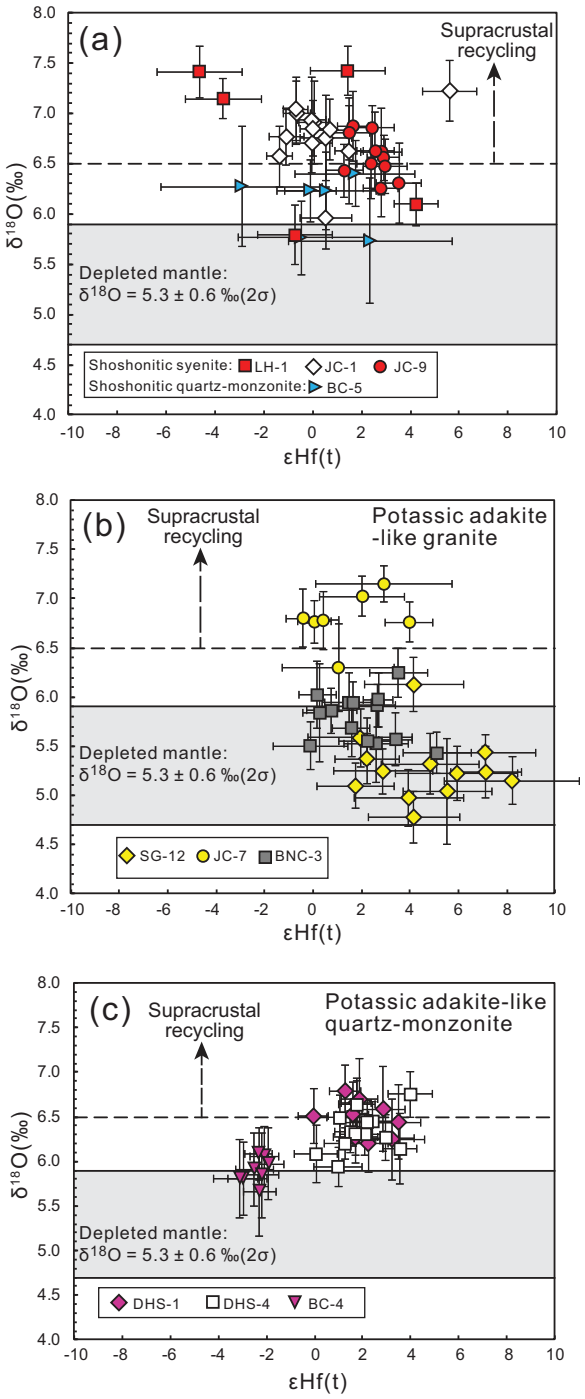

Fig. 14. Combined zircon Hf–O isotope diagram for the felsic intrusions in western Yunnan. The gray band represents the range of igneous zircons in high-temperature equilibrium with the Depleted Mantle ($\delta^{18}O = 5{\cdot}3 \pm 0{\cdot}6‰$, 2σ; Valley *et al.*, 1998, 2005). Zircons with $\delta^{18}O$ of less than 6·5‰ (dashed line) are interpreted to be formed from melts that contained a minor to negligible sedimentary component, whereas zircon $\delta^{18}O$ values higher than 6·5‰ indicate important supracrustal material contribution (Cavosie *et al.*, 2005; Valley *et al.*, 2005; Hawkesworth & Kemp, 2006).

post-collisional context it is unlikely that they were produced by partial melting of subducting oceanic crust. This suggestion is corroborated by the much lower $\varepsilon_{Nd}(t)$ and higher $(^{87}Sr/^{86}Sr)_i$ ratios for the western Yunnan potassic adakite-like rocks in comparison with the mid-ocean ridge basalt (MORB)-like isotopic signatures of Cenozoic oceanic Na-adakites (Fig. 11a). In addition, the western Yunnan potassic adakite-like granites have higher SiO_2 and lower MgO, Ni and Cr contents and lower Mg# values than delaminated lower crust-derived adakite-like rocks, suggesting that they were unlikely to have been derived by partial melting of delaminated lower crust (Fig. 7; Wang et al., 2006b).

The western Yunnan potassic adakite-like granites were most plausibly derived by partial melting of thickened K-rich mafic lower crust. This interpretation is supported by the following lines of evidence: (1) their major element compositions fit well within the fields of experimental melts of medium-K, high-K and shoshonitic amphibolites (Fig. 6; Rapp *et al.*, 1991; Rushmer, 1991, 1993; Sen & Dunn, 1994; Rapp & Watson, 1995; Sisson *et al.*, 2005; Xiong *et al.*, 2005; Xiao & Clemens, 2007); (2) their Mg#, and MgO, Ni and Cr contents are same as those of thick lower-crust derived adakite-like rocks and metabasaltic and eclogite experimental melts (Fig. 7; Wang *et al.*, 2006*b*); (3) their REE and trace element patterns are similar to those of the adakite-like granites in South Tibet, which are widely considered to be derived from thickened mafic lower crust (Fig. 8g and h; Chung *et al.*, 2003; Hou *et al.*, 2004; Guo *et al.*, 2007; Chen *et al.*, 2011).

There is a close match in the Sr and Nd isotope compositions of the potassic adakite-like granites and the western Yunnan amphibolite xenoliths hosted by the potassic felsic intrusions, indicating that amphibolites may be the primary source of the adakite-like granites (Fig. 11a). To test this hypothesis, batch melting modeling was conducted to simulate the Sr/Y vs Y and La/Yb vs Yb variations, following the methods of Haschke *et al.* (2002, 2010). The starting composition for the modeling is an amphibolite xenolith sampled at Liuhe in western Yunnan (sample LH14b, Wang *et al.*, 2003). The variations for the potassic adakite-like granites broadly follow the trends expected for partial melting with up to 30 wt % garnet in the restite (Fig. 9). On the Sr/Y vs Y diagram, some granite samples plot off the partial melting curves, which suggest that these samples might have a different source composition (Fig. 9a). The presence of garnet as a residual phase is consistent with the high La/Yb ratios (24–51), low HREE concentrations ($Yb_N < 6$), and fractionated HREE patterns ($Dy/Yb = 2{\cdot}1–3{\cdot}3$) of the adakite-like granites (Fig. 8g; Table 1). The distinctive positive correlation on La/Yb vs SiO_2 and Dy/Yb vs SiO_2 plots for the adakite-like granites also suggests that garnet was present in the residue during the partial melting process (Fig. 10; Davidson *et al.*, 2007; Macpherson, 2008).

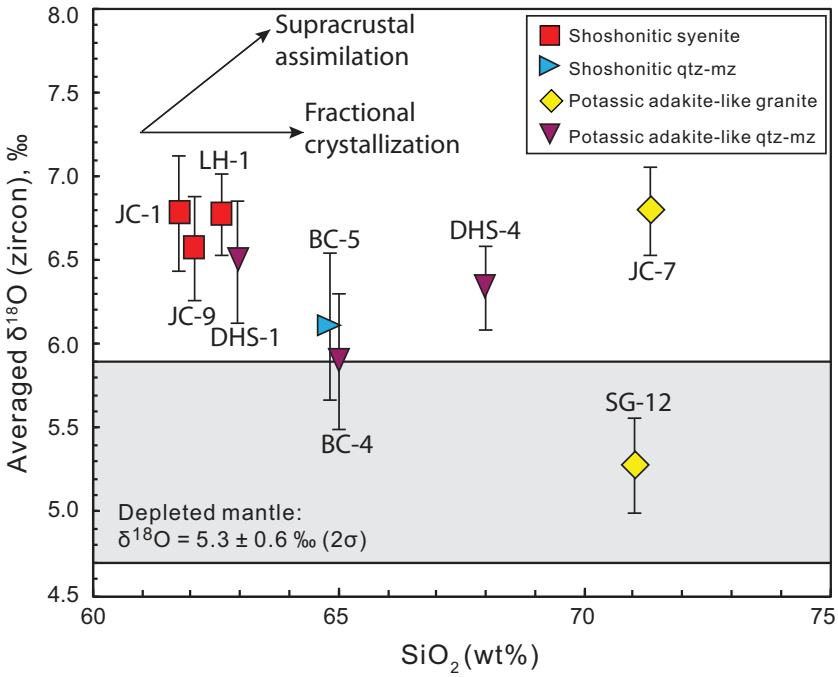

Fig. 15. Whole-rock SiO_2 (wt %) versus averaged Tertiary magmatic zircon $\delta^{18}O$ values. The sample number is shown next to the error bars (2σ). Supracrustal assimilation and fractional crystallization vectors are shown as arrows. Fractional crystallization in a closed system from a common parent will produce constant zircon $\delta^{18}O$ values from mafic to felsic melt; whereas open-system assimilation of supracrustal material will yield increasing zircon $\delta^{18}O$ values with increasing SiO_2 (Valley, 2003). qtz-mz, quartz monzonite.

The εHf value of the Tertiary magmatic zircons in the adakite-like granites mostly varies from near zero to +5·5 with corresponding mantle model ages of 0·8–1·1Ga, consistent with melting of Neoproterozoic mafic crust (Fig. 13). This interpretation is supported by the fact that the Neoproterozoic is the major episode for juvenile crustal growth in the Yangtze Craton (Sun *et al.*, 2009; Zhao *et al.*, 2010; Wang *et al.*, 2012).

The presence of inherited zircons with ages of 900–850 and 250 Ma indicates that there is an older crustal component involved in the genesis of the potassic adakite-like granites, either in the source or by AFC during magma emplacement (Figs 12i–l and 13). This older crustal component is unlikely to have been supracrustal material (such as metasedimentary rocks), given that most potassic adakite-like granites have mantle-like zircon $\delta^{18}O$ values (Fig. 14b). The age and εHf of the inherited zircons are similar to those of felsic intrusions in the Neoproterozoic and Late Permian sequences of the western Yangtze Craton (Huang *et al.*, 2008, 2009; Xu *et al.*, 2008). This observation implies that these older intrusions, as well as garnet amphibolite, were involved in the generation of the potassic adakite-like granites.

Origin of potassic adakite-like quartz monzonite

It is likely that the western Yunnan potassic adakite-like quartz monzonites are derived from partial melting of thickened mafic lower crust, through processes similar to those invoked for the potassic adakite-like granites. However, the difference is the involvement of hybridization with mafic magma as supported by petrographic and geochemical evidence. The evidence for this hybridization includes the following: (1) the presence of MMEs in the potassic adakite-like quartz monzonites suggests magma mingling and mixing (Waight *et al.*, 2000; Fig. 3d and e); (2) the major element compositions, REE and trace element characteristics of the potassic adakite-like quartz monzonites are transitional between the potassic adakite-like granites and the western Yunnan shoshonitic mafic magmas, consistent with two-component mixing (Figs 6 and 8e, f); (3) there is an inverse relationship between SiO_2 and both Mg# and MgO contents for the potassic adakite-like quartz monzonites. These trends are steeper than for the thick lower crust-derived adakite-like rocks and the metabasaltic experimental melts, which indicates a mafic magma input (Figs 6d and 7a, b; Guo *et al.*, 2007); (4) at the same SiO_2 contents, the potassic adakite-like quartz monzonites have higher Ni and Cr contents than the thick lower crust-derived adakite-like rocks, also suggesting input of a high Ni and Cr component such as a mafic melt (Fig. 7c and d).

To test the hybridization hypothesis, magma mixing modeling was conducted for the potassic adakite-like quartz monzonites to simulate the variations in Sr/Y vs Y

Table 4: Summary of Paleogene potassic magmatic suites and associated rocks in western Yunnan

Lithology:	Shoshonitic felsic suite		Potassic adakite-like felsic suite		Shoshonitic mafic suite		Crustal xenolith	ASRR
	Syenites	Quartz monzonites	Quartz monzonites	Granites	Mafic lava	Lamprophyre	Amphibolite	Leucogranite
Age (Ma)	36·9–35·4	36·6	35·4–33·1	36·8–32·5	36·6–35·1	36·2–33·4	–	32–22
Xenoliths	Garnet-bearing xenolith	Garnet-free xenolith	no	no	–	–	–	–
MMEs	yes	no	yes	no	–	–	–	–
SiO_2 (wt %)	61·1–63·6	62·3–64·8	62·3–68·9	68·8–71·5	44·5–60·0	43·5–54·8	40·0–51·6	73·4–74·5
MgO (wt %)	1·42–2·61	0·04–1·26	0·79–2·82	0·03–0·87	4·6–21·8	3·4–12·4	3·96–12·90	0·03–0·15
K_2O (wt %)	5·9–6·8	4·9–5·6	3·4–5·8	3·7–6·4	3·1–6·5	2·6–8·2	1·2–3·6	3·0–6·9
K_2O/Na_2O	1·3–1·7	1·1–1·3	0·7–1·4	0·7–1·9	1·3–3·9	0·8–5·0	0·6–1·3	0·8–2·5
A/CNK	0·67–0·75	0·80–0·84	0·83–1·05	0·91–1·06	0·28–0·70	0·44–0·82	0·56–0·78	1·02–1·16
Ni (ppm)	13·1–42·6	1·4–8·0	3·8–55·0	1·3–6·9	152–852	59·5–403	7·0–817·6	–
Cr (ppm)	34·3–113	3·2–35·3	7·6–113	2·0–27·7	348–1663	122–778	49·2–1815·2	–
Sr (ppm)	722–1604	1229–1450	813–1423	328–1272	311–1244	483–2104	200–1240	17–398
Yb (ppm)	1·5–3·2	1·8–2·5	0·7–1·6	0·4–0·9	1·3–2·4	1·3–3·6	1·2–6·1	0·6–1·7
Y (ppm)	15·7–34·8	18·0–27·2	8·9–18·6	4·3–12·1	14·7–29·6	14·9–50·3	12·6–63·1	–
Sr/Y	40–58	49–68	58–107	38–243	17–77	28–77	7–28	–
La/Yb	19–21	18–23	23–62	24–50	9–21	14–101	4–40	6–22
$(Ho/Yb)_n$	1·1–1·2	1·1–1·2	1·1–1·6	1·1–1·4	1·1–1·3	1·2–1·8	1·1–1·5	–
Eu/Eu*	0·65–0·72	0·75–0·78	0·60–0·91	0·64–0·87	0·67–1·04	0·76–0·89	0·62–1·14	0·27–0·58
$(^{87}Sr/^{86}Sr)_i$	0·7070–0·7073	0·7065–0·7072	0·7058–0·7080	0·7056–0·7078	0·7056–0·7094	0·7061–0·7095	0·7065–0·7093	0·7084–0·7354
$\varepsilon_{Nd}(t)$	−5·3 to −0·4	−3·4 to −4·0	−7·8 to −1·1	−5·6 to 1·8	−4·6 to −1	−10·5 to −0·9	−7·6 to −1·6	−13·4 to −3·3
Nd model age (Ma)	881–1272	1120–1169	937–1428	700–1303	1045–1380	945–1542	994–1323	1106–1931
$^{206}Pb/^{204}Pb$	18·589–18·720	18·540–18·554	18·168–18·808	18·440–18·673	18·556–18·695	18·159–18·708	18·136–18·847	18·609–19·216
$^{207}Pb/^{204}Pb$	15·637–15·659	15·608–15·615	15·587–15·651	15·619–15·675	15·609–15·630	15·568–15·702	15·558–15·632	15·636–15·765
$^{208}Pb/^{204}Pb$	38·821–38·899	38·639–38·670	38·390–38·874	38·633–39·018	38·603–38·817	38·755–39·362	37·839–39·205	38·837–39·331
Inherited/xenocrystic zircon	yes	yes	no	yes	–	–	–	yes
Zircon inheritance age (Ma)	260, 800–961, 2481	768–834	–	231–280, 800–1010, 2480	–	–	–	320–1860
εHf (zircon)	−4·2 to +4·7	−2·5 to +2·8	−2·7 to +8·6	−1·2 to +8·7	–	–	–	–
$\delta^{18}O‰$ (zircon)	5·79–7·43	5·74–6·41	5·67–6·80	4·78–7·16	–	–	–	–
Zircon Hf model age (Ma)	729–1383	938–1273	562–1284	562–1194	–	–	–	–
Reference	this study	this study	this study	this study	Xu *et al*. (2001*b*); Huang *et al*. (2010)	Guo *et al*. (2005); Lu *et al*. (2012)	Deng *et al*. (1998); Wang *et al*. (2003); Zhao *et al*. (2004)	Zhang & Schärer (1999)

—, no information or not measured; ASRR, Ailao Shan–Red River shear zone; MMEs, microgranular mafic enclaves.

and La/Yb vs Yb plots following the methods of Schwartz *et al.* (2011). The modeling shows that the trend of the potassic adakite-like quartz monzonites fits well with the magma mixing curves, which are distinct from the partial melting curves for the potassic adakite-like granites (Fig. 9).

The potassic adakite-like quartz monzonites have uniform mantle-like zircon $\delta^{18}O$ values, ruling out significant supracrustal contamination (Figs 14c and 15), in keeping with the lack of crustal xenoliths (Fig. 3d and e) and the absence of inherited zircons (Figs 12e–h and 13).

Implications for geodynamic processes

Table 4 summarizes the characteristics of the major magmatic suites and associated rocks in western Yunnan, including shoshonitic mafic suites, shoshonitic felsic, and potassic adakite-like felsic suites. Figure 16 illustrates the inferred tectonic evolution of the western Yangtze Craton (combining the results of previous studies and this contribution). Figure 17 illustrates in detail our proposed model for the origin of the various magmatic suites at *c.* 35 Ma in western Yunnan. The shoshonitic mafic suites in western Yunnan, consisting of mafic lavas and lamprophyres, are derived from metasomatized continental lithospheric mantle (CLM) (Table 4; Xu *et al.*, 2001*b*; Li *et al.*, 2002; Guo *et al.*, 2005; Huang *et al.*, 2010). The metasomatic domains within the CLM were probably formed by the double-vergent oceanic subduction beneath the northern and southern margins of Yangtze Craton at 1000–900 Ma as suggested by Li *et al.* (2008*b*) and Wang *et al.* (2009) (Fig. 16a). In the Late Triassic (220 Ma), the Simao Block accreted to the western Yangtze Craton along the westward subducting Jinsha suture. Since then, the western Yangtze Craton has occupied an intracontinental position (Fig. 16b; Yang, 1998; Wang *et al.*, 2000).

As discussed above, the shoshonitic suites require melting of metasomatized CLM, whereas the potassic adakite-like suites involve melting of a thickened potassic mafic lower crust with an older felsic component. The two magmatic suites are coeval and spatially closely related, in keeping with control by the same tectonic processes (Fig. 2).

The crustal thickness beneath western Yunnan is currently ~40–55 km, as indicated by data from seismic profiles (Li *et al.*, 2008*a*; Sun *et al.*, 2008), and was ~55 km in the Eocene, as estimated from studies of lower-crustal xenoliths hosted by the potassic felsic intrusions (Zhao *et al.*, 2003). Therefore, the crustal thickness has not changed significantly in western Yunnan since the Eocene, when it thickened to >50 km during the collision of the Indian and Asian plates (Fig. 16c).

Melting of thickened lower crust generally requires input of mantle heat (Thompson & Connolly, 1995; Petford *et al.*, 2000; Petford & Gallagher, 2001; Clemens, 2003; Zeng *et al.*, 2011). One plausible mechanism for

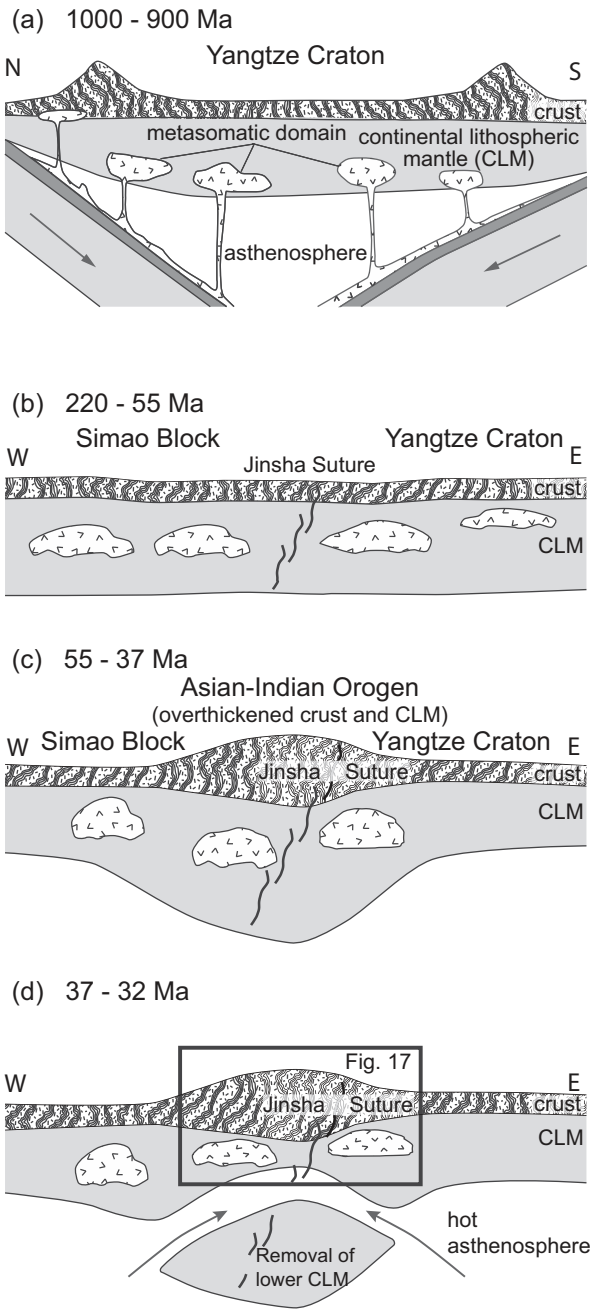

Fig. 16. Schematic illustration of the tectonic evolution of the western Yangtze Craton. (a) Double-vergent oceanic subduction from the northern and southern margins of the Yangtze Craton before 900 Ma produced metasomatic domains within the continental lithospheric mantle (CLM). (b) In the Late Triassic (*c.* 220 Ma), the Simao Block accreted to the western Yangtze Craton along the westward subducting Jinsha suture. Since then, the western Yangtze Craton has occupied an intracontinental position (Yang, 1998; Wang *et al.*, 2000). (c) Between *c.* 55 and 37 Ma, the continuing India–Asia continental collision may have preferentially overthickened the crust and CLM along the Jinsha suture. (d) The lower overthickened CLM was removed at *c.* 37–32 Ma along the Jinsha suture, causing upwelling of hot asthenosphere. (a) is a north–south section whereas (b)–(d) are west–east sections.

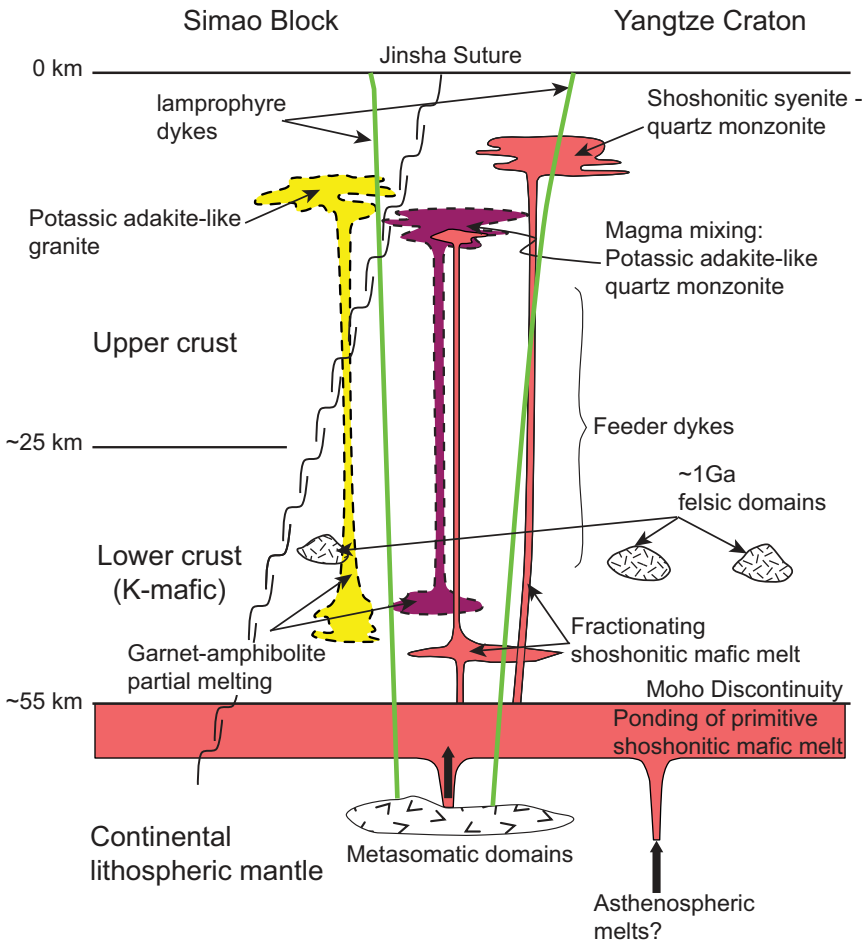

Fig. 17. Schematic crustal section during the formation of the post-collisional potassic magmatic rocks in western Yunnan (modified from Annen *et al.*, 2006; Guo *et al.*, 2007). The primitive shoshonitic mafic melt from the metasomatic domains within the continental lithospheric mantle underplated beneath the thickened crust or intruded directly as lamprophyre dykes. Shoshonitic syenites and quartz monzonites are mainly due to fractional crystallization of shoshonitic mafic melts. In contrast, potassic adakite-like granites are mainly potassic mafic lower-crustal melts with involvement of older felsic domains (*c.* 1 Ga) in keeping with zircon inheritance. Potassic adakite-like quartz monzonites are due to varying degrees of mixing between lower-crustal melts and shoshonitic mafic melts, probably in the upper crust. The thickness of the crust beneath western Yunnan (~55 km) is from Zhao *et al.* (2003).

inducing both lower-crustal melting and CLM melting is asthenosphere upwelling induced by the thinning of the lithospheric mantle (Thompson & Connolly, 1995; Clemens, 2003). Therefore, we propose that the shoshonitic and potassic adakite-like magmatism was in response to the removal of the lower overthickened CLM beneath the western Yangtze Craton, which took place at 37–32 Ma following the Indian–Asian continent–continent collision (Fig. 16d).

Using geophysical data, Liu *et al.* (2000) and Lei *et al.* (2009) suggested that there is an ~300 km wide mantle diapir derived from ~450 km depth beneath western Yunnan. This may support the conclusion that the lower CLM was removed and replaced by upwelling asthenosphere. In this process, upwelling hot asthenosphere displaces cooler lower CLM, causing asthenospheric decompression and advection of heat. This can lead to the production of the shoshonitic mafic magmas observed in western Yunnan through the melting of the residual metasomatized CLM. In this model, underplating of CLM- or asthenosphere-derived melts at the Moho density filter, and intrusion of mantle-derived hot mafic magmas into an already thickened continental crust, induced dehydration melting of potassic-rich mafic and minor felsic components in the lower crust. This resulted in the production of the potassic adakite-like granitic melts containing inherited zircons (Table 4; Fig. 17). Fractional crystallization of the shoshonitic mafic magmas en route to shallow crustal levels generated the shoshonitic syenites and quartz monzonites. Extensive interaction between the mafic magmas and the lower-crustal adakite-like melts through mixing produced the potassic adakite-like quartz monzonites (Fig. 17).

The 2000 km long Eocene potassic magmatic belt across the Qiangtang Terrane and Yangtze Craton is coincident with the Late Triassic translithospheric Jinsha suture (Fig. 1). This spatial distribution of the potassic magmatic suites suggests that the translithospheric structure may have been the focus of lithospheric overthickening during development of the Asian–Indian orogen since 55 Ma, and is now the upper-crustal expression of the locus of removal of the CLM. These lithospheric boundaries and structures may have provided first-order control on the localization of the post-collisional intracontinental magmatism (Begg *et al.*, 2009).

CONCLUSIONS

(1) Spatially related, coeval potassic adakite-like and shoshonitic felsic intrusions occur in the western Yunnan province of SW China, recognized on the basis of field relationships and their major and trace element compositions. The shoshonitic syenites and quartz monzonites are characterized by high K_2O contents (4·9–6·8 wt %) and K_2O/Na_2O ratios (1·1–1·7), enrichment in LREE and LILE, and depletion in Nb, Ta, Ti and P. The potassic adakite-like granites and quartz monzonites are both characterized by high Sr (328–1423 ppm), Sr/Y (38–243) and La/Yb (23–62) values, and low Y and Yb contents.

(2) The shoshonitic syenites and quartz monzonites have the same Sr–Nd–Pb isotope compositions as the shoshonitic mafic magma suite. They define linear trends on Harker variation diagrams, and have similar REE and trace-element patterns to the shoshonitic mafic magmas, suggesting a comagmatic origin. These observations suggest that the shoshonitic syenites and quartz monzonites originated by fractional crystallization of shoshonitic mafic melts derived from metasomatized lithospheric mantle with varying degrees of olivine, clinopyroxene and feldspar fractionation. The shoshonitic syenites and quartz monzonites have higher zircon $\delta^{18}O$ values (6·26–7·05‰) than the mantle, which suggests some ^{18}O enrichment from earlier subduction-related metasomatic enrichment of the CLM source.

(3) The potassic adakite-like granites have Sr–Nd–Pb isotopic compositions that overlap those of lower-crustal amphibolites. They have low Mg# and MgO, Ni and Cr contents, abundant inherited zircons, juvenile zircon εHf (0–5·5) and mantle-like $\delta^{18}O$ (4·78–6·25‰) values. The granites were probably derived from partial melting of a thickened, potassic, mafic lower crust with minor input from an older igneous felsic component.

(4) The potassic adakite-like quartz monzonites contain abundant mafic microgranular enclaves (MMEs), and have transitional major and trace element characteristics between the adakite-like granites and the shoshonitic mafic magmas. The quartz monzonites generally have higher Mg# and MgO, Ni and Cr contents than the thick lower crust derived adakite-like rocks. They have no inherited zircons and display uniform zircon εHf and $\delta^{18}O$ values. It is suggested that they were derived by variable degrees of mixing between lower-crustal melts and shoshonitic mafic magmas.

(5) Collectively, the geochemical, Sr–Nd–Pb isotope and zircon Hf–O isotope signatures are consistent with both the shoshonitic and potassic adakite-like suites being associated with removal of the lower CLM and upwelling of asthenosphere in western Yunnan, which induced partial melting of the residual metasomatized lithospheric mantle as well as the thickened potassic mafic lower crust.

ACKNOWLEDGEMENTS

We thank Drs Shuxian Wang and Lizhen Li for major, trace element, and Pb isotopic analyses. Dr Zhiming Yang and Chuandong Xue are appreciated for fieldwork assistance. Robert Loucks, Zhaohua Luo and Simon Wilde are thanked for valuable discussions. The paper benefited greatly from critical reviews by Tod Waight, Derek Wyman, Jeremy Richards, David Cooke, Colin Macpherson and an anonymous reviewer. R. Kerrich acknowledges a Natural Science and Engineering Council of Canada Discovery Grant, and George McLeod endowment to the Department of Geological Sciences. The Hf analytical data were obtained using instrumentation funded by DEST Systemic Infrastructure Grants, ARC LIEF, NCRIS, industry partners and Macquarie University. The authors acknowledge the facilities, and the scientific and technical assistance of the Australian Microscopy & Microanalysis Research Facility at the Centre for Microscopy, Characterisation & Analysis, The University of Western Australia, a facility funded by the University, State and Commonwealth Governments. This is contribution 162 from the ARC Centre of Excellence for Core to Crust Fluid Systems (http://www.CCFS.mq.edu.au), TIGeR (The Institute for Geoscience Research) publication 452 and an IGCP/SIDA-600 contribution.

FUNDING

This study was funded by the Ministry of Science and Technology of China (973 project: 2011CB403100), IGCP/SIDA-600, the National Natural Science Foundation of China (40730419; 40425014), the Ministry of Land and Resources of China (201011011), Centre for Exploration Targeting, The Society of Economic Geologists Student Research Grant, and the Australian Microscopy and

Microanalysis Research Facility (AMMRF) TAP Grant, which are gratefully acknowledged.

REFERENCES

Annen, C., Blundy, J. D. & Sparks, R. S. J. (2006). The genesis of intermediate and silicic magmas in deep crustal hot zones. *Journal of Petrology* **47**, 505–539.

Atherton, M. P. & Petford, N. (1993). Generation of sodium-rich magmas from newly underplated basaltic crust. *Nature* **362**, 144–146.

Baertschi, P. (1976). Absolute ^{18}O content of Standard Mean Ocean Water. *Earth and Planetary Science Letters* **31**, 341–344.

Baker, M. B., Hirschmann, M. M., Ghiorso, M. S. & Stolper, E. M. (1995). Compositions of near-solidus peridotite melts from experiments and thermodynamic calculations. *Nature* **375**, 308–311.

Begg, G. C., Griffin, W. L., Natapov, L. M., O'Reilly, S. P., Grand, S. P., O'Neill, C. J., Hronsky, Y., Djomani, P., Swain, C. S., Deen, T. & Bowden, P. (2009). The lithospheric architecture of Africa: seismic tomography, mantle petrology, and tectonic evolution. *Geosphere* **5**, 23–50.

Bindeman, I. (2008). Oxygen isotopes in mantle and crustal magmas as revealed by single crystal analysis. In: Putirka, K. D. & Tepley, F. J., III (eds) *Minerals, Inclusions and Volcanic Processes. Mineralogical Society of America and Geochemical Society, Reviews in Mineralogy and Geochemistry* **69**, 445–478.

Black, L. P., Kamo, S. L., Allen, C. M., Davis, D. W., Aleinikoff, J. N., Valley, J. W., Mundil, R., Campbell, I. H., Korsch, R. J., Williams, I. S. & Foudoulis, C. (2004). Improved $^{206}Pb/^{238}U$ microprobe geochronology by the monitoring of a trace-element-related matrix effect; SHRIMP, ID-TIMS, ELA-ICP-MS and oxygen isotope documentation for a series of zircon standards. *Chemical Geology* **205**, 115–140.

Bouvier, A., Vervoort, J. D. & Patchett, P. J. (2008). The Lu–Hf and Sm–Nd isotopic composition of CHUR: Constraints from unequilibrated chondrites and implications for the bulk composition of terrestrial planets. *Earth and Planetary Science Letters* **273**, 48–57.

Capitanio, F. A., Morra, G., Goes, S., Weinberg, R. F. & Moresi, L. (2010). India–Asia convergence driven by the subduction of the Greater Indian continent. *Nature Geoscience* **3**, 136–139.

Castillo, P. R. (2012). Adakite petrogenesis. *Lithos* **134–135**, 304–316.

Castillo, P. R., Janney, P. E. & Solidum, R. U. (1999). Petrology and geochemistry of Camiguin Island, southern Philippines: insights to the source of adakites and other lavas in a complex arc setting. *Contributions to Mineralogy and Petrology* **134**, 33–51.

Cavosie, A. J., Valley, J. W. & Wilde, S. A. Edinburgh Ion Microprobe Facility (2005). Magmatic $\delta^{18}O$ in 4400–3900 Ma detrital zircons: A record of the alteration and recycling of crust in the Early Archean. *Earth and Planetary Science Letters* **235**, 663–681.

Chen, J. L., Xu, J. F., Zhao, W. X., Dong, Y. H., Wang, B. D. & Kang, Z. Q. (2011). Geochemical variations in Miocene adakitic rocks from the western and eastern Lhasa terrane: Implications for lower crustal flow beneath the Southern Tibetan Plateau. *Lithos* **125**, 928–939.

Chung, S. L. & Jahn, B. M. (1995). Plume–lithosphere interaction in generation of the Emeishan flood basalts at the Permian–Triassic boundary. *Geology* **23**, 889–892.

Chung, S. L., Lee, T. Y., Lo, C. H., Wang, P. L., Chen, C. Y., Yem, N. T., Hoa, T. & Genyao, W. (1997). Intraplate extension prior to continental extrusion along the Ailao Shan–Red River shear zone. *Geology* **25**, 311–314.

Chung, S. L., Lo, C. H., Lee, T. Y., Zhang, Y. Q., Xie, Y. W., Li, X. H., Wang, K. L. & Wang, P. L. (1998). Diachronous uplift of the Tibetan plateau starting 40 Myr ago. *Nature* **394**, 769–773.

Chung, S. L., Liu, D. Y., Ji, J. Q., Chu, M. F., Lee, H. Y., Wen, D. R., Lo, C. H., Lee, T. Y., Qian, Q. & Zhang, Q. (2003). Adakites from continental collision zones: Melting of thickened lower crust beneath southern Tibet. *Geology* **31**, 1021–1024.

Chung, S. L., Chu, M. F., Zhang, Y. Q., Xie, Y. W., Lo, C. H., Lee, T. Y., Lan, C. Y., Li, X. H., Zhang, Q. & Wang, Y. Z. (2005). Tibetan tectonic evolution inferred from spatial and temporal variations in post-collisional magmatism. *Earth-Science Reviews* **68**, 173–196.

Chung, S. L., Searle, M. P. & Yeh, M. W. (2008). The age of potassic alkaline igneous rocks along the Ailao Shan–Red River shear zone: Implications for the onset age of left-lateral shearing: A Discussion. *Journal of Geology* **116**, 201–204.

Chung, S. L., Chu, M. F., Ji, J. Q., O'Reilly, S. Y., Pearson, N. J., Liu, D. Y., Lee, T. Y. & Lo, C. H. (2009). The nature and timing of crustal thickening in Southern Tibet: Geochemical and zircon Hf isotopic constraints from postcollisional adakites. *Tectonophysics* **477**, 36–48.

Clemens, J. D. (2003). S-type granitic magmas—petrogenetic issues, models and evidence. *Earth-Science Reviews* **61**, 1–18.

Cousens, B. L., Aspler, L. B., Chiarenzelli, J. R., Donaldson, J. A., Sandeman, H., Peterson, T. D. & Lecheminant, A. N. (2001). Enriched Archean lithospheric mantle beneath western Churchill Province tapped during Paleoproterozoic orogenesis. *Geology* **29**, 827–830.

Davidson, J., Turner, S., Handley, H., Macpherson, C. & Dosseto, A. (2007). Amphibole 'sponge' in arc crust? *Geology* **35**, 787–790.

DeBievre, P. & Taylor, P. D. P. (1993). Table of the isotopic composition of the elements. *International Journal of Mass Spectrometry and Ion Processes* **123**, 149.

Defant, M. J. & Drummond, M. S. (1990). Derivation of some modern arc magmas by melting of young subducted lithosphere. *Nature* **347**, 662–665.

Deng, W. M., Huang, X. & Zhong, D. L. (1998). Petrological characteristics and genesis of Cenozoic alkali-rich porphyry in West Yunnan, China. *Scientia Geologica Sinica* **33**, 412–425 (in Chinese with English abstract).

DePaolo, D. J. (1988). *Neodymium Isotope Geochemistry: an Introduction.* New York: Springer, 230 p.

Eiler, J. M., McInnes, B., Valley, J. W., Graham, C. M. & Stolper, E. M. (1998). Oxygen isotope evidence for slab-derived fluids in the sub-arc mantle. *Nature* **393**, 777–781.

Ernst, R. E., Wingate, M.T. D., Buchan, K. L. & Li, Z. X. (2008). Global record of 1600–700 Ma Large Igneous Provinces (LIPs): Implications for the reconstruction of the proposed Nuna (Columbia) and Rodinia supercontinents. *Precambrian Research* **160**, 159–178.

Foley, S., Tiepolo, M. & Vannucci, R. (2002). Growth of early continental crust controlled by melting of amphibolite in subduction zones. *Nature* **417**, 837–840.

Fu, B., Mernagh, T. P., Kita, N. T., Kemp, A. I. S. & Valley, J. W. (2009). Distinguishing magmatic zircon from hydrothermal zircon: A case study from the Gidginbung high-sulphidation Au–Ag–(Cu) deposit, SE Australia. *Chemical Geology* **259**, 131–142.

Gagnevin, D., Daly, J. S., Horstwood, M.S. A. & Whitehouse, M. J. (2011). *In-situ* zircon U–Pb, oxygen and hafnium isotopic evidence for magma mixing and mantle metasomatism in the Tuscan Magmatic Province, Italy. *Earth and Planetary Science Letters* **305**, 45–56.

Gill, J. (1981). *Orogenic Andesites and Plate Tectonics.* New York: Springer, 358 p.

Goldstein, S. L., O'Nions, R. K. & Hamilton, P. J. (1984). A Sm–Nd isotopic study of atmospheric dusts and particulates from major river systems. *Earth and Planetary Science Letters* **70**, 221–236.

Griffin, W. L., Pearson, N. J., Belousova, E., Jackson, S. E., Achterbergh, E., O'Reilly, S. Y. & Shee, S. R. (2000). The Hf isotope composition of cratonic mantle: LAM-MC-ICPMS analysis of zircon megacrysts in kimberlites. *Geochimica et Cosmochimica Acta* **64**, 133–147.

Griffin, W. L., Wang, X., Jackson, S. E., Pearson, N. J., O'Reilly, S. Y., Xu, X. S. & Zhou, X. M. (2002). Zircon chemistry and magma mixing, SE China: *in-situ* analysis of Hf isotopes, Tonglu and Pingtan igneous complexes. *Lithos* **61**, 237–269.

Guo, Z. F., Hertogen, J., Liu, J. Q., Pasteels, P., Boven, A., Punzalan, L., He, H. & Luo, X. (2005). Potassic magmatism in Western Sichuan and Yunnan Provinces, SE Tibet, China: Petrological and geochemical constraints on petrogenesis. *Journal of Petrology* **46**, 33–78.

Guo, Z. F., Wilson, M. & Liu, J. Q. (2007). Post-collisional adakites in south Tibet: Products of partial melting of subduction-modified lower crust. *Lithos* **96**, 205–224.

Hart, S. R. (1984). A large-scale isotope anomaly in the southern hemisphere mantle. *Nature* **309**, 753–757.

Haschke, M., Siebel, W., Gunther, A. & Scheuber, E. (2002). Repeated crustal thickening and recycling during the Andean orogeny in north Chile (21–26°S). *Journal of Geophysical Research* **107**, 1–18.

Haschke, M., Ahmadian, J., Murata, M. & McDonald, I. (2010). Copper mineralization prevented by arc-root delamination during Alpine–Himalayan collision in central Iran. *Economic Geology* **105**, 855–865.

Hawkesworth, C. J. & Kemp, A. I. S. (2006). Using hafnium and oxygen isotopes in zircons to unravel the record of crustal evolution. *Chemical Geology* **226**, 144–162.

Hawkesworth, C. J., Dhuime, B., Pietranik, A. B., Cawood, P. A., Kemp, A. I. S. & Storey, C. D. (2010). The generation and evolution of the continental crust. *Journal of the Geological Society, London* **167**, 229–248.

He, H. L., Li, B., Han, L. R., Sun, D. Z., Wang, S. X. & Li, S. (2002). Evaluation of determining 47 elements in geological samples by pressurized acid digestion–ICPMS. *Chinese Journal of Analysis Laboratory* **21**, 8–12 (in Chinese with English abstract).

He, S. X., Zhu, X. K., Yang, C. & Tang, S. H. (2005). High-precision analysis of Pb isotope ratios using MC-ICPMS. *Acta Geoscientica Sinica* **26**, 19–22 (in Chinese with English abstract).

He, S. X., Tang, S. H., Zhu, X. K. & Wang, J. H. (2007). Precise measurement of Nd isotopic ratios by means of multi-collector magnetic sector inductively coupled plasma mass spectrometry. *Acta Geoscientica Sinica* **28**, 405–410 (in Chinese with English abstract).

Hou, Z. Q., Gao, Y. F., Qu, X. M., Rui, Z. Y. & Mo, X. X. (2004). Origin of adakitic intrusives generated during mid-Miocene east–west extension in southern Tibet. *Earth and Planetary Science Letters* **220**, 139–155.

Hou, Z. Q., Zheng, Y. C., Zeng, L. S., Gao, L. E., Huang, K. X., Li, W., Li, Q. Y., Fu, Q., Liang, W. & Sun, Q. Z. (2012). Eocene–Oligocene granitoids in southern Tibet: Constraints on crustal anatexis and tectonic evolution of the Himalayan orogen. *Earth and Planetary Science Letters* **349–350**, 38–52.

Houseman, G. A. & Molnar, P. (1997). Gravitational (Rayleigh–Taylor) instability of a layer with non-linear viscosity and convective thinning of continental lithosphere. *Geophysical Journal International* **128**, 125–150.

Huang, X. L., Xu, Y. G., Li, X. H., Li, W. X., Lan, J. B., Zhang, H. H., Liu, Y. S., Wang, Y. B., Li, H. Y., Luo, Z. Y. & Yang, Q. J. (2008). Petrogenesis and tectonic implications of Neoproterozoic, highly fractionated A-type granites from Mianning, South China. *Precambrian Research* **165**, 190–204.

Huang, X. L., Xu, Y. G., Lan, J. B., Yang, Q. J. & Luo, Z. Y. (2009). Neoproterozoic adakitic rocks from Mopanshan in the western Yangtze Craton: Partial melts of a thickened lower crust. *Lithos* **112**, 367–381.

Huang, X. L., Niu, Y., Xu, Y. G., Chen, L. L. & Yang, Q. J. (2010). Mineralogical and geochemical constraints on the petrogenesis of post-collisional potassic and ultrapotassic rocks from western Yunnan, SW China. *Journal of Petrology* **51**, 1617–1654.

Irvine, T. N. & Baragar, W.R. A. (1971). A guide to the chemical classification of the common volcanic rocks. *Canadian Journal of Earth Sciences* **8**, 523–548.

Jacobsen, S. B. & Wasserburg, G. J. (1980). Sm–Nd isotopic evolution of chondrites. *Earth and Planetary Science Letters* **50**, 139–155.

Kay, R. W. & Kay, S. M. (1993). Delamination and delamination magmatism. *Tectonophysics* **219**, 177–189.

Kemp, A. I. S. & Hawkesworth, C. J. (2003). Granitic perspectives on the generation and secular evolution of the continental crust. In: Rudnick, R. L. (ed.) *The Crust. Treatise on Geochemistry, Vol. 3.* Amsterdam: Elsevier, pp. 349–410.

Kemp, A. I. S., Hawkesworth, C. J., Paterson, B. A. & Kinny, P. D. (2006). Episodic growth of the Gondwana supercontinent from hafnium and oxygen isotopes in zircon. *Nature* **439**, 580–583.

Kepezhinskas, P., Defant, M. J. & Drummond, M. S. (1996). Progressive enrichment of island arc mantle by melt–peridotite interaction inferred from Kamchatka xenoliths. *Geochimica et Cosmochimica Acta* **60**, 1217–1229.

Kind, R. & Yuan, X. H. (2010). Seismic images of the biggest crash on Earth. *Science* **329**, 1479–1480.

Lee, T. Y. & Lawver, L. A. (1995). Cenozoic plate reconstruction of Southeast Asia. *Tectonophysics* **251**, 85–138.

Lei, J. S., Zhao, D. P. & Su, Y. J. (2009). Insight into the origin of the Tengchong intraplate volcano and seismotectonics in southwest China from local and teleseismic data. *Journal of Geophysical Research* **114**, B05302.

Leloup, P. H., Lacassin, R., Tapponnier, P., Schärer, U., Zhong, D. L., Liu, X. H., Zhang, L. S., Ji, S. C. & Trinh, P. T. (1995). The Ailao Shan–Red River shear zone (Yunnan, China), Tertiary transform boundary of Indochina. *Tectonophysics* **251**, 3–84.

Leslie, R. A. J., Danyushevsky, L. V., Crawford, A. J. & Verbeeten, A. C. (2009). Primitive shoshonites from Fiji: Geochemistry and source components. *Geochemistry, Geophysics and Geosystems* **10**, Q07001, doi:10.1029/2008GC002326.

Li, X. H., Zhou, H. W., Chung, S. L., Lo, C. H., Wei, G. J., Liu, Y. & Lee, C. Y. (2002). Geochemical and Sr–Nd isotopic characteristics of late Paleogene ultrapotassic magmatism in Southeastern Tibet. *International Geology Review* **44**, 559–574.

Li, Y. H., Wu, Q. J., Zhang, R. Q., Tian, X. B. & Zeng, R. S. (2008*a*). The crust and upper mantle structure beneath Yunnan from joint inversion of receiver functions and Rayleigh wave dispersion data. *Physics of the Earth and Planetary Interiors* **170**, 134–146.

Li, Z. X. (1998). Tectonic history of the major East Asian lithospheric blocks since the Mid-Proterozoic—a synthesis. In: Flower, M. F. J., Chung, S.-L., Lo, C.-H. & Lee, T.-Y. (eds) *Mantle Dynamics and Plate Interactions in East Asia. Geodynamics Series, American Geophysical Union* **27**, 221–243.

Li, Z. X., Bogdanova, S. V., Collins, A. S., Davidson, A., De Waele, B., Ernst, R. E., Fitzsimons, I. C. W., Fuck, R. A., Gladkochub, D. P., Jacobs, J., Karlstromk, K. E., Lu, S., Natapovm, L. M., Pease, V., Pisarevsky, S. A., Thrane, K. & Vernikovsky, V. (2008*b*). Assembly,

configuration, and break-up history of Rodinia: A synthesis. *Precambrian Research* **160**, 179–210.

Liang, H. Y., Campbell, I. H., Allen, C. M., Sun, W. D., Yu, H. X., Xie, Y. W. & Zhang, Y. Q. (2007). The age of the potassic alkaline igneous rocks along the Ailao Shan–Red River shear zone: Implications for the onset age of left-lateral shearing. *Journal of Geology* **115**, 231–242.

Liu, C. Z., Wu, F. Y., Chung, S. L. & Zhao, Z. D. (2011). Fragments of hot and metasomatized mantle lithosphere in Middle Miocene ultrapotassic lavas, southern Tibet. *Geology* **39**, 923–926.

Liu, F. T., Liu, J. H., Zhong, D. L., He, J. K. & You, Q. Y. (2000). The subducted slab of Yangtze continental block beneath the Tethyan orogen in western Yunnan. *Chinese Science Bulletin* **45**, 466–472.

Lloyd, F. E., Arima, M. & Edgar, A. D. (1985). Partial melting of a phlogopite-clinopyroxenite nodule from south-west Uganda: an experimental study bearing on the origin of highly potassic continental rift volcanics. *Contributions to Mineralogy and Petrology* **91**, 321–329.

Lu, Y. J., Kerrich, R., Cawood, P. A., McCuaig, T. C., Hart, C. J. R., Li, Z. X., Hou, Z.-Q. & Bagas, L. (2012). Zircon SHRIMP U–Pb geochronology of potassic felsic intrusions in western Yunnan, SW China: Constraints on the relationship of magmatism to the Jinsha suture. *Gondwana Research* **22**, 737–747.

Lugmair, G. W. & Marti, K. (1978). Lunar initial $^{143}Nd/^{144}Nd$: differential evolution of the lunar crust and mantle. *Earth and Planetary Science Letters* **39**, 349–357.

Macpherson, C. G. (2008). Lithosphere erosion and crustal growth in subduction zones: Insights from initiation of the nascent East Philippine Arc. *Geology* **36**, 311–314.

Macpherson, C. G., Dreher, S. T. & Thirlwall, M. F. (2006). Adakites without slab melting: High pressure differentiation of island arc magma, Mindanao, the Philippines. *Earth and Planetary Science Letters* **243**, 581–593.

McCulloch, M. T. & Black, L. P. (1984). Sm–Nd isotope systematics of Enderby Land granulites and evidence for the redistribution of Sm and Nd during metamorphism. *Earth and Planetary Science Letters* **71**, 46–58.

Metcalfe, I. (2006). Palaeozoic and Mesozoic tectonic evolution and palaeogeography of East Asian crustal fragments: The Korean Peninsula in context. *Gondwana Research* **9**, 24–46.

Middlemost, E. A. K. (1994). Naming materials in the magma/igneous rock system. *Earth-Science Reviews* **37**, 215–224.

Miller, C., Schuster, R., Klotzli, U., Frank, W. & Purtscheller, F. (1999). Post-collisional potassic and ultrapotassic magmatism in SW Tibet: geochemical and Sr–Nd–Pb–O isotopic constraints for mantle source characteristics and petrogenesis. *Journal of Petrology* **40**, 1399–1424.

Molnar, P. & Stock, J. M. (2009). Slowing of India's convergence with Eurasia since 20 Ma and its implications for Tibetan mantle dynamics. *Tectonics* **28**, TC3001, doi:10.1029/2008TC002271,2009.

Molnar, P., England, P. & Martinod, J. (1993). Mantle dynamics, uplift of the Tibetan Plateau, and the Indian monsoon. *Reviews of Geophysics* **31**, 357–396.

Müller, D. & Groves, D. I. (1993). Direct and indirect associations between potassic igneous rocks, shoshonites and gold–copper deposits. *Ore Geology Reviews* **8**, 383–406.

Owens, T. J. & Zandt, G. (1997). Implications of crustal property variations for models of Tibetan plateau evolution. *Nature* **387**, 37–43.

Pearson, N. J., Griffin, W. L. & O'Reilly, S. Y. (2008). Mass fractionation correction in laser ablation-multiple collector ICP-MS: implications for overlap corrections and precise and accurate *in situ* isotope ratio measurement. In: Sylvester, P. (ed.) *Laser-Ablation-ICP-MS in the Earth Sciences: Current Practices and Outstanding Issues. Mineralogical Association of Canada Short Course* **40**, 93–116.

Peccerillo, A. & Taylor, S. R. (1976). Geochemistry of Eocene calc-alkaline volcanic rocks from the Kastamonu area, northern Turkey. *Contributions to Mineralogy and Petrology* **58**, 63–81.

Pe-Piper, G., Piper, D. J. W., Koukouvelas, I., Dolansky, L. M. & Kokkalas, S. (2009). Postorogenic shoshonitic rocks and their origin by melting underplated basalts: The Miocene of Limnos, Greece. *Geological Society of America Bulletin* **121**, 39–54.

Petford, N. & Atherton, M. (1996). Na-rich partial melts from newly underplated basaltic crust: the Cordillera Blanca Batholith, Peru. *Journal of Petrology* **37**, 1491–1521.

Petford, N. & Gallagher, K. (2001). Partial melting of mafic (amphibolitic) lower crust by periodic influx of basaltic magma. *Earth and Planetary Science Letters* **193**, 483–499.

Petford, N., Cruden, A. R., McCaffrey, K. J. W. & Vigneresse, J. L. (2000). Granite magma formation, transport and emplacement in the Earth's crust. *Nature* **408**, 669–673.

Peucat, J. J., Vidal, P., Bernard-Griffiths, J. & Condie, K. C. (1989). Sr, Nd and Pb isotopic systematics in the Archaean low- to high-grade transition zone of southern India: syn-accretion vs post-accretion granulites. *Journal of Geology* **97**, 537–550.

Pullen, A., Kapp, P., Gehrels, G. E., Vervoort, J. D. & Ding, L. (2008). Triassic continental subduction in central Tibet and Mediterranean-style closure of the Paleo-Tethys Ocean. *Geology* **36**, 351–354.

Rapp, R. P. & Watson, E. B. (1995). Dehydration melting of metabasalt at 8–32 kbar: Implications for continental growth and crust–mantle recycling. *Journal of Petrology* **36**, 891–931.

Rapp, R. P., Watson, E. B. & Miller, C. F. (1991). Partial melting of amphibolite/eclogite and the origin of Archean trondhjemites and tonalites. *Precambrian Research* **51**, 1–25.

Rapp, R. P., Shimizu, N., Norman, M. D. & Applegate, G. S. (1999). Reaction between slab-derived melts and peridotite in the mantle wedge: experimental constraints at 3·8 GPa. *Chemical Geology* **160**, 335–356.

Richards, J. P. & Kerrich, R. (2007). Adakite-like rocks: Their diverse origins and questionable role in metallogenesis. *Economic Geology* **102**, 537–576.

Rohrlach, B. D. & Loucks, R. R. (2005). Multi-million-year cyclic ramp-up of volatiles in a lower crustal magma reservoir trapped below the Tampakan copper–gold deposit by Mio-Pliocene crustal compression in the southern Philippines. In: Porter, T. M. (ed.) *Super Porphyry Copper and Gold Deposits: A Global Perspective, Vol. 2.* Adelaide: PGC Publishing, pp. 369–407.

Rudnick, R. L. & Gao, S. (2003). Composition of the continental crust. In: Rudnick, R. L. (ed.) *The Crust, Treatise in Geochemistry, 3.* Amsterdam: Elsevier, pp. 1–64.

Rushmer, T. (1991). Partial melting of two amphibolites: contrasting experimental results under fluid-absent conditions. *Contributions to Mineralogy and Petrology* **107**, 41–59.

Rushmer, T. (1993). Experimental high-pressure granulites: some applications to natural mafic xenolith suites and Archean granulite terranes. *Geology* **21**, 411–414.

Sajona, F. G., Maury, R. C., Bellon, H., Cotten, J. & Defant, M. (1996). High field strength element enrichment of Pliocene–Pleistocene island arc basalts, Zamboanga peninsula, western Mindanao (Philippines). *Journal of Petrology* **37**, 693–726.

Scherer, E., Münker, C. & Mezger, K. (2001). Calibration of the lutetium–hafnium clock. *Science* **293**, 683–687.

Schwartz, J. J., Johnson, K., Miranda, E. A. & Wooden, J. L. (2011). The generation of high Sr/Y plutons following Late Jurassic

arc–arc collision, Blue Mountains province, NE Oregon. *Lithos* **126**, 22–41.

Searle, M. P., Yeh, M. W., Lin, T. H. & Chung, S. L. (2010). Structural constraints on the timing of left-lateral shear along the Red River shear zone in the Ailao Shan and Diancang Shan Ranges, Yunnan, SW China. *Geosphere* **6**, 316–338.

Sen, C. & Dunn, T. (1994). Dehydration melting of a basaltic composition amphibolite at 1·5 and 2·0 GPa: implications for the origin of adakites. *Contributions to Mineralogy and Petrology* **117**, 394–409.

Sisson, T. W., Ratajeski, K., Hankins, W. B. & Glazner, A. F. (2005). Voluminous granitic magmas from common basaltic sources. *Contributions to Mineralogy and Petrology* **148**, 635–661.

Steiger, R. H. & Jäger, E. (1977). Subcommission on geochronology: convention on the use of decay constants in geo- and cosmochronology. *Earth and Planetary Science Letters* **36**, 359–362.

Sun, S. S. & McDonough, W. F. (1989). Chemical and isotopic systematics of oceanic basalts: implication for mantle composition and processes. In: Saunder, A. D. & Norry, M. J. (eds) *Magmatism in the Ocean Basins. Geological Society, London, Special Publications* **42**, 313–345.

Sun, W. H., Zhou, M. F., Gao, J. F., Yang, Y. H., Zhao, X. F. & Zhao, J. H. (2009). Detrital zircon U–Pb geochronological and Lu–Hf isotopic constraints on the Precambrian magmatic and crustal evolution of the western Yangtze Block, SW China. *Precambrian Research* **172**, 99–126.

Sun, Y. S., Nafi Toksoz, M., Pei, S. P., Zhao, D. P., Morgan, F. D. & Rosca, A. (2008). S wave tomography of the crust and uppermost mantle in China. *Journal of Geophysical Research* **113**, B11307, doi:10.1029/2008JB005836.

Tang, S. H., Wang, J. H., Zhu, X. K. & Ma, H. Y. (2007). Determination of strontium isotopic composition in celestite. *Rock and Mineral Analysis* **26**, 93–96 (in Chinese with English abstract).

Tapponnier, P., Lacassin, R., Leloup, P. H., Schärer, U., Zhong, D. L., Wu, H. W., Liu, S. H., Ji, S. C., Zhang, L. S. & Zhong, J. Y. (1990). The Ailao Shan/Red River metamorphic belt: Tertiary left-lateral shear between Indochina and South China. *Nature* **343**, 431–437.

Thompson, A. B. & Connolly, A. D. (1995). Melting of the continental crust: some thermal and petrological constraints on anatexis in continental collision zones and other tectonic settings. *Journal of Geophysical Research* **100**, 15565–15579.

Todt, W., Cliff, R. A., Hanser, A. & Hofmann, A. W. (1996). Evaluation of a ^{202}Pb–^{205}Pb double spike for high-precision lead isotope analysis. In: Hart, S. R. & Basu, A. (eds) *Earth Processes: Reading the Isotopic Code. American Geophysical Union, Geophysical Monographs* **95**, 429–37.

Turner, S., Hawkesworth, C., Liu, J. Q., Rogers, N., Kelley, S. & Calsteren, P. (1993). Timing of Tibetan uplift constrained by analysis of volcanic rocks. *Nature* **364**, 50–54.

Turner, S., Arnaud, N., Liu, J., Rogers, N., Hawkesworth, C., Harris, N., Kelley, S., van Calsteren, P. & Deng, W.-M. (1996). Postcollisional, shoshonitic volcanism on the Tibetan plateau: implications for convective thinning of the lithosphere and the source of ocean island basalts. *Journal of Petrology* **37**, 45–71.

Valley, J. W. (2003). Oxygen isotopes in zircon. In: Hanchar, J. M. & Hoskin, P. W. O. (eds) *Zircon. Mineralogical Society of America and Geochemical Society, Reviews in Mineralogy and Geochemistry* **53**, 343–385.

Valley, J. W., Kinny, P. D., Schulze, D. J. & Spicuzza, M. J. (1998). Zircon megacrysts from kimberlite: oxygen isotope variability among mantle melts. *Contributions to Mineralogy and Petrology* **133**, 1–11.

Valley, J. W., Lackey, J. S., Cavosie, A. J., Clechenko, C. C., Spicuzza, M. J., Basei, M. A. S., Bindeman, I. N., Ferreira, V. P., Sial, A. N., King, E. M., Peck, W. H., Sinha, A. K. & Wei, C. S. (2005). 4·4 billion years of crustal maturation: oxygen isotope ratios of magmatic zircon. *Contributions to Mineralogy and Petrology* **150**, 561–580.

Waight, T. E., Maas, R. & Nicholls, I. A. (2000). Fingerprinting feldspar phenocrysts using crystal isotopic composition stratigraphy: Implications for crystal transfer and magma mingling in S-type granites. *Contributions to Mineralogy and Petrology* **139**, 227–239.

Wang, J., Li, J. P. & Wang, J. H. (2003). Shoshonitic magmatism in Dali–Jianchuan area, western Yunnan: a geochemical study of arc magmatism in a post-collisional strike-slip extensional setting. *Acta Petrologica Sinica* **19**, 61–70 (in Chinese with English abstract).

Wang, Q., McDermott, F., Xu, J. F., Bellon, H. & Zhu, Y. T. (2005). Cenozoic potassic rich adakitic volcanic rocks in the Hohxil area, northern Tibet: Lower-crustal melting in an intracontinental setting. *Geology* **33**, 465–468.

Wang, Q., Wyman, D. A., Xu, J. F., Zhao, Z. H., Jian, P., Xiong, X. L., Bao, Z. W., Li, C. F. & Bai, Z. H. (2006*a*). Petrogenesis of Cretaceous adakitic and shoshonitic igneous rocks in the Luzong area, Anhui Province (eastern China): Implications for geodynamics and Cu–Au mineralization. *Lithos* **89**, 424–446.

Wang, Q., Xu, J. F., Jian, P., Bao, Z. W., Zhao, Z. H., Li, C. F., Xiong, X. L. & Ma, J. L. (2006*b*). Petrogenesis of adakitic porphyries in an extensional tectonic setting, Dexing, South China: Implications for the genesis of porphyry copper mineralization. *Journal of Petrology* **47**, 119–144.

Wang, X. C., Li, X. H., Li, W. X. & Li, Z. X. (2009). Variable involvements of mantle plumes in the genesis of mid-Neoproterozoic basaltic rocks in South China: A review. *Gondwana Research* **15**, 381–395.

Wang, X. C., Li, X. H., Li, Z. X., Li, Q. L., Tang, G. Q., Gao, Y. Y., Zhang, Q. R. & Liu, Y. (2012). Episodic Precambrian crust growth: Evidence from U–Pb ages and Hf–O isotopes of zircon in the Nanhua Basin, central South China. *Precambrian Research* **222–223**, 386–403.

Wang, X. F., Metcalfe, I., Jian, P., He, L. Q. & Wang, C. S. (2000). The Jinshajiang–Ailaoshan Suture zone, China: tectonostratigraphy, age and evolution. *Journal of Asian Earth Sciences* **18**, 675–690.

Winther, K. T. (1996). An experimentally based model for the origin of tonalitic and trondhjemitic melts. *Chemical Geology* **127**, 43–59.

Winther, K. T. & Newton, R. C. (1991). Experimental melting of hydrous low-K tholeiite: evidence on the origin of Archaean cratons. *Bulletin of the Geological Society of Denmark* **39**, 213–228.

Wolf, M. B. & Wyllie, P. J. (1994). Dehydration-melting of amphibolite at 10 kbar: the effects of temperature and time. *Contributions to Mineralogy and Petrology* **115**, 369–383.

Wyman, D. A. & Kerrich, R. (1993). Archean shoshonitic lamprophyres of the Abitibi Subprovince, Canada: petrogenesis, age, and tectonic setting. *Journal of Petrology* **34**, 1067–1109.

Xia, L. Q., Li, X. M., Ma, Z. P., Xu, X. Y. & Xia, Z. C. (2011). Cenozoic volcanism and tectonic evolution of the Tibetan plateau. *Gondwana Research* **19**, 850–866.

Xiao, L. & Clemens, J. D. (2007). Origin of potassic (C-type) adakite magmas: Experimental and field constraints. *Lithos* **95**, 399–414.

Xiong, X. L., Adam, J. & Green, T. H. (2005). Rutile stability and rutile/melt HFSE partitioning during partial melting of hydrous basalt: Implications for TTG genesis. *Chemical Geology* **218**, 339–359.

Xiong, X. L., Liu, X. C., Zhu, Z. M., Li, Y., Xiao, W. S., Song, M. S., Zhang, S. & Wu, J. H. (2011). Adakitic rocks and destruction of the North China Craton: Evidence from experimental petrology and geochemistry. *Science China, Earth Sciences* **54**, 858–870.

Xu, J. F., Shinio, R., Defant, M. J., Wang, Q. & Rapp, R. P. (2002). Origin of Mesozoic adakitic intrusive rocks in the Ningzhen area of east China: Partial melting of delaminated lower continental crust? *Geology* **30**, 1111–1114.

Xu, Y. G., Chung, S. L., Jahn, B. M. & Wu, G. Y. (2001*a*). Petrologic and geochemical constraints on the petrogenesis of Permian–Triassic Emeishan flood basalts in southwestern China. *Lithos* **58**, 145–168.

Xu, Y. G., Menzies, M. A., Thirlwall, M. F. & Xie, G. H. (2001*b*). Exotic lithosphere mantle beneath the western Yangtze craton: Petrogenetic links to Tibet using highly magnesian ultrapotassic rocks. *Geology* **29**, 863–866.

Xu, Y. G., Luo, Z. Y., Huang, X. L., He, B., Xiao, L., Xie, L. W. & Shi, Y. R. (2008). Zircon U–Pb and Hf isotope constraints on crustal melting associated with the Emeishan mantle plume. *Geochimica et Cosmochimica Acta* **72**, 3084–3104.

Yang, K. H. (1998). A plate reconstruction of the eastern Tethyan orogen in southwestern China. In: Flower, M. F. J., Chung, S.-L., Lo, C.-H. & Lee, T.-Y. (eds) *Mantle Dynamics and Plate Interactions in East Asia. Geodynamics Series, American Geophysical Union* **27**, 269–287.

Yin, A. & Harrison, T. M. (2000). Geologic evolution of the Himalayan–Tibetan orogen. *Annual Review of Earth and Planetary Sciences* **28**, 211–280.

Zeng, L. S., Gao, L. E., Xie, K. J. & Zeng, J. L. (2011). Mid-Eocene high Sr/Y granites in the Northern Himalayan gneiss domes: Melting thickened lower continental crust. *Earth and Planetary Science Letters* **303**, 251–266.

Zeng, P. S., Mo, X. X. & Yu, X. Y. (2002). Nd, Sr and Pb isotopic characteristics of the alkaline-rich porphyries in western Yunnan and its compression strike-slip setting. *Acta Petrologica et Mineralogica* **23**, 231–241 (in Chinese with English abstract).

Zhang, L. S. & Schärer, U. (1999). Age and origin of magmatism along the Cenozoic Red River shear belt, China. *Contributions to Mineralogy and Petrology* **134**, 67–85.

Zhao, X., Mo, X. X., Yu, X. H., Lu, B. X. & Zhang, J. (2003). Mineralogical characteristics and petrogenesis of deep-derived xenoliths in Cenozoic syenite porphyry in Liuhe, western Yunnan province. *Earth Science Frontiers* **10**, 93–104 (in Chinese with English abstract).

Zhao, X., Yu, X. H., Mo, X. X., Zhang, J. & Lu, B. X. (2004). Petrological and geochemical characteristics of Cenozoic alkali-rich porphyries and xenoliths hosted in Western Yunnan Province. *Geoscience* **18**, 217–228 (in Chinese with English abstract).

Zhao, X. F., Zhou, M. F., Li, J. W., Sun, M., Gao, J. F., Sun, W. H. & Yang, J. H. (2010). Late Paleoproterozoic to early Mesoproterozoic Dongchuan Group in Yunnan, SW China: Implications for tectonic evolution of the Yangtze Block. *Precambrian Research* **182**, 57–69.

Zhao, Z. D., Mo, X. X., Dilek, Y., Niu, Y. L., DePaolo, D. J., Robinson, P., Zhu, D. C., Sun, C. G., Dong, G. C., Zhou, S., Luo, Z. H. & Hou, Z. Q. (2009). Geochemical and Sr–Nd–Pb–O isotopic compositions of the post-collisional ultrapotassic magmatism in SW Tibet: Petrogenesis and implications for India intra-continental subduction beneath southern Tibet. *Lithos* **113**, 190–212.

Zi, J. W., Fan, W. M., Wang, Y. J., Cawood, P. A., Peng, T. P. & Sun, L. H. (2010). Geochronological and geochemical constraints on the Dashibao Basalts, SW China: petrogenesis and relationship with the Emeishan LIP. *American Journal of Science* **310**, 1054–1080.

Zindler, A. & Hart, S. R. (1986). Chemical geodynamics. *Annual Review of Earth and Planetary Sciences* **14**, 493–571.